Tilted Weyl Semimetals

Dissertation
zur Erlangung des Grades eines Doktors der Naturwissenschaften
am Fachbereich Physik
der Freien Universität Berlin
vorgelegt von

Maximilian Trescher

Berlin, 2018

1. Gutachter: Dr. Emil J. Bergholtz
2. Gutachter: Prof. Dr. Piet W. Brouwer
Tag der Disputation: 3. Mai 2018

Selbstständigkeitserklärung

Hiermit versichere ich, dass ich in meiner Dissertation alle Hilfsmittel und Hilfen angegeben habe, und auf dieser Grundlage die Arbeit selbstständig verfasst habe. Diese Arbeit habe ich nicht schon einmal in einem früheren Promotionsverfahren eingereicht.

Maximilian Trescher, 29. März 2018

Acknowledgements

First of all I want to express my gratitude to Emil Bergholtz for supervising my thesis, for proposing and developing interesting and realistic lines of research, for his guidance and help throughout the time of my PhD, for uncountable discussions, for being approachable and available all the time and for still giving me the freedom to pursue my own ideas. I further thank him for sending me to numerous interesting conferences in beautiful places and for generally having my development and opportunities in mind. I thank Piet W. Brouwer, my second supervisor, for proposing interesting research questions and his valuable input to discussions about physics, for his kind attitude and for arranging the extension of my contract in Berlin and for welcoming me in his group when Emil Bergholtz moved to Stockholm. During all the time of my PhD, Björn Sbierski was a great and reliable collaborator. He helped me to get started in the field of Weyl semimetals and with the methods he had used in previous work. He shared his experience and knowledge with great patience and detail. I thank Johannes Knolle for approaching me and Emil Bergholtz with his ideas on type-II Weyl semimetals, his collaboration on two projects and his amicable way of communicating. I also thank Masafumi Udagawa for the collaboration on and contribution to the project on charge density waves.

I want to thank my office mates Elina and Max, who became good friends and were always open to discussion, whether about physics or not. I thank Flore Kunst for our collaboration on an exciting project about surface states, for discussing physics, python and much more and for the time spent together at conferences. Further I want to thank Jörg Behrmann for numerous discussions about physics, computers and programming and for ensuring the supply of fresh coffee. Also, I am grateful to Jens Dreger and the ZEDV for managing the cluster — without these computing powers my thesis would not have been feasible in this way. I am thankful to Marcus Stålhammar for proofreading my thesis. I also thank all other DCCQS members for the daily lunches with vivid discussions, for dice seminars, being open, friendly, helpful and approachable. I thank Gabriele Hermann, Marietta Wissmann and Anette Schumann-Welde for handling all administrative tasks in an exceptionally friendly and accommodating way. I acknowledge the funding I received from the DFG via Emil Bergholtz' Emmy Noether Grant.

I thank my parents and my family for supporting me in all my undertakings. A special thanks belongs to Melvyn Poore for turning my prose into proper English. I am deeply grateful that my son Milo was born in May 2017. Thank you, Milo, for making the last year of my PhD a very special one and for making me incredibly happy! Finally I thank my wife Saskia for her unconditional and infinite support, for lifting my spirits whenever I needed it, for her patient proofreading of my thesis, her love and a wonderful time together.

Abstract

Weyl semimetals, named after the physicist Hermann Weyl, were predicted theoretically about ten years ago and were found experimentally only in 2015. The topological properties of Weyl semimetals and their analogy to massless elementary particles make them a field of great interest in condensed matter physics. The key feature of Weyl semimetals is the crossing of two linearly dispersing bands, forming a Weyl cone.

Here we study the effects of breaking the rotational symmetry of the Weyl cone by a tilt, which refers in this context to an additive linear term proportional to the unit matrix in the Weyl equation, leaving the topological invariants unaffected. This thesis is built on a work originally published in Physical Review B, which is one of the first works to discuss the generic but previously overlooked tilt in Weyl semimetals and the very first to point out the tilt's relevance for the transport properties. Based on our theoretical results we can conclude which properties are useful to demonstrate the tilt in Weyl semimetals experimentally. We distinguish between type-I Weyl semimetals, which have moderate tilts and a point-like Fermi surface, and type-II Weyl semimetals, characterized by large tilts leading to finite electron and hole pockets.

This thesis begins with a general introduction to transport properties, Weyl semimetals and the methods we use. The following main content consists of two parts. The first part (chapters 2 and 3) addresses the electronic quantum transport properties of type-I Weyl semimetals, including the conductivity and the Fano factor. We discuss the symmetry-breaking tilt in detail and consider the influence of the tilt on the transport properties. We show that the Fano factor is a useful indicator to detect the tilt of a Weyl semimetal, as it is independent of other parameters. Further, we study the phase transition induced by disorder from a quasi-ballistic to a diffusive phase and we determine how the critical disorder strength depends on the tilt. In doing so, we show that the transition from type-I to type-II Weyl semimetals is always preceded by the disorder-induced transition. To find these results, we apply a variety of methods, including scattering matrix theory and the self-consistent Born approximation, and show exemplary lattice models.

The second part (chapters 4 and 5) considers type-II Weyl semimetals in a magnetic field including electron-electron interactions. By developing a general mean field approach for type-II Weyl semimetals, we show that the interaction induces a charge density wave (CDW). We compute the critical temperature of the transition to the CDW phase and find a cascade of successive transitions for different Landau levels. We determine the resistivity ρ using the quantum mechanic linear response theory and confirm the semi-classical picture of a $\rho \propto B^2$ scaling. The semi-classical picture is valid below the quantum limit reached at high magnetic fields. We further quantify the transition to a different scaling above the quantum limit. While the semi-classical picture only considers the non-interacting case, we are able to extend the analysis to the interacting case and show in which regime the $\rho \propto B^2$ scaling is still present. Additionally, we study the oscillations of $\rho(B)$, finding that the CDW increases their amplitude and leads to an unusual temperature dependence.

Altogether this thesis demonstrates the importance of the tilt in Weyl semimetals on the basis of quantum mechanical transport properties.

Zusammenfassung

Weyl Halbmetalle, benannt nach dem Physiker Hermann Weyl, wurden theoretisch vor etwa zehn Jahren vorhergesagt und erst 2015 experimentell nachgewiesen. Die topologischen Eigenschaften der Weyl Halbmetalle und deren Analogie zu masselosen Elementarteilchen begründen das große Interesse an diesem Forschungsgebiet der Festkörperphysik. Das Hauptmerkmal von Weyl Halbmetallen ist die Kreuzung zweier linearer Bänder, die dabei einen Weyl-Kegel bilden.

Hier untersuchen wir die Effekte der Brechung der Rotationssymmetrie des Weyl-Kegels durch die Neigung, die in diesem Zusammenhang stets den Effekt eines additiven linearen Terms in der Weyl-Gleichung, der proportional zur Einheitsmatrix ist, meint. Dies Dissertation basiert auf einem Artikel, der ursprünglich in Physical Review B erschienen ist. Dieser Artikel ist eine der ersten Arbeiten, die die allgemein gegenwärtige aber im Vorfeld übersehene Neigung in Weyl Halbmetallen diskutiert und die erste Arbeit, die die Relevanz der Neigung für die Transporteigenschaften aufzeigt. Aus unseren theoretischen Ergebnissen können wir Rückschlüsse ziehen, welche Eigenschaften sich als experimentelle Signaturen eignen würden, um die Neigung in Weyl Halbmetallen nachzuweisen. Wir unterscheiden zwischen Typ-I Weyl Halbemtallen, die eine moderate Neigung und punktartige Fermi-Flächen aufweisen, und Typ-II Weyl Halbmetallen, die durch eine Starke Neigung gekennzeichnet sind, die zu endlichen Elektron- und Loch-Taschen führt.

Diese Arbeit beginnt mit einer allgemeinen Einführung zu Transporteigenschaften, Weyl Halbmetallen und den verwendeten Methoden. Der folgende Hauptteil der Arbeit gliedert sich in zwei Abschnitte. Im ersten Abschnitt (Kapitel 2 und 3), berechnen wir die quantenmechanischen elektronischen Transporteigenschaften von Typ-I Weyl Halbmetallen, unter anderem die Leitfähigkeit und den Fano-Faktor. Dabei diskutieren wir die symmetriebrechenden Neigung detailliert und erörtern den Einfluss der Neigung auf die Transporteigenschaften. Wir zeigen, dass der Fano-Faktor ein guter Indikator ist um die Neigung eines Weyl Halbmetalls nachzuweisen, da er von anderen Parametern unabhängig ist. Weiterhin untersuchen wir den unordnungsinduzierten Phasenübergang von einer quasi-ballistischen in eine diffusive Phase und die Abhängigkeit der kritischen Unordnungsstärke von der Neigung. Dabei zeigen wir, dass dem Übergang von Typ-I zu Typ-II Weyl Halbmetallen stets der unordnungsinduzierten Phasenübergang vorausgeht. Um diese Ergebnisse zu erzielen verwenden wir verschiedene Methoden, unter anderem die Streumatrix-Theorie und die selbstkonsistente Born Annäherung und zeigen stets exemplarische Gittermodelle.

Im zweiten Abschnitt (Kapitel 4 und 5) betrachten wir Typ-II Weyl Halbmetalle im magnetischen Feld und mit Elektron-Elektron Wechselwirkungen. Mithilfe unserer Herleitung der allgemeinen Durchschnittsfeld-Näherung für Typ-II Weyl Halbmetalle zeigen wir, dass sich durch die Wechselwirkung eine Ladungsdichtewelle (CDW für “charge density wave”) ergibt. Wir berechnen die kritischen Temperaturen für den Übergang in die CDW-Phase und finden eine Kaskade von aufeinanderfolgenden Übergängen für verschiedene Landau-Level. Daraufhin berechnen wir den spezifischen Widerstand unter Verwendung der quantenmechanischen linearen Antworttheorie und bestätigen das in der semiklassischen Herleitung erwartete $\rho \propto B^2$ Verhalten. Die semiklassische Betrachtungsweise ist nur unterhalb des Quantenlimits gültig, das bei starken Magnetfeldern erreicht wird. Weiterhin quantifizieren wir den Übergang zu einem anderen Skalierungsverhalten oberhalb des Quantenlimits. Während die semiklassische Herleitung nur den Fall ohne Wechselwirkung behandelt, sind wir in der Lage unsere Berechnungen auch für den Fall mit Wechselwirkung anzuwenden und zu zeigen, in welchem Bereich das $\rho \propto B^2$ Verhalten weiterhin existiert. Zudem untersuchen wir die Oszillationen von $\rho(B)$, wobei die CDW die Amplitude vergrößert und zu einer ungewöhnlichen Temperaturabhängigkeit führt.

Insgesamt zeigt diese Arbeit die Bedeutung der Neigung in Weyl Halbmetallen anhand von quantenmechanischen Transporteigenschaften.

Contents

List of publications

This thesis is based on the following first-author publications:

- [Tre+15] M. Trescher, B. Sbierski, P. W. Brouwer and E. J. Bergholtz, *Quantum transport in Dirac materials: Signatures of tilted and anisotropic Dirac and Weyl cones*, Phys. Rev. B **91**, 115135 (2015).
  This publication is based on ideas proposed by P. W. Brouwer and E. J. Bergholtz, inspired by our earlier findings in [Ber+15]. I performed all analytical and numerical calculations and the lattice model computations. Also, I created all figures and had an important role in the writing of the manuscript. B. Sbierski provided me with his knowledge of similar calculations in isotropic Weyl semimetals.

- [Tre+17b] M. Trescher, B. Sbierski, P. W. Brouwer and E. J. Bergholtz, *Tilted disordered Weyl semimetals*, Phys. Rev. B **95**, 045139 (2017).
  The general idea was proposed by all authors, combining the main findings of the previous publication [Tre+15] and an earlier work by B. Sbierski and P. W. Brouwer [Sbi+14]. I implemented the numerical methods for the SCBA and the scattering matrix calculations myself, performed all the necessary calculations and prepared all corresponding figures. The computations involving the KPM were contributed by B. Sbierski as well as the corresponding figure. The manuscript was mainly written by me, with contributions by all other authors.

- [Tre+17a] M. Trescher, E. J. Bergholtz, M. Udagawa and J. Knolle, *Charge density wave instabilities of type-II Weyl semimetals in a strong magnetic field*, Phys. Rev. B **96**, 201101 (2017).
  J. Knolle and E. J. Bergholtz proposed the original idea. J. Knolle provided some of the analytical derivations and E. J. Bergholtz devised the lattice model. I performed all detailed calculations (including the derivation of the general mean field theory), implemented the computer programs to solve the self-consistency equations and analysed the results. M. Udagawa provided the calculations of the full lattice model, the results of which are presented in the first figure. Further I created all figures and had a pivotal role in writing the manuscript.

- [TBK18, in preparation] M. Trescher, E. J. Bergholtz and J. Knolle, *Quantum Oscillations and Magnetoresistance in Type-II Weyl Semimetals – Effect of a Field Induced Charge Density Wave Transition*,
  All authors developed jointly the main ideas. I performed all numerical calculations including the development of the necessary codes as well as the analytic derivations. I created all figures and wrote most of the manuscript.

Further I was involved in the following publications during the time of my PhD:

- [Ber+15] E. J. Bergholtz, Z. Liu, M. Trescher, R. Moessner and M. Udagawa, *Topology and Interactions in a Frustrated Slab: Tuning from Weyl Semimetals to* $\mathcal{C} > 1$ *Fractional Chern Insulators*, Phys. Rev. Lett. **1**14, 016806 (2015).
- [Com+16] F. Combes, M. Trescher, F. Piéchon and J. Fuchs, *Statistical mechanics approach to the electric polarization and dielectric constant of band insulators*, Phys. Rev. B **9**4 (2016).
- [Sbi+17] B. Sbierski, M. Trescher, E. J. Bergholtz and P. W. Brouwer, *Disordered double Weyl node: Comparison of transport and density of states calculations*, Phys. Rev. B **9**5 (2017).
- [KTB17] F. K. Kunst, M. Trescher and E. J. Bergholtz, *Anatomy of topological surface states: Exact solutions from destructive interference on frustrated lattices*, Phys. Rev. B **9**6 (2017).
  I contributed the part on pyrochlore slabs to this article and one of the figures of this part is shown in the introductory chapter 1.5 of this thesis along with a summary of the main results of [KTB17].

1. Introduction

In contemporary condensed matter physics two of the central directions of research are topological phases and topological materials. While the concept of topological phases was introduced already in the 1980s, it has become very popular during the last ten years with the discovery of topological insulators[Kön+07] and topological semimetals[Xu+15; Lu+15; Lv+15]. The pioneers of topological phases recently were awarded the Nobel prize in 2016[THK]. The concept of topological phases presents a notable extension of the hitherto general theory of phase transitions by local symmetry breaking. As topological semimetals were only recently discovered, both theoretically and experimentally, current research focuses on investigating their fundamental properties and their differences from more conventional materials.

Hermann Weyl proposed the existence of fundamental particles that are massless, have a linear dispersion and a chirality, based on his solution of the Dirac equation he found in 1929[Wey29]. For a long time it was believed that neutrinos actually were Weyl fermions, but eventually experiments showed that they have a very small mass[Bil16]. Weyl semimetals are crystalline materials whose electronic excitations, described as quasiparticles, behave like Weyl fermions. The concept of crystalline band structures mimicking the Weyl dispersion goes back to the 1930s[Her37], but realistic proposals of actual materials only emerged during the last 10 years[Mur07; BB11; Wan+11]. Only after I started my work on this thesis, investigating the then hypothetical Weyl semimetals, were several experimental discoveries reported[Xu+15; Lu+15; Lv+15], in experiments on TaAs (Tantalum arsenide) and TaP (Tantalum phosphide) crystals as well as in photonic crystal systems. Since then, the number of theoretical and experimental works on Weyl semimetals has been rapidly growing. Since Weyl semimetals are a new class of materials, there is a big interest in investigating all their physical properties, which could be useful for their experimental identification and for practictal applications. See chapter 1.5 for more details.

The key feature of Weyl semimetals is the crossing of two linearly dispersing bands, forming a Weyl cone. The visualization of this dispersion requires restriction of the momenta to two dimensions. For two momentum dimensions, the contours of constant energies are ellipsoids in general and a circle when the cone is not tilted. The actual linear dispersion in all three momentum directions leads to surfaces of constant energy in the form of ellipsoids in general, which become spheres in the symmetric case. All earlier theoretical work focused on idealized, isotropic Weyl semimetals (depicted on the left of Figure 1.1) as this description captures the topological aspect of Weyl cones, which is one of the most interesting aspects of Weyl semimetals. Nonetheless, material realizations always feature different types of anisotropies, therefore we study these anisotropies in

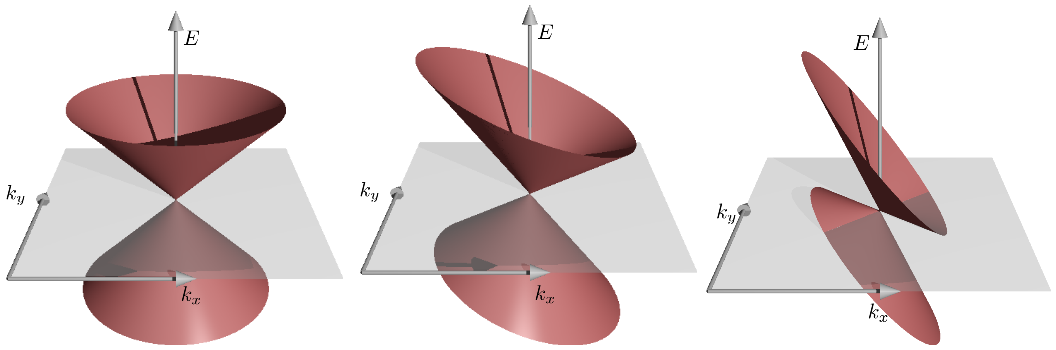

Figure 1.1.: Dispersion of a Weyl cone (only two of three momentum dimensions are shown) for different values of tilt a. From left to right, a takes the values 0, 0.4 and 1.3. The gray plane indicates zero energy.

this thesis, and distinguish between anisotropic velocities and the tilt of a Weyl cone. While the first part of this thesis studies electronic transport in Weyl semimetals with moderate tilts (middle cone in Figure 1.1), the second part focuses on Weyl semimetals so heavily tilted that one side of the cone actually lies below the zero energy plane (see rightmost cone in Figure 1.1). Such Weyl cones are called “type-II” and consequently the materials harbouring them are referred to as “type-II Weyl semimetals”[Ber+15; Sol+15; XZZ15]. The common subject throughout this thesis is the symmetry breaking tilt. The several specific consequences discussed here show the general importance of the tilt. Although the tilt does not alter the topological index of the phase, it leads to interesting quantitative and qualitative changes compared to symmetric Weyl cones. This is in contrast to much of the work on topological materials, which often focusses on the principles of symmetry.

This thesis addresses basic properties of a new, and until recently unknown, class of materials. Therefore they belong to the realm of fundamental research where material properties and physical effects are studied without a specific application in mind. The goal is to gain a general understanding of how Weyl semimetals behave and how they are different from known systems. However, it is important to note that we are not trying to give material-specific results expecting a quantitative agreement with experiments. Such predictions are made in conjunction with ab-initio methods like density functional theory (DFT) calculations. This thesis focuses on model-based condensed matter theory and aims at finding more general results and to understand the physical origin of the discovered effects. We will use a number of different theoretical techniques to study transport properties and interaction effects in these models. We always start with some analytical derivation but most often we will eventually use numerical methods to solve equations where analytical solutions are not feasible. The degree to which we rely on numerics differs from technique to technique.

Structure of this thesis

This introductory chapter recapitulates some basics of electronic transport and continues introducing several methods from quantum physics to study transport phenomena in clean and disordered systems and to incorporate electronic interactions. The methods used in quantum transport calculations include scattering matrices and the well-known Kubo formula from linear response theory. For disordered systems a specific model of disorder is introduced and the self-consistent Born approximation is derived in a diagrammatic language. To deal with interactions, the mean field approximation is presented. This part of the introduction recapitulates well established techniques that can be found in most textbooks on condensed matter physics[BF04; AS10; NB09; AM07; Dat97]. For consistency we chose to follow mostly the notation and presentation of [BF04] and will refer to the corresponding chapters in this textbook at several points. The following part of the introduction is about the concept of topology in the context of condensed matter physics. Subsequently we give a detailed description of Weyl semimetals and some of their prominent features. The last part of the introduction discusses the numerical methods used in this thesis. This introduction is followed by four chapters presenting the results of this thesis as obtained in subsequent projects. These chapters are each based on a publication of which I am the first author[Tre+15; Tre+17b; Tre+17a],[TBK18, in preparation].

The first part (chapters 2 and 3) studies the consequences of a tilt for the electronic transport properties of a tilted (but not over tilted) Weyl semimetal, namely conductance and conductance fluctuations characterized by the Fano factor. Chapter 2 considers the ballistic case. In chapter 3, the effect of disorder on these findings is discussed to see whether the robustness of the isotropic Weyl cone against disorder carries over to the tilted case.

In the second part (chapters 4 and 5) we investigate interaction effects between electrons in type-II (i.e. over tilted) Weyl semimetals in a magnetic field. We find the formation of a charge density wave due to the interactions, which are treated at a mean field level. The term “Charge density wave” refers to a (wave-like) regular modulation of electronic density in real space while in metallic systems the usual distribution of the electron charge is homogeneous. Chapter 5 compares the magnetotransport properties of type-II Weyl semimetals with and without interactions, applying the linear response formalism to the results obtained in the previous chapter. Further we discuss the resulting quantum oscillations. The concluding chapter 6 recapitulates the main findings of this thesis and puts them into context with interesting open questions and possible routes for further research.

Notation

Some common abbreviations will be used throughout the text, including BZ(Brillouin zone), CDW(charge density wave) and SCBA(self consistent Born approximation). We use the following standard notation:

$$\beta = \frac{1}{k_B T} \tag{1.1}$$

$$\boldsymbol{\sigma} = \begin{pmatrix} \sigma_1 \\ \sigma_2 \\ \sigma_3 \end{pmatrix} \tag{1.2}$$

$$\sigma_1 = \begin{pmatrix} 0 & 1 \\ 1 & 0 \end{pmatrix} \qquad \sigma_2 = \begin{pmatrix} 0 & -i \\ i & 0 \end{pmatrix} \qquad \sigma_3 = \begin{pmatrix} 1 & 0 \\ 0 & 1 \end{pmatrix} . \tag{1.3}$$

Throughout this thesis we will encounter situations where we need to discuss multiple particles, each having by a set of quantum numbers like position $\mathbf{r}$ or momentum $\mathbf{k}$, a band or spin index s, a Landau level index n etc. We will make use of the accordingly defined shorthand notation

$$\zeta_1 = (\mathbf{r}_1, s_1, n_1) \tag{1.4}$$

$$\int \mathrm{d}\zeta_1 = \sum_{s_1} \sum_{n_1} \int \mathrm{d}\mathbf{r}_1 \, . \tag{1.5}$$

1.1. Electronic transport and quantum mechanics

This part of the introduction covers the basic description of transport properties, the general setup used to study transport in theory and several quantum mechanical methods to assess transport properties. The general concept of transport applies to a vast number of physical quantities, let it be particles, charge, spin, heat, entropy etc. This thesis focuses exclusively on electronic transport, i.e. charge transport, and more specifically on regimes where quantum effects are important. As we are only interested in charge transport, we will mostly ignore the spin degree of freedom of the electrons, which anyway is not relevant for Weyl semimetals.

When talking about transport properties we have to make a clear distinction between material properties and sample properties. While experiments always study specific samples as instances of a material, physics is most often interested in material properties, being the more general quantity. Of course, material properties translate in some way or the other to sample specific properties, and vice versa: by measuring (multiple) samples we can infer material properties experimentally.

This thesis studies transport properties by theoretical means and while some of the described methods directly access the bulk material properties, other methods are suitable to calculate properties of samples of finite size. To extract general material properties from sample specific computations, we first describe the geometry of these fictitious samples used later on.

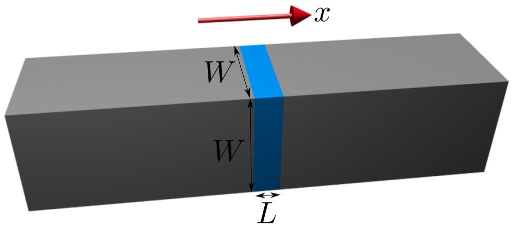

Figure 1.2.: A sample (blue) shaped as a rectangular cuboid of length L and width W with two leads (grey) attached.

1.1.1. Sample geometry

Whenever we use a sample of finite size in our transport calculations we will think of a device as depicted in Figure 1.2. The actual sample is the blue cuboid of length L in the direction of transport and width W in both transversal directions. To enable transport we need to attach leads to the sample that provide (or take away) electrons. These leads are depicted in grey and they are considered as perfectly conducting. As detailed below the material properties are derived by an appropriate scaling of this sample's properties with L and W. In the case of numerical computations we have to verify that these scaled values are then independent of the sample's specificities, i.e. its length and width, and any parameters introduced for numerical purposes, i.e. the numerical resolution. Usually this is achieved by ensuring convergence for longer (and/or wider) systems and for the different numerical parameters.

1.1.2. Classical transport quantities

When studying electronic transport, we are interested in how materials conduct electrons (or electronic charge) under different circumstances. We are mostly interested in the electric current j occurring as a response to some external "perturbation", as for example a temperature gradient, an electric or a magnetic field. We distinguish the total current I measured in units of Coulomb per second (C/s), the quantity typically measured experimentally, from the local current density $j(x)$ used in the microscopic description.

In the simplest case of electric conduction the current flows parallel to an electric field E, usually created by a voltage difference V between different leads. Then the conductance G is defined as

$$G = \frac{I}{V} = \frac{1}{R} \tag{1.6}$$

and its inverse R is called resistance. This linear relation between current and voltage is known as "Ohms law"[Ohm27]. While it holds true for many different length scales it will necessarily break down at very high electric fields when either nonlinear effects come into play or the material is structurally affected by the high voltages. From these sample specific quantities we obtain the geometry-independent conductivity σ and resistivity ρ

which are defined as

$$\sigma = \frac{1}{\rho} = \frac{L}{W^2} G \tag{1.7}$$

supposing a sample of length L and width W in both transversal directions. We further introduce the less common cube conductance g [Sbi+14] which scales as

$$g = \frac{L^2}{W^2} G \tag{1.8}$$

and is of interest when σ vanishes in the thermodynamic limit of $L, W \to \infty$.

Microscopically, conductivity is the relation between electric field $\mathbf{E}$ and current density $\mathbf{j}$

$$\mathbf{j} = \sigma \mathbf{E} \tag{1.9}$$

where we now generalize to a treatment where E and j are considered as vectors and σ is then a conductivity tensor. Often σ is diagonal and hence the current flows parallel to the applied electric field. The best known example of a non-diagonal σ is the Hall effect[Hal79], see Figure 1.3. It arises when a magnetic field is applied perpendicular to the current direction, resulting in a current perpendicular to both the original current and the magnetic field. While the classical Hall effect is proportional to the magnetic field and was discovered already in the 19th century, a quantized version of the Hall effect, the Quantum Hall effect, was found in 1980[KDP80].

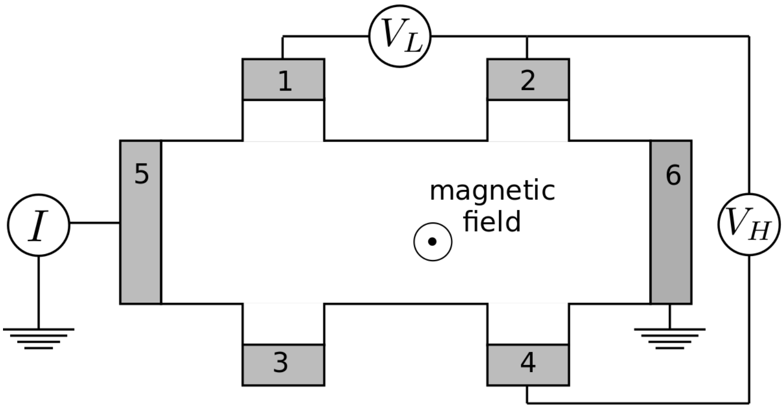

Figure 1.3.: Device to measure the Hall effect. Current is flowing from left (5) to right (6), the magnetic field is perpendicular to the plane and the Hall voltage can be measured between (2) and (4). The figure is taken from https://ocw.tudelft.nl/course-readings/the-hall-effect/ (9.3.2018), available under the Creative Commons Attribution-NonCommercial-ShareAlike 4.0 International License.

Performing a measurement of an electric current I in a quantum regime (i.e. at low temperatures and low current) does not yield a constant value all the time, but rather results in a probability distribution of current values. The shot noise, the temporal fluctuation of electric current, is due to the discrete nature of the electrons and is characterized by the Fano factor F. For a general distribution, the Fano factor F is defined as

$$F = \frac{\sigma^2}{\mu} \tag{1.10}$$

where σ^2 is the variance of the distribution (not to be confused with the conductivity) and μ is the mean value. A classical analysis would suggest that transport is a Poisson process where the mean current $\langle I \rangle$ is equal to the current fluctuations $\langle (\Delta I)^2 \rangle$ and hence the Fano factor is 1. Due tue quantum correlations the process is not poissonian and the Fano factor is always smaller than one. In usual metals where transport is diffusive it takes the value 1/3. In chapter 1.1.5 a microscopic formula for the Fano factor is given.

1.1.3. Quantum mechanics and second quantization

A general introduction to the basics of quantum mechanics can be found in many textbooks[Sak94; AS10] and will not be presented here. Instead, we introduce the notation that will be used in the subsequent chapters, following the notation used in [BF04, chapter 1]. We will work in the so called "second quantization" description, using creation ($a^\dagger$) and annihilation(a) operators. In this framework the field operator Ψ at position $\mathbf{r}$ is given in terms of the single particle wave functions ψ_ν as

$$\Psi^\dagger(\mathbf{r}) = \sum_\nu \langle \mathbf{r} \,|\, \psi_\nu \rangle^* a_\nu^\dagger \qquad \Psi(\mathbf{r}) = \sum_\nu \langle \mathbf{r} \,|\, \psi_\nu \rangle a_\nu \tag{1.11}$$

$$\Psi^\dagger(\mathbf{r}) = \frac{1}{\sqrt{\mathcal{V}}} \sum_{\mathbf{k}} e^{-i\mathbf{k}\cdot\mathbf{r}} a_{\mathbf{k}}^\dagger \qquad \Psi(\mathbf{r}) = \frac{1}{\sqrt{\mathcal{V}}} \sum_{\mathbf{k}} e^{i\mathbf{k}\cdot\mathbf{r}} a_{\mathbf{k}} \tag{1.12}$$

where ψ_ν is a complete basis. In (1.12) we write the operators in the momentum ($\mathbf{k}$) basis, where $\mathcal{V}$ is the Volume in which the fields are defined and serves as normalization constant.

In quantum mechanics, observable quantities are given by the expectation values of operators. To calculate the observable electric current we need to know the current operator. In general the current operator has two terms: the paramagnetic term $\mathbf{J}^\nabla$ and the diamagnetic part $\mathbf{J}^A$

$$\mathbf{J}_\sigma(\mathbf{r}) = \mathbf{J}_\sigma^\nabla(\mathbf{r}) + \mathbf{J}_\sigma^A(\mathbf{r}) \tag{1.13}$$

$$\mathbf{J}_\sigma^\nabla(\mathbf{r}) = \frac{\hbar}{2mi}\left[\Psi_\sigma^\dagger(\mathbf{r})\left(\nabla\Psi_\sigma(\mathbf{r})\right) - \left(\nabla\Psi_\sigma^\dagger(\mathbf{r})\right)\Psi_\sigma(\mathbf{r})\right] \tag{1.14}$$

$$\mathbf{J}_\sigma^A(\mathbf{r}) = -\frac{q}{m}\mathbf{A}(\mathbf{r})\Psi_\sigma^\dagger(\mathbf{r})\Psi_\sigma(\mathbf{r}) \tag{1.15}$$

where m is the mass of the particles, q the charge and A is the electromagnetic vector potential. In momentum space the current operator becomes

$$\mathbf{J}^{\nabla}_{\sigma}(\mathbf{r}) = \frac{\hbar}{2m\mathcal{V}} \sum_{\mathbf{kq}} \left((\mathbf{k} + \frac{1}{2}\mathbf{q}) e^{i\mathbf{q}\cdot\mathbf{r}} a^{\dagger}_{\mathbf{k}\sigma} a_{\mathbf{k}+\mathbf{q},\sigma} \right) \tag{1.16}$$

$$\mathbf{J}^{A}_{\sigma}(\mathbf{r}) = \frac{-q}{m\mathcal{V}} \mathbf{A}(\mathbf{r}) \sum_{\mathbf{kq}} \left(e^{i\mathbf{q}\cdot\mathbf{r}} a^{\dagger}_{\mathbf{k}\sigma} a_{\mathbf{k}+\mathbf{q},\sigma} \right) . \tag{1.17}$$

1.1.4. Linear response theory and the Kubo formula

The general idea of linear response theory is the assumption that any response to a weak external perturbation of a system previously in thermal equilibrium can be described by a linear function of this external perturbation. Therefore we want to find the proportionality factor between an external perturbation and a measurable response. The formula to obtain this linear response in a quantum system is known as Kubo formula[Kub57]. While linear response theory is used in many contexts, here we are mostly interested in electric properties like conductivity. The presentation and derivation of the Kubo formula in this chapter follows [BF04, chapter 6] (see also [AM07, chapter A7.1]).

The expectation value of some operator A in a quantum system described by H_0 in equilibrium can be calculated as

$$\langle A \rangle = \frac{1}{Z_0} \operatorname{Tr}\left[\rho_0 A\right] , \qquad \rho_0 = e^{-\beta H_0} = \sum_n \left(|n\rangle \langle n| \, e^{-\beta E_n} \right) , \qquad Z_0 = \operatorname{Tr}[\rho_0] \tag{1.18}$$

where ρ_0 is the density operator, Z_0 the partition function and $|n\rangle$ a set of eigenstates. We add an external perturbation $H'(t)$ to the Hamiltonian of the unperturbed system H_0. The external perturbation starts at some point in time t_0 and we are interested in the evolution of $\langle A(t) \rangle$ under the new Hamiltonian $H(t) = H_0 + H'(t)\theta(t - t_0)$. In principle, the exact time evolution of such an expectation values of a quantum mechanical operator can be calculated. In practice, however, this time evolution is often impossible to solve analytically and therefore we use the linear response approximation. We will denote the average with respect to H_0 with $\langle\rangle_0$ and we introduce the retarded[1] correlation function $C^R_{AH'}$ as

$$\langle A(t) \rangle - \langle A \rangle_0 = \int_{t_0}^{t} \mathrm{d}t' C^R_{AH'}(t, t') . \tag{1.19}$$

In the interaction picture the time dependence of $|n(t)\rangle$ is given by

$$|n(t)\rangle = e^{-iH_0 t} \hat{U}(t, t_0) \, |\hat{n}(t_0)\rangle \tag{1.20}$$

---

[1] The superscript R denotes the “retarded” correlation function which intuitively corresponds to the causal action “forward” in time, as opposed to the “advanced” correlation function that works backwards in time.

where $|\hat{n}(t_0)\rangle$ is defined as $|\hat{n}(t_0)\rangle = e^{iH_0 t_0}|n(t_0)\rangle = |n\rangle$. Further, the unitary matrix $\hat{U}(t,t_0)$ is, to linear order, given by

$$\hat{U}(t,t_0) = 1 + \frac{1}{i}\int_{t_0}^{t} \mathrm{d}t' \hat{H}'(t)\,. \tag{1.21}$$

Inserting this into (1.18) we obtain the expectation value of A up to linear order in the perturbation. The Kubo formula then takes the form

$$C^R_{AH'} = -i\theta(t-t')\left\langle \left[A(t), H'(t')\right]\right\rangle_0\,. \tag{1.22}$$

Combining (1.19) and (1.22) we can compute $\langle A(t)\rangle$ to linear order in H' where we only need to evaluate expectation values with respect to H_0.

This formula can be used to compute the bulk conductivity of a system. To this end we introduce the current-current correlation function

$$\Pi^R_{\alpha\beta}(\mathbf{r},\mathbf{r}',t-t') = C^R_{J_0^\alpha(\mathbf{r})J_0^\beta(\mathbf{r}')}(t-t') \tag{1.23}$$

of the current operator J where α and β denote spatial directions x,y,z. The relation between the current operator and the conductivity tensor in linear response in frequency space[2] is given by

$$J_e^\alpha(\mathbf{r},\omega) = \int \mathrm{d}\mathbf{r}' \sum_\beta \sigma^{\alpha\beta}(\mathbf{r},\mathbf{r}',\omega)E^\beta(\mathbf{r}',\omega)\,. \tag{1.24}$$

Computing the expectation value of the current operator in response to an external electric field using the Kubo formula (1.22) we find, after some intermediate algebra[BF04, chapter 6], that the conductivity tensor reads

$$\sigma_{\alpha\beta}(\mathbf{r},\mathbf{r}',\omega) = \frac{ie^2}{\omega}\Pi^R_{\alpha\beta}(\mathbf{r},\mathbf{r}',\omega) + \frac{e^2 n(\mathbf{r})}{i\omega m}\delta(\mathbf{r}-\mathbf{r}')\delta_{\alpha\beta} \tag{1.25}$$

for some frequency ω, the electron charge e, its mass m and n the electron density. Assuming that $\sigma_{\alpha\beta}$ is translationally invariant, this formula can be recast in the form

$$\sigma_{\alpha\beta}(\omega) = i\hbar\sum_{\zeta,\zeta'}\frac{f(E_{\zeta'})-f(E_\zeta)}{E_\zeta - E_{\zeta'}}\frac{\left\langle \zeta \middle| \hat{j}_\alpha \middle| \zeta'\right\rangle\left\langle \zeta' \middle| \hat{j}_\beta \middle| \zeta\right\rangle}{\hbar\omega + E_{\zeta'} - E_\zeta + i\hbar/(2\tau)} \tag{1.26}$$

for non interacting fermions[TC15; SY16], where f is the Fermi function, E the dispersion relation, τ the lifetime of the (quasi-)particles and ζ is a shorthand notation for any quantum number pertinent to the system under consideration.

---

[2] As an equilibrium property σ can only depend on time differences $t-t'$ and hence it depends only on a single frequency after a Fourier transformation.

1.1.5. Scattering matrix for mesoscopic systems

In contrast to the linear response theory introduced before, which describes bulk properties, the scattering matrix (S-matrix) formalism always describes a finite system. The formalism described in this chapter is also known as Landauer-Büttiker formalism[Lan57; Lan70; Büt88]. Here we follow the presentation and derivations of [BF04, chapter 7], and [Dat97].

This formalism is usually used for mesoscopic samples, hence the sample conventionally is denoted M. This sample M is connected to two leads on the left and right L and R (generalization to more leads is straightforward). For simplicity, we choose the leads to be along the $x-$direction. These leads are considered perfect conductors with N channels, where N is obtained from the transverse quantization condition of the wave functions. Using leads of the same width as the sample allows the use of the same transverse quantization everywhere. A further assumption is the coherent movement of the electrons through the sample, restricting the sample's size to be smaller than the mean free path of an electron. The cleaner the sample, the longer the mean free path is and thereby the allowed system size increases.

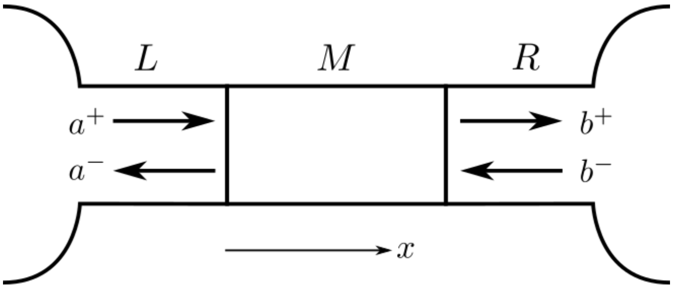

Figure 1.4.: Two-terminal mesoscopic sample.

The leads connect the sample to reservoirs, which are considered to be much larger than the sample, so we can assume that any particle entering the lead will disappear into the reservoir and that particles arriving from a reservoir are in equilibrium with this reservoir. We introduce eigenstates in the leads as $\phi^{\pm}_{\alpha n E}(x, \mathbf{r}_\perp)$ where α labels the lead L or R and n is an integer labeling the states with energy E. These eigenstates are normalized in an unusual fashion by fixing the absolute probability current in a given cross section $\mathcal{S}$, such that for particles of mass m

$$\int_{\mathcal{S}} \mathrm{d}\mathbf{r}_\perp \left(\phi^{\pm}_{\alpha n E}(x, \mathbf{r})\right)^* \frac{\mathbf{p}_x}{m} \left(\phi^{\pm}_{\alpha n E}(x, \mathbf{r})\right) = \pm \frac{1}{m} \,. \tag{1.27}$$

Since we consider a mesoscopic sample where the particles move coherently, we must define a single wave function spanning over both leads and the sample

$$\psi_E(x,\mathbf{r}_\perp) = \begin{cases} \sum_n a^+\phi^+_{LnE}(x,\mathbf{r}_\perp) + \sum_n a^-\phi^-_{LnE}(x,\mathbf{r}_\perp) & x \in L \\ \phi_{M,E}(x,\mathbf{r}_\perp) & x \in M \\ \sum_n b^+\phi^+_{RnE}(x,\mathbf{r}_\perp) + \sum_n b^-\phi^-_{RnE}(x,\mathbf{r}_\perp) & x \in R \end{cases} \tag{1.28}$$

The unknown coefficients $a_n^\pm, b_n^\pm$ can be found by solving a set of linear equations obtained from the continuity condition on the wave function and its derivative. Writing the set of n parameters $a_n^\pm$ as vector $\mathbf{a}^\pm$ and collecting the amplitudes of ingoing and outgoing waves $\mathbf{c}_{in}$ and $\mathbf{c}_{out}$ (c.f. Figure 1.4) as

$$\mathbf{c}_{in} = \begin{pmatrix} \mathbf{a}^+ \\ \mathbf{b}^- \end{pmatrix} \mathbf{c}_{out} = \begin{pmatrix} \mathbf{a}^- \\ \mathbf{b}^+ \end{pmatrix} \tag{1.29}$$

$$\tag{1.30}$$

we can introduce the scattering matrix $\mathbf{S}$

$$\mathbf{c}_{out} = \mathbf{S}\mathbf{c}_{in} \tag{1.31}$$

$$\mathbf{S} = \begin{pmatrix} \mathbf{r}(E) & \mathbf{t}'(E) \\ \mathbf{t}(E) & \mathbf{r}'(E) \end{pmatrix} , \tag{1.32}$$

a $2N \times 2N$ matrix consisting of four $N \times N$ blocks. The blocks $\mathbf{r}$ and $\mathbf{r}'$ are reflection matrices and the blocks $\mathbf{t}$ and $\mathbf{t}'$ are transmission matrices. Using the knowledge of all these matrix elements $t_{nn'}, r_{nn'}$ we can define the scattering states. These are states where the incoming wave occupies a single channel in the lead and has amplitude 1. Labeling the scattering states with the lead channel n, the lead $\alpha \in L, R$ where the incoming wave is located and, as before, the energy E, we can write them as

$$\psi_{LnE}(x,\mathbf{r}_\perp) = \begin{cases} \phi^+_{LnE}(x,\mathbf{r}_\perp) + \sum_{n'} r_{n'n}\phi^-_{Ln'E}(x,\mathbf{r}_\perp) & x \in L \\ \phi_{M,E}(x,\mathbf{r}_\perp) & x \in M \\ \sum_{n'} t_{n'n}\phi^+_{Rn'E}(x,\mathbf{r}_\perp) & x \in R \end{cases} \tag{1.33}$$

$$\psi_{RnE}(x,\mathbf{r}_\perp) = \begin{cases} \sum_{n'} t'_{n'n}\phi^-_{Ln'E}(x,\mathbf{r}_\perp) & x \in L \\ \phi_{M,E}(x,\mathbf{r}_\perp) & x \in M \\ \phi^-_{RnE}(x,\mathbf{r}_\perp) + \sum_{n'} r'_{n'n}\phi^+_{Rn'E}(x,\mathbf{r}_\perp) & x \in R \end{cases} \tag{1.34}$$

The scattering matrix has some useful properties[BF04; Dat97]: it is unitary and time-reversal symmetric at zero magnetic field, while at finite magnetic field $\mathbf{S}^*_{-\mathbf{B}} = \mathbf{S}^\dagger_{\mathbf{B}}$.

Combination of S-matrices

It is important to note that while the "Scattering Matrix" S is a unitary matrix, the combination of two scattering matrices describing two successive systems is not given by the usual matrix multiplication, as one might expect at first sight. For a system consisting of two consecutive scattering regions M_1 and M_2 with given scattering matrices S_1 and S_2

$$\mathbf{S}_1 = \begin{pmatrix} \mathbf{r}_1(E) & \mathbf{t}'_1(E) \\ \mathbf{t}_1(E) & \mathbf{r}'_1(E) \end{pmatrix} \qquad \mathbf{S}_2 = \begin{pmatrix} \mathbf{r}_2(E) & \mathbf{t}'_2(E) \\ \mathbf{t}_2(E) & \mathbf{r}'_2(E) \end{pmatrix} , \tag{1.35}$$

the scattering matrix S for the full system has the elements[Dat97, p. 126]

$$\mathbf{r} = \mathbf{r}_1 + \mathbf{t}'_1 \mathbf{r}_2 \left[1 - \mathbf{r}'_1 \mathbf{r}_2\right]^{-1} \mathbf{t}_1 \qquad \mathbf{t}' = \mathbf{t}'_1 \left[1 - \mathbf{r}_2 \mathbf{r}'_1\right]^{-1} \mathbf{t}'_2 \tag{1.36}$$

$$\mathbf{t} = \mathbf{t}_2 \left[1 - \mathbf{r}'_1 \mathbf{r}_2\right]^{-1} \mathbf{t}_1 \qquad \mathbf{r}' = \mathbf{r}'_2 + \mathbf{t}_2 \left[1 - \mathbf{r}'_1 \mathbf{r}_2\right]^{-1} \mathbf{r}'_1 \mathbf{t}'_2 \, . \tag{1.37}$$

Conductance and Fano factor from S-matrix

We can compute the conductance of the sample under consideration by applying the Landauer formula[Lan57; Lan70]. Making use of the transmission coefficients, it provides the conductance G in dependence of the chemical potential μ

$$\begin{aligned} G(\mu) &= \frac{2e^2}{h} \sum_n \mathcal{T}_n(\mu) = \frac{2e^2}{h} \sum_n T_n(\mu) \\ &= \frac{2e^2}{h} \operatorname{Tr} \left[\mathbf{t}(\mu)^\dagger \mathbf{t}(\mu) \right] , \end{aligned} \tag{1.38}$$

introducing the eigenvalues $\mathcal{T}_n$ of the matrix $\mathbf{t}^\dagger \mathbf{t}$, the probabilities $T_n = (\mathbf{t}^\dagger \mathbf{t})_{nn}$ and including a factor 2 for spin degeneracy. One can understand this formula intuitively as the total current being given as a sum of transmission probabilities for all possible ways an incoming electron at the energy of the chemical potential can be transmitted to the other lead. Derivations of (1.38) along the lines of this intuitive argument can be found in the literature[BF04; Dat97]. We will derive it in the next section using the linear response theory introduced in 1.1.4, again following the presentation in [BF04].

The Fano factor as introduced in chapter 1.1.2 is given by the fluctuations and mean value of the current. Expressing the current operator in terms of the scattering matrix, we can compute the Fano factor from the scattering matrix. The calculation leading to the expression

$$F = \frac{\sum_n T_n (1 - T_n)}{\sum_n T_n} \tag{1.39}$$

was first performed by Lesovik[Les89]. This formula is valid for a two-terminal system and a generalization to multi-terminal systems can be found in [Büt90].

Derivation of the Landauer Formula using the linear response theory

Here we derive the Landauer formula (1.38) by using the linear response theory introduced in 1.1.4, following the derivation in [BF04, chapter 7.2.2]. We write the conductance G in terms of the current-current correlation function

$$G(\omega) = -\frac{2e^2}{\omega}\Im \int_{-\infty}^{\infty} \mathrm{d}t e^{i(\omega+i\eta)t}(-i)\theta(t)\langle[I(x,t), I(x,0)]\rangle_0 \,, \tag{1.40}$$

where G is independent of x as a result of current conservation and $\Im$ denotes taking the imaginary part. Writing the current operator (1.15) in the basis of scattering states (1.34) and using λ as shorthand notation for $n\eta E$ (with $\eta = \pm 1$), we find

$$I(x) = \sum_{\lambda\lambda'} j_{\lambda\lambda'}(x) c_\lambda^\dagger c_{\lambda'} \tag{1.41}$$

$$j_{\lambda\lambda'}(x) = \frac{1}{2mi}\int_{\mathcal{S}} \mathrm{d}\mathbf{r}_\perp \phi_\lambda^*(x,\mathbf{r}_\perp)\left(\overrightarrow{\partial_x} - \overleftarrow{\partial_x}\right)\phi_{\lambda'}(x,\mathbf{r}_\perp)\,. \tag{1.42}$$

Plugging these expressions into (1.40) and using the relations $\langle c_\lambda^\dagger c_\lambda\rangle = \delta_{\lambda\lambda'} n(E_\lambda)$ we get[3]

$$G(\omega) = \frac{2e^2}{\omega}\Im \sum_{\lambda\lambda'}\left(\frac{|j_{\lambda\lambda'}(x')|^2}{\hbar\omega + i\eta + E_\lambda - E_{\lambda'}}\left(n(E_\lambda) - n(E_{\lambda'})\right)\right) \tag{1.43}$$

which in the limit of $\omega \to 0$ becomes

$$G(0) = 2e^2\hbar\pi \sum_{\lambda\lambda'}\left(|j_{\lambda\lambda'}(x')|^2\left(-\frac{\partial n(E_\lambda)}{\partial E_\lambda}\right)\delta(E_\lambda - E_{\lambda'})\right)\,. \tag{1.44}$$

At zero temperature the derivative of the Fermi function becomes a delta function $\delta(E-\mu)$ and replacing $\sum_\lambda$ with the appropriate $\sum_{n\eta}\frac{m}{2\pi\hbar^2}\int \mathrm{d}E$ we get

$$G(0) = 2e^2\hbar\pi\left(\frac{m}{2\pi\hbar^2}\right)^2 \sum_{nn',\eta\eta'} |j_{n\eta\mu,n'\eta' mu}(x')|^2\,. \tag{1.45}$$

For a given energy μ we can easily evaluate the matrix elements of j as we know the wave functions in the leads and we can evaluate j at an arbitrary value x'

$$j_{n\eta\mu,n'\eta' mu}(x') = \frac{\hbar}{m}\mathbf{j} = \frac{\hbar}{m}\begin{pmatrix} (\mathbf{t}^\dagger\mathbf{t})_{nn'} & (\mathbf{t}^\dagger\mathbf{r}')_{nn'} \\ -(\mathbf{t}'^\dagger\mathbf{r})_{nn'} & -(\mathbf{t}'^\dagger\mathbf{t}')_{nn'}\end{pmatrix}\,. \tag{1.46}$$

Then the sum becomes

$$\sum_{nn',\eta\eta'} |j_{n\eta\mu,n'\eta' mu}(x')|^2 = \frac{\hbar^2}{m^2}\,\mathrm{Tr}\left[\mathbf{j}^\dagger\mathbf{j}\right] \tag{1.47}$$

$$= \frac{2\hbar^2}{m^2}\,\mathrm{Tr}\left[\mathbf{t}^\dagger\mathbf{t}\right]\,, \tag{1.48}$$

where we make use of the unitarity of the $\mathbf{S}$ matrix. Substituting this result into (1.45) we now find the Landauer formula as stated in (1.38).

---

[3] The commutator of $[I(t), I(0)]$ contributes $e^{i(E_\lambda - E_{\lambda'})t/\hbar}$ to the dt integration.

1.1.6. Ballistic vs. diffusive transport

Electrons moving through a crystal can scatter at impurities in the material, lattice dislocations, phonons (lattice vibrations) etc. The mean free path ξ gives the average distance between two of such scattering events. For metals at room temperature, ξ becomes very short. Therefore, in any sample of length L (as in Figure 1.2) longer than ξ, especially any metal wire we encounter in our daily life, electrons scatter multiple times until they have travelled through the sample. The transport is then said to be "diffusive". To be precise, we should distinguish the mean free path between elastic scattering events ξ and the average distance between inelastic scattering events $\xi_{\text{inelastic}}$. When studying disordered systems with the scattering matrix approach, as derived in chapter 1.37 and detailed in chapter 1.6.2, we assume $\xi_{\text{inelastic}} > \xi$ and we consider samples of intermediate size L, where $\xi_{\text{inelastic}} > L > \xi$.

The transport is called "ballistic" when the electrons travel through the sample of length L without scattering, i.e. in situations where L is smaller than ξ. The experimental realization of ballistic transport is only possible at low temperatures and in very clean samples. To decide whether transport is ballistic or diffusive for a given sample one could measure the conductance fluctuations characterized by the Fano factor (1.10). Diffusive transport in a small sample, which is much longer than the mean free path but much shorter than an inelastic scattering length, leads to a Fano factor of $\frac{1}{3}$[BB92]. A prime example for ballistic transport is graphene. Incidentally the ballistic transport in this two-dimensional system also leads to a Fano factor of $\frac{1}{3}$ [Two+06; DiC+08]. In Weyl semimetals however, seen as the three-dimensional generalizations of graphene (see chapter 1.5) ballistic transport leads to a larger Fano factor. This characteristic transport property was known only for isotropic Weyl semimetals[Sbi+14]. The aim of this thesis, notably the works presented in chapters 2 and 3, is to find the Fano factor for a general Weyl semimetal and to answer the question whether this number changes if disorder is present.

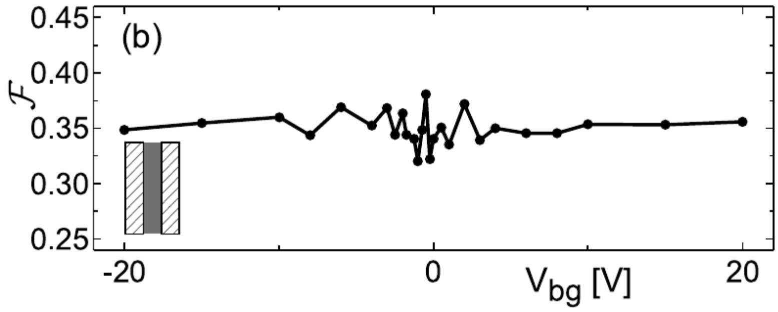

Figure 1.5.: Measurement of Fano factor F in graphene for different values of the back-gate Voltage V_{bg}. (Taken from [DiC+08])

Often graphene is said to have a very high conductivity, but as conductivity for two-dimensional systems is defined differently from three-dimensional ones, the comparison of the numbers obtained for graphene to conductivities of conventional three-dimensional metals is rather useless. On the other hand it is sensible to compare the Fano factor which is defined independently of dimensionality.

1.2. Disordered systems

1.2.1. Disorder Hamiltonian

In most real materials we encounter some type of disorder. A common source of disorder are impurities, i.e. some atoms are of a different element than the surrounding crystal. These can either locally change the potential energy of electrons in the crystal — what we call “potential disorder” — or have magnetic properties leading to a rich phenomenology[Kon64; AS10]. Here we concentrate on potential disorder, described by an additional fixed potential to the otherwise free electrons described by an effective low energy theory or a lattice model. Denoting any additional quantum numbers except position with ζ as discussed in 1, the Hamiltonian of such a disordered system reads

$$H = H_0 + H_{\text{dis}} \tag{1.49}$$

with the free particles dispersion

$$H_0 = \int \mathrm{d}\mathbf{r} \int \mathrm{d}\zeta \psi^\dagger(\mathbf{r},\zeta) H_0(\mathbf{r},\zeta) \psi(\mathbf{r},\zeta)\,. \tag{1.50}$$

For a translationally invariant crystal this Hamiltonian is diagonal in **k**-space and denoted with

$$H_0(\mathbf{k},\zeta) = \varepsilon_{\mathbf{k},\zeta}\,. \tag{1.51}$$

We model the disorder as a set of randomly placed scatterers locally changing the potential energy, here with Gaussian potentials

$$H_{\text{dis}} = \sum_j U(\mathbf{r} - \mathbf{r}_j) \tag{1.52}$$

$$U(\mathbf{r}) = \frac{\pm u_0}{(\sqrt{\pi} d_0)^2} \exp\left(-\frac{r^2}{d_0^2}\right)\,, \tag{1.53}$$

which in momentum space is equivalent to

$$u(\mathbf{q}) = \pm u_0 \exp\left(-\frac{q^2}{q_0^2}\right) \tag{1.54}$$

with $q_0 = 2/d_0$. This type of static disorder cannot absorb any energy from the scattered energy and hence leads to elastic scattering. Another common model of the disorder potential is called “white noise”, where the correlations are only local ($\langle U(\mathbf{r})U(\mathbf{r}')\rangle \propto \delta(\mathbf{r},\mathbf{r}')$). This model can be numerically favorable but it is missing the physically relevant lengthscale d_0 of the Gaussian disorder potential. Then the momentum cutoff becomes important and defines the missing lengthscale, while in the Gaussian case the momentum cutoff can be taken to infinity[4]. Therefore we will only use the Gaussian disorder potential.

1.2.2. Disorder self-average

When we consider small disordered samples, such that electrons could move and scatter coherently through the whole sample, the resulting behaviour depends on the complex diffraction patterns determined by the exact location of each impurity. If however the system is much bigger than the coherence length we will encounter disorder self-average: The system then can be seen as a collection of small (coherent) subsystems which are phase-independent. On its way through the system a single electron moves through a number of these independent subsystems and the overall behaviour will be given by an incoherent average of the subsystems. Therefore the effective behaviour of these electrons can be equally well described by averaging over impurity positions[5]. This averaging procedure has the additional benefit of restoring translational invariance and hence we can continue to perform calculations in momentum space.

1.2.3. Green’s function and Feynman diagrams

For the study of such disordered systems we will make use of the self-consistent Born approximation (SCBA), also known as non-crossing approximation[AS10, p. 227] due to the corresponding diagrammatic expansion. A more general introduction to the SCBA, diagrammatic expansions and Green’s function can be found in [BF04, chapter 11.5], [AS10, chapter 5.3] and [AM07, chapter 3]. Here, we follow the presentation of [BF04, chapter 12] and [OK14; NKA10]. For consistency we introduce here

$$\xi_\nu = \varepsilon_\nu - \mu \tag{1.55}$$

the energy levels including the chemical potential, but as described below we almost exclusively discuss the case of $\mu = 0$. Using the collection of quantum numbers ζ (as defined in chapter 1)— here including an imaginary time τ with corresponding integration $\int_0^\beta \mathrm{d}\tau$ — we can write the formal solution to the full Green’s function of (1.49) in a basis $|\nu\rangle$ diagonalizing H_0 as solutions of the following matrix equations using the

---

[4] The cutoff is formally infinite, in the numerical calculations it can be chosen big enough to have no influence on the results.

[5] To be exact we should impose a fixed number of impurities and average over the distribution of impurity positions sets $\{r_j\}$, called disorder realizations.

transformed potential $V_{\nu\nu'} = \int \mathrm{d}\mathbf{r} \, \langle \nu | \mathbf{r} \rangle \, V(\mathbf{r}) \, \langle \mathbf{r} | \nu' \rangle$ and the Matsubara frequency[6] ik_n

$$\sum_{\nu''} [(ik_n - \xi_\nu)\delta_{\nu\nu''} - V_{\nu\nu''}] G_{\nu''\nu'}(ik_n) = \delta_{\nu\nu'} \, . \tag{1.56}$$

The Green's function of the clean system (as described by H_0 alone) is diagonal

$$\sum_{\nu''} (ik_n - \xi_\nu)\delta_{\nu\nu''} G^0_{\nu''\nu'}(ik_n) = \delta_{\nu\nu'} \tag{1.57}$$

$$\Rightarrow \quad G^0_{\nu\nu'}(ik_n) = \frac{1}{ik_n - \xi_\nu} \delta_{\nu\nu'} \, . \tag{1.58}$$

From these equations the Dyson equation for the full Green's function can be derived

$$G_{\nu\nu'} = \delta_{\nu\nu'} G^0_{\nu\nu'}(ik_n) + \sum_{\nu''} G^0_{\nu\nu}(ik_n) V_{\nu\nu''} G_{\nu''\nu'}(ik_n) \tag{1.59}$$

Substituting this Dyson equation iteratively into itself yields an infinite perturbative series in powers of V. We will use Feynman diagrams to represent terms in this series and to perform "visual" computations.

In the following diagrams scattering is indicated by dashed lines, scatterers are shown as stars, the bare Green's function is a solid (thin) line and the full, disorder averaged Green's function $\langle \mathbf{G} \rangle_{\mathrm{imp}}$ is depicted as bold solid line. As discussed above we recover momentum conservation once we perform the disorder average hence the momentum change due to a single scatterer must sum to zero. As an exemplary diagram we show in Figure 1.6 the simplest process giving an interesting contribution, where the momentum of the propagator temporarily changes and $u_{\mathbf{q}}$ is the scattering amplitude corresponding to the momentum change q. At every vertex the sum of momenta must be conserved as in the exemplary wigwam diagram shown in Figure 1.6. In following diagrams we

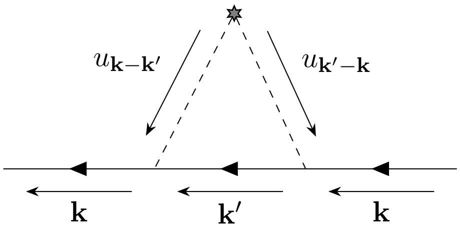

Figure 1.6.: A simple Feynman diagram, called "wigwam" diagram.

---

[6] The Matsubara frequencies are a set of imaginary frequencies, used to calculate Green's functions at finite temperature. The use of the Matsubara frequencies involves some computational "tricks" to obtain physical result, like the extension of the Green's functions to imaginary time and analytic continuations back to the real axis. Here they are used to provide the formally correct equation of the Green's functions, while the derived results will be formulated in real time using the real energies as parameters.

will not show the momentum dependency for better readability, but the first (incoming) and last (outgoing) line always must be of the same momentum $\mathbf{k}$ in the averaged case. Expanding the series on powers of u amounts to grouping all possible diagrams by their number of scattering lines. This leads to the diagrammatic representation of the perturbative series for $\langle \mathbf{G} \rangle_{\mathrm{imp}}$ shown in Figure 1.7.

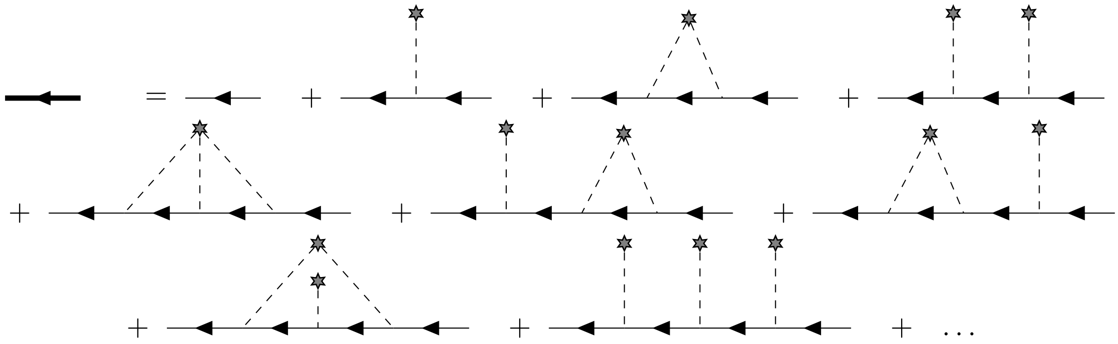

Figure 1.7.: Diagrammatic expansion of the impurity averaged Green's function. Diagrams up to third order are shown.

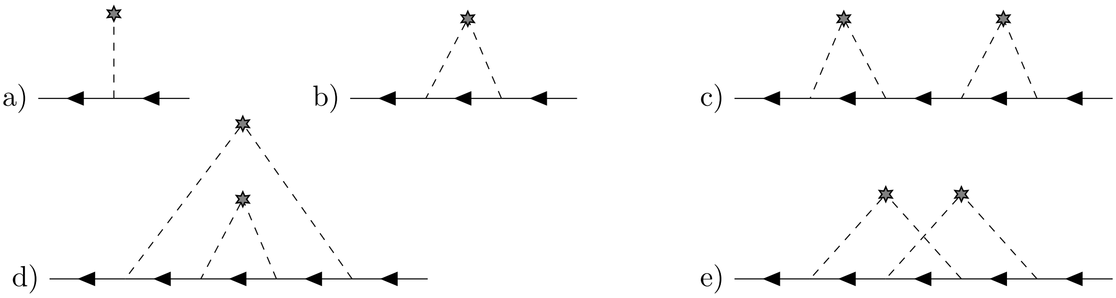

Figure 1.8.: Exemplary diagrams: a) single impurity line, b) the wigwam diagram, c) two consecutive wigwams, d) two nested wigwams, e) two crossed wigwams

Knowing the different possible diagrams, as appearing in Figure 1.7 and Figure 1.8, we can introduce the concept of 1-particle-irreducible (1-PI) diagrams. We call the dashed lines "impurity lines" and the solid lines corresponding to the electron propagators "fermion lines". Neglecting the two external fermion lines, a diagram is called 1-PI if it cannot be cut into two distinct pieces by cutting a single fermion line. For example, the diagrams b), d) and e) in Figure 1.8 are 1-PI, while diagram c) is not 1-PI, as it can be cut into two independent wigwam diagrams by cutting a single fermion line.

The sum of all 1-PI diagrams is the self-energy, depicted as hatched circle in the diagrams. The expansion of the impurity averaged Green's function is then simplified to a sum of self-energies connected by bare propagators, leading to the Dyson equation shown in Figure 1.9. To solve this equation we have to choose some approximation for the self-energy.

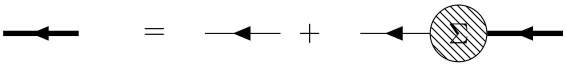

Figure 1.9.: Dyson Equation for the impurity averaged Green's function (bold line) in terms of the bare Green's function (thin line) and the self-energy Σ.

Lowest order approximation

To the lowest order, we can approximate the self-energy Σ as being equal to diagram a) in Figure 1.8, the single impurity line. In this approximation the self-energy simply shifts all energy levels by the average disorder potential, i.e. it amounts to a global change of the chemical potential. Therefore the consequences are not very interesting from a theoretical point of view, as the chemical potential is just a simple parameter in our theoretical models and is irrelevant when considering fixed stochiometry. Consequently, we study disorder potentials with zero average to avoid an additional contribution to the chemical potential.

First order Born approximation and full Born approximation

In the first order Born approximation the self-energy is given by diagram b) of Figure 1.8, while the full Born approximation includes also wigwam type diagrams with more than two impurity lines, i.e. multiple scattering events of the same impurity.

Self-consistent Born approximation

The self-consistent Born approximation (SCBA) is obtained by replacing the bare propagator in the single wigwam diagram of the first order Born approximation with the full propagator, effectively leading to a set of self-consistent equations, here given as function of energy and not of imaginary time[7].

$$\langle \hat{\mathbf{G}}(\mathbf{k},\varepsilon)\rangle_{\text{imp}} = \langle \frac{1}{\varepsilon - H}\rangle = \frac{1}{\varepsilon - \varepsilon_{\mathbf{k}} - \hat{\Sigma}(\mathbf{k},\varepsilon)} \tag{1.60}$$

$$\hat{\Sigma}\,(\mathbf{k},\varepsilon) = \int \frac{\mathrm{d}\mathbf{k}'}{(2\pi)^3} n_i |u_i(\mathbf{k}-\mathbf{k}')|^2 \langle \hat{\mathbf{G}}(\mathbf{k}',\varepsilon)\rangle_{\text{imp}} \tag{1.61}$$

while the bare Green's function is given by

$$\hat{\mathbf{G}}^0(\mathbf{k},\varepsilon) = \frac{1}{\varepsilon - \varepsilon_{\mathbf{k}} + i\eta} \tag{1.62}$$

Diagrammatically, this can be understood as follows: the SCBA includes all wigwam and nested wigwam diagrams in the self-energy (Figure 1.8 b)-d)), but ignores crossed

---

[7] The proper derivation of this formula involves an analytic continuation from the imaginary time axis to the real time axis. Furthermore, this form of the SCBA is derived specifically for the Gaussian disorder model introduced above.

wigwam diagrams (Figure 1.8 e)). Hence, it is also sometimes called “non-crossing” approximation. While in Figure 1.7 we also showed three-legged wigwam diagrams, they turn out to give zero contribution in the case of Gaussian disorder as introduced in 1.2.1 as the third moment of a Gaussian distributed variable x is 0. The higher order momenta can be expressed in terms of mean and variation of the Gaussian distribution, and therefore we can also ignore wigwam diagrams with four or more legs[AM07, chapter 3]. One can show that the SCBA is a good approximation when $\frac{1}{k_F l} \ll 1$, with l the scattering length and k_F the Fermi wave vector. This condition is usually fulfilled in metals. As for Weyl semimetals the Fermi vector $k_F = 0$, this condition is not fulfilled and the SCBA is not a formally well controlled approximation. Nonetheless, good (qualitative) results for Weyl semimetals were obtained using the SCBA approximation before[Sbi+14]. These were confirmed by other methods as well, albeit the quantitative results are not expected to correspond to real experimental values.

1.3. Interactions and mean field approximation

Until now we discussed electrons moving in a crystalline solid that might be disordered, but we neglected interaction effects between the electrons. Here we introduce the mean field theory to take interactions into account, and we follow the presentation of [BF04, chapter 4].

A quantum system described by a single number operator $\hat{n}_a = a^\dagger a$, i.e. a quadratic Hamiltonian in creation/annihilation operators, can be described in a single particle picture. Multiple particles in the same system are independent of one another and, according to their quantum statistics, fill the available single particle states beginning at the lowest energy. Once we include some interaction in the system, it can be written generically[8] as

$$H = H_0 + V_{\text{int}} \tag{1.63}$$

$$H_0 = \sum_{c\in\{a,b\},\xi} \left(\varepsilon_\xi c_\xi^\dagger c_\xi\right) \tag{1.64}$$

$$V_{\text{int}} = V_{\nu\mu,\nu'\mu'} \hat{A}\hat{B} \tag{1.65}$$

$$\hat{A} = a_\nu^\dagger a_\nu' \tag{1.66}$$

$$\hat{B} = b_\mu^\dagger b_\mu' \tag{1.67}$$

for two different species of particles a and b, where H_0 is the single-particle part of the Hamiltonian and V_{int} is quartic in creation/annihilation operators. Interactions between the same species of particles will be discussed below. To find the mathematically exact solution of this Hamiltonian we would have to solve the full many-body problem. Solving

---

[8] This is the generic two-body interaction, on which we focus here. Interactions including three or more particles are also possible, but less common and not discussed here.

these many-body problems is very hard in general[9], therefore one often resorts to the use of approximations.

The idea of the mean field approximation is to decompose both operators $\hat{A}$ and $\hat{B}$ figuring in V_{int} into their mean and fluctuations around the mean as

$$\hat{A} = \langle A \rangle + \hat{\delta}_A \tag{1.68}$$

$$\hat{B} = \langle B \rangle + \hat{\delta}_B \,. \tag{1.69}$$

Substituting this into (1.65), where we assumed that $\hat{A}$ and $\hat{B}$ describe different particles, results in

$$\begin{aligned}\hat{A}\hat{B} &= \langle A \rangle\langle B \rangle + \langle A \rangle\hat{\delta}_B + \hat{\delta}_A\langle B \rangle + \hat{\delta}_A\hat{\delta}_B \\ &= \langle A \rangle\langle B \rangle + \langle A \rangle(\hat{B} - \langle B \rangle) + (\hat{A} - \langle A \rangle)\langle B \rangle + \hat{\delta}_A\hat{\delta}_B \\ &= \langle A \rangle\hat{B} + \hat{A}\langle B \rangle - \langle A \rangle\langle B \rangle + \hat{\delta}_A\hat{\delta}_B\end{aligned} \tag{1.70}$$

which is still exact. The mean field approximation consists of neglecting $\hat{\delta}_A\hat{\delta}_B$, leading to

$$\hat{A}\hat{B} \approx \langle A \rangle_{\text{MF}}\hat{B} + \hat{A}\langle B \rangle_{\text{MF}} - \langle A \rangle_{\text{MF}}\langle B \rangle_{\text{MF}} \,. \tag{1.71}$$

The rationale behind this approximation is the following: Assuming that the fluctuations of $\hat{A}$ and $\hat{B}$ around their mean value are small, we expand in orders of the fluctuations and only keep the terms to first order in the fluctuations while neglecting the second order terms. In neglecting the product of the fluctuations $\hat{\delta}_A\hat{\delta}_B$ we turned the many-body problem into a single particle one, as $\langle A \rangle$ and $\langle B \rangle$ are just numbers and not operators. The means $\langle \ldots \rangle_{\text{MF}}$ in equation (1.71) have to be evaluated self-consistently with respect to the Hamiltonian computed in the mean field approximation. This procedure of determining $\langle A \rangle$ and $\langle B \rangle$ is equivalent to minimizing the free energy of the system[BF04, page 67].

This result has to be adapted when $\hat{A}$ and $\hat{B}$ act on the same kind of particles. Then we can write the interaction as

$$V_{\text{int}} = \frac{1}{2} \sum_{\nu\nu',\mu\mu'} \left(V_{\nu\mu,\nu'\mu'} c^\dagger_\nu c^\dagger_\mu c_{\mu'} c_{\nu'} \right) \tag{1.72}$$

and for fermions the approximation becomes

$$\begin{aligned}c^\dagger_\nu c^\dagger_\mu c_{\mu'} c_{\nu'} \simeq\ & c^\dagger_\nu c_{\nu'} \langle c^\dagger_\mu c_{\mu'} \rangle_{\text{MF}} + \langle c^\dagger_\nu c_{\nu'} \rangle_{\text{MF}} c^\dagger_\mu c_{\mu'} \\ & - c^\dagger_\nu c_{\mu'} \langle c^\dagger_\mu c_{\nu'} \rangle_{\text{MF}} - \langle c^\dagger_\nu c_{\mu'} \rangle_{\text{MF}} c^\dagger_\mu c_{\nu'} \\ & - \langle c^\dagger_\nu c_{\nu'} \rangle_{\text{MF}} \langle c^\dagger_\mu c_{\mu'} \rangle_{\text{MF}} + \langle c^\dagger_\nu c_{\mu'} \rangle_{\text{MF}} \langle c^\dagger_\mu c_{\nu'} \rangle_{\text{MF}} \,.\end{aligned} \tag{1.73}$$

---

[9] The dimensionality of the Hilbert space grows exponentially with the number of particles.

For bosons, the equations have the same structure with plus signs only, but in this thesis we will only consider fermions.

By using equation (1.71) or (1.73) we effectively reduced the many-body problem to a single-particle problem, at the cost of finding a self consistent solution of the new effective Hamiltonian that includes mean values taken with respect to this Hamiltonian itself.

A subtlety in applying the mean-field approximation is the appropriate choice of the means to consider. A choice is necessary, as there is a large number of possible means to look at. Often, we can identify the relevant means based on the system's symmetries. On the other hand, interactions can lead to spontaneously broken symmetries, and depending on the means chosen, one might not be able to identify such phases. Then again, we can assume some symmetry breaking and study the corresponding mean field approximation. An example of such a symmetry broken phase is a periodic spatial variation of charge densities as studied in chapter 4. Usually, one allows for some variational parameters in the mean field approximation to optimize the mean field solution in this parameter space. Introducing a specific breaking of symmetries, of course, excludes the possibility of finding different symmetry broken phases, but it allows us to decide whether the symmetry breaking actually occurs (and results in a non-zero mean) or not (resulting in a mean equal to zero).

1.4. Topology in condensed matter

1.4.1. Topological phases

Before the discovery of topological phases it was believed that Landau's theory of spontaneous symmetry breaking was sufficient to classify all possible phases. In Landau's theory an ordered phase is identified by a local order parameter and phase transitions manifest themself as changes of this order parameter from zero (in the phase respecting the symmetry) to nonzero (in the symmetry broken phase). In this theory, phase transitions are called nth order transition when the nth derivate of the free energy is discontinuous across the transition. But in the 1980's it was realized that there are phases that can only be distinguished by a global property[Tho+82; Hal88; BH13], while there is no local order parameter telling the two phases apart. These phases are called "topological phases", and in 2016 the Nobel Prize was awarded to D. J. Thouless, F. D. M. Haldane and J. M. Kosterlitz "for theoretical discoveries of topological phase transitions and topological phases of matter"[THK]. A property common to all topological phases is their stability against local perturbations. Put differently, two topologically different phases cannot be changed into each other by local perturbations[10]. Regarding

---

[10] This concept can be extended to "symmetry protected topological phases" (SPT), which are stable against local perturbations as long as they obey some symmetries, that are then said to stabilize the topological phase. These phases are important in condensed matter physics as crystalline materials often have discrete translational or rotational symmetries that can lead to SPT phases.

the key properties of topological phases, different communities in physics place different emphases: In the many-body framework, the key characteristic of a topological phase is a degenerate (many-body) ground state on top of which exist fractionalized excitations and said degeneracy of the ground state acts as topological index. In the single particle picture, the topological index is defined in terms of the (single-particle and gapped) eigenstates. At the boundary of two phases with different topological index, there are always gapless states, a general property known as "bulk-boundary correspondence". As the vacuum is topologically trivial, this notably includes any surface of a topological material. For different classes of topological phases, there exist different topological indices[Ryu+10], for example the Chern number[Tho+82] as introduced formally in chapter 1.4.2. The Chern number can be understood as being analogous to the genus of a closed surface. The genus of a closed manifold corresponds intuitively to "the number of holes" in a shape. For example the genus of a sphere is 0, a donut has genus 1 and a pretzel has genus 3, see Figure 1.10. Mathematically, the genus can be determined using the Gauss-Bonnet theorem of differential geometry.

Figure 1.10.: Closed manifolds of different shapes, with genus 0, 1 and 3 from left to right.

In this thesis we consider the single particle picture and subsequently introduce the Chern number together with the quantum Hall effect.

1.4.2. IQHE and the Chern number

A prime example of a topological phase is the (integer) quantum Hall effect, where a two-dimensional electron gas subject to a perpendicular magnetic field develops a quantized Hall conductance

$$\sigma_{xy} = \frac{e^2}{h}\nu \tag{1.74}$$

where e^2/h is the conductance quantum and ν is an integer called Chern number which will be introduced in more detail below. The experimental setup to observe the Quantum Hall effect is schematically equivalent to the setup depicted in Figure 1.3. While the Quantum Hall effect requires an external magnetic field, it turns out that there is also the possibility of having a quantized Hall effect without the need for an external magnetic field[Hal88], called quantum anomalous Hall effect[LZQ16], which again can be understood in terms of Berry phase and Chern number. Further, a fractional quantum Hall effect exists, leading to quantized conductance values of simple fractions (i.e 1/3, 2/5 etc.) of the conductance quantum. This effect can only be understood in a many-body framework and will not be discussed in more detail here.

When the quantization of the integer quantum Hall effect was first derived by Thouless, Kohmoto, Nightingale and den Nijs[Tho+82], it was named TKNN-invariant. It turns out that this TKNN invariant is just the Chern number[Sim83]. In the following we show how the Chern number is computed for systems with a given Hamiltonian H.

Berry Phase

In a seminal paper, M.V. Berry introduced in 1984[BS84] the "geometrical phase", which nowadays is called Berry phase. Here, we will follow the derivation and notation of [XCN10]. The Berry phase arises during an adiabatic change of a quantum state and is gauge invariant for cyclic changes. This adiabatic change takes place along a path $\mathcal{C}$ in paramter space which is traversed in time t. The parameter in this space is called $\mathbf{R}$. We can write the Hamiltonian and its eigenstates as

$$H(\mathbf{R})\left|n(\mathbf{R})\right\rangle = \varepsilon_n(\mathbf{R})\left|n(\mathbf{R})\right\rangle, \tag{1.75}$$

where ε_n is the n^{th} eigenvalue of the Hamiltonian and these eigenvalues are ordered from smallest to highest value. Solving formally the time dependant Schrödinger equation and using the adiabatic theorem[11] we get the time-dependent eigenstate

$$\left|\Psi_n(t)\right\rangle = e^{i\gamma_n t}\exp\left[-\frac{i}{\hbar}\int_0^t dt'\varepsilon_n(\mathbf{R}(t'))\right]\left|n(\mathbf{R}(t))\right\rangle \tag{1.76}$$

where the second exponential term appears in the usual solution of the time dependent Schrödinger equation, whereas γ_n is the Berry phase

$$\gamma_n = \int_{\mathcal{C}} d\mathbf{R}\cdot\mathcal{A}_n(\mathbf{R}), \tag{1.77}$$

where

$$\mathcal{A}_n(\mathbf{R}) = i\left\langle n(\mathbf{R})\right|\frac{\partial}{\partial\mathbf{R}}\left|n(\mathbf{R})\right\rangle \tag{1.78}$$

---

[11] The adiabatic theorem states that under a "slow" (i.e. adiabatic) change of the Hamiltonian, a particle starting out in the eigenstate $n(0)$ remains in eigenstate $n(t)$ throughout time and does not transition into any other state.

is the Berry connection. It might seem that both γ_n and $\mathcal{A}$ are unphysical as they are gauge dependent, but for cyclic adiabatic changes, where γ_n is calculated along a closed loop, any gauge transformation can change γ_n only by multiples of 2π. Hence for closed paths $\gamma_n \mod 2\pi$ becomes a quantity of physical relevance. The value of γ_n only depends on the geometry of the closed path and the actual time dependence of $\mathbf{R}$ is no longer important.

Berry Curvature

We can further introduce the Berry curvature as a gauge field tensor[XCN10, p. 5]

$$\begin{aligned}\Omega^n_{\mu\nu}(\mathbf{R}) &= \frac{\partial}{\partial R^\mu} A^n_\nu(\mathbf{R}) - \frac{\partial}{\partial R^\nu} A^n_\mu(\mathbf{R}) \\ &= i \left[\left\langle \frac{\partial n(\mathbf{R})}{\partial R^\mu} \middle| \frac{\partial n(\mathbf{R})}{\partial R^\nu} \right\rangle - (\nu \leftrightarrow \mu) \right] \end{aligned} \tag{1.79}$$

which can also be written in vector form if the parameter space is three-dimensional:

$$\boldsymbol{\Omega}_n(\mathbf{R}) = \nabla_{\mathbf{R}} \times \mathcal{A}_n(\mathbf{R}) \,. \tag{1.80}$$

Using this notation it is easy to apply Stoke's theorem and replace the line integral of the Berry phase (1.77) by a surface integral

$$\gamma_n = \int_{\mathcal{S}} d\mathbf{S} \cdot \Omega_n(\mathbf{R}) \,, \tag{1.81}$$

where $\mathcal{S}$ is a surface with border $\delta\mathcal{S} = \mathcal{C}$. It is noteworthy that while the Berry connection is gauge dependent the Berry curvature is independent of the gauge and directly related to physical observables.

Chern Number

When we integrate the Berry curvature over a closed manifold in parameter space the result is an integer multiple of 2π, according to the Chern-Gauss-Bonnet theorem[Che45]. This integer is called Chern number and can be obtained using (1.81) where $\mathcal{S}$ is now a closed manifold. While the Berry phase is only determined modulo 2π on a path $\mathcal{C}$, for a closed manifold $\mathcal{S}$ the border is vanishing and the integral is no longer gauge dependent. For the band structures of lattice models the Chern number ν refers to the case where $\mathbf{R}$ is chosen as the momentum $\mathbf{k}$ and the Berry curature is integrated over the full Brillouin zone.

$$\nu = \int_{BZ} \mathrm{d}^2\mathbf{k} \, \Omega_{12}(\mathbf{k}) \,, \tag{1.82}$$

with Ω as defined in (1.79), $R_1 = k_x$ and $R_2 = k_y$. The Chern number is computed for a two-dimensional system in momentum space, hence can formally only be computed for an infinite system or one with periodic boundary conditions. Further the spectrum needs to be gapped for the Chern number to be well defined. Once we consider a finite sample of systems with non-zero Chern number, we will find states localized at the edges and crossing the gap. This is a manifestation of the bulk-boundary correspondence mentioned earlier.

Numerical Calculation

While an analytic solution of (1.79) might be feasible for small models with few bands, it quickly becomes very difficult for larger and more complicated models. To actually calculate the Berry curvature and Chern number using (1.79) we need to know the eigenstate and its derivatives for the band we are interested in (denoted with n). If the analytic solution to the eigenstates is not known, the derivative has to be taken numerically. This is generally hard due to the gauge freedom of the eigenstates which in usual numerical codes is determined randomly at each point in k-space.

Fortunately, there exists an alternative formulation of the Berry curvature using a summation over all eigenstates of the systems[XCN10]

$$\Omega^n_{\mu\nu}(\mathbf{R}) = i \sum_{n' \neq n} \frac{\langle n| \frac{\partial H}{\partial R^\mu} |n'\rangle \langle n'| \frac{\partial H}{\partial R^\nu} |n\rangle - (\nu \leftrightarrow \mu)}{(\varepsilon_n - \varepsilon_{n'})^2} . \tag{1.83}$$

This equation only requires the derivatives of the Hamiltonian with respect to $\mathbf{R}$ and we do not need to compute the derivative of the eigenstates. For these reasons, equation (1.83) is well suited for numerical calculations and will be used in all numerical computations of the Chern number (1.82) in this thesis.

In the following chapter we introduce Weyl semimetals, where we will also explain the connection of a gapless semimetall to the Chern number defined for gapped band structures.

1.5. Weyl semimetals

In 1928, Paul Dirac proposed an equation describing massive spin-1/2 relativistic[12] particles in quantum mechanics[Dir28]. This equation involves 4-component wave functions and 4 × 4 matrices. It can be seen as an adaptation of the Schrödinger equation to special relativity. One year later, Hermann Weyl realized that in order to describe massless spin-1/2 particles, a real-valued 2-component equation is sufficient, splitting the Dirac equation into two parts of different chirality[Wey29]. Soon after, this equation was called the Weyl equation. It might not be obvious at first sight, how an equation from the context of high-energy and particle physics relates to current research in condensed matter

---

[12] The Dirac equation respects special relativity, the problem of unifying general relativity and quantum mechanics is a central problem of modern theoretical physics.

physics. While there are no elementary particles known to be Weyl fermions[13], they can be realized as quasiparticles in crystalline materials. The concept of quasiparticles is common in condensed matter physics, when the real electrons interact with the crystal or among one another. Their effective behaviour can be described in terms of fictitious quasiparticles behaving as if they were weakly interacting particles in free space. Hence in Weyl semimetals the behaviour of the electrons can effectively be described by quasiparticles obeying the Weyl equation.

Although as early as in 1937 there was a proposal of realizing Weyl fermions as quasiparticles in crystals[Her37], it was only seventy years later that this idea was again considered[Mur07], followed by many theoretical proposals on material realizations[Vol09; Wan+11; BB11]. Very recently some of these materials were realized in experiments and shown to be Weyl semimetals[Xu+15; Lv+15; Lu+15].

1.5.1. Weyl equation in condensed matter

In condensed matter systems, Weyl fermions arise due to a linear band crossing that can effectively be described by

$$H = \hbar v \left(\boldsymbol{\sigma} \cdot \mathbf{k} + \mathbf{a} \cdot \mathbf{k} \right) \tag{1.84}$$

resulting in the dispersion relation

$$E = \hbar v \left(\mathbf{a} \cdot \mathbf{k} \pm \sqrt{k_x^2 + k_y^2 + k_z^2} \right) , \tag{1.85}$$

where v has dimensions of velocity, $\hbar$ is the reduced Planck constant, $\boldsymbol{\sigma}$ is the vector of Pauli matrices in the basis of the two crossing bands and $\mathbf{a}$ is the dimensionless tilting parameter that will play a prominent role in the following chapters of this thesis. In actual materials these Weyl cones cannot appear around $\mathbf{k} = 0$, so in equations (1.84) and (1.85) $\mathbf{k}$ has to be understood relative to the position $\mathbf{k}_0$ of the Weyl cone in momentum space. This effective Hamiltonian is exactly the one Hermann Weyl derived for the massless relativistic (elementary) particles. Due to the conical dispersion (1.85), as shown in Figure 1.1, one often talks of "Weyl cones" in the context of condensed matter systems.

The most general description of a Weyl dispersion replaces $v\boldsymbol{\sigma} \cdot \mathbf{k}$ in (1.84) with an anisotropic velocity tensor $v_{ij}\sigma_i k_j$, but as we will show in chapter 2 (see also [Tre+15]) most of the effects of this anisotropic velocities can be understood in terms of simple coordinate rescalings. The term $\mathbf{a} \cdot \mathbf{k}$ produces an overall tilt of the Weyl cone, as shown in Figure 1.1. Such a tilt is generally to be expected in real Weyl semimetals, as it is not prohibited by any symmetries. In the article [Ber+15] we discussed the possibility of tilted Weyl cones and studied the case of interacting electrons in Wely bands that are so strongly tilted that they become flat. The publication [Tre+15], which was prepared

---

[13] For a long time neutrinos were thought to be Weyl fermions, but in 1998 they were found to have a tiny mass[Bil16].

during the work on this thesis and whose results are presented in chapter 2, was the first one to discuss the consequences of such a tilting term on the transport properties. It was also the first work to specifically point out the previously ignored importance of the tilt.

The stability of Weyl cones, which is due to their topological nature, can be intuitively understood considering the two band Hamiltonian (1.84). Since in the Hamiltonian all possible Pauli matrices are multiplied with a momentum component, it is not possible to add a term that gaps out the Weyl cone: at most the location k_0 of the Weyl cone is altered. This is in contrast to the two-dimensional graphene, where the effective Hamiltonian of the Dirac cone only contains two Pauli matrices and the addition of a local term proportional to the third Pauli matrix gaps out the Dirac cone in two dimensions.

1.5.2. Symmetries in topological phases and Weyl semimetals

For gapped topological phases (topological insulators), there exists a classification of possible topological invariants based only on dimensionality and symmetries of the system under consideration. This classification only uses the three symmetries of inversion, time-reversal and charge conjugation and is also known as the 10-fold way[Ryu+10]. Further, topological phases exist, which are protected by additional crystalline symmetries. These phases are called “symmetry protected topological phases” (SPT)[Sen15].

Weyl semimetals are different from these gapped phases, as they explicitly require the breaking of some symmetry[HQ13]: It is important for the topological stability of the Weyl cones, that the linearly crossing bands are non-degenerate. According to Kramers theorem[Kra30; Wig32], all states would be doubly degenerate when time-reversal symmetry and inversion symmetry are present. Therefore, at least one of these two symmetries must be broken in a Weyl semimetal, otherwise the Weyl points would be degenerate and then combine to form less stable and not topologically protected Dirac points. A second consequence of these considerations is that Weyl cones usually appear away from high symmetry points of the Brillouin zone. This might be one of the reasons why Weyl semimetals were not observed earlier.

The Weyl equation was originally proposed in the context of relativistic elementary particles, and therefore was formulated to be Lorentz invariant. Requiring Lorentz invariance rules out anisotropic velocities and also the tilt term $\mathbf{a}$, as both these generalizations break rotational invariance. However, in the context of quasiparticles in a condensed matter system the Lorentz invariance itself is not crucial. We are more interested in the topologically protected linear band crossing that possibly, and in material realizations quite generally, includes anisotropic velocities and a tilt[Ber+15; Tre+15; Sol+15]. This directly connects to the main objective of this thesis: We will study how this tilt term affects (transport) properties of Weyl semimetals while it does not change the basic topological index of Weyl cones.

1.5.3. Chirality and topological index

Since Weyl cones are gapless, a connection to the topological invariants discussed above for gapped band structures might not be obvious at first sight, but there *is* a simple correspondence: the surface of a sphere in (three-dimensional) momentum space gives a two-dimensional "cut" of the band structure. When the gap closing of the Weyl cone is inside the bulk of this sphere, the two bands of the Weyl cone are gapped on the sphere's surface and the Chern number is well defined as introduced above. This Chern number corresponds directly to the chirality of the Weyl cone denoted with χ for an electronic band (the one with positive energy in the case of zero chemical potential relative to the Weyl node) respectively $-\chi$ for the hole band[HQ13]. In the case of multiple Weyl cones this Chern number corresponds to the sum of the chirality of all Weyl cones inside the sphere. This is an important property when searching (numerically) for Weyl cones in complex three-dimensional band structures by moving a "probe" sphere through momentum space: a result of Chern number zero can correspond to no Weyl cone at all or to a pair of Weyl cones of opposite chirality. Therefore, one needs to apply some care in using this property as a diagnostic tool to find Weyl cones. As Weyl cones have a fixed chirality and at the same time the total chirality of a system must be zero, Weyl cones have to come in pairs of opposite chirality that are separated in momentum space. When two Weyl cones of opposite chirality "meet" in momentum space, they become a Dirac cone, where both linear bands are doubly degenerate. Further, Weyl cones of opposite chirality are related by symmetry, and therefore Weyl cones cannot appear at $\mathbf{k} = 0$.

1.5.4. Transport

When a new class of materials is discovered, their transport properties are of great interest, both for experimental verification of material candidates and in the search for applications. Weyl semimetals are special as they posses a topologically protected band crossing, where the density of states vanishes. How this topological feature affects transport properties was studied in many contexts: The conductance properties including the influence of potential disorder were discussed in [Sbi+14; PML15; Che+15], while [RS15a] considered charge impurities. Further, the critical exponents of the disorder phase transition were calculated by [SRG15; SBB15], while others argued that rare region effects lead to an avoided quantum critical point at this phase transition[NHS14]. Adding a magnetic field to the picture leads to magnetoresistance[Bur15; KGM15], magneto-thermal effects[SGT16] and curious "non-local" phenomena[Bau+15; RKL17; Par+14].

While there were numerous articles available about the transport properties of Weyl semimetals in 2014 when I began to work on this thesis, the articles listed above only considered the idealized isotropic Weyl cone, with the only exception [RKN15] taking into account anisotropies of the Weyl cones in the conductivity calculation. To the best of our knowledge, the effects of a tilt were never discussed before our work [Tre+15;

Tre+17b], corresponding to the results presented in chapters 2 and 3. These articles consider the conductivity of a Weyl semimetal with the Fermi energy at the energy of the nodal point. The “classical” intuition tells us that the conductivity must vanish, as the density of states vanishes. While this turns out to be correct, there is a non-vanishing cube conductance g as introduced in (1.8) and therefore the conductance is finite. Due to the topological stability of the Weyl cone the addition of potential disorder does not directly increase the conductivity to a non-zero value, but there is a critical disorder strength at which a phase transition to a “disordered phase” occurs[Sbi+14]. Further, for isotropic Weyl cones it was found that the Fano factor (see (1.10)) takes a unique value of

$$F = \frac{1 + 2\ln 2}{6\ln 2}, \tag{1.86}$$

in the “clean” phase, while it takes the well-known value 1/3 in the disorderd phase and thus can serve as an indicator distinguishing the clean and the disordered phase. These properties will be discussed in more detail in chapters 2 and 3, where we study if the addition of anisotropy and a tilt changes the conductivity and the Fano factor.

Chiral anomaly

Another prominent transport property of Weyl semimetals is the chiral anomaly[HQ13]. For a single Weyl cone of chirality χ the current in a magnetic field is given by

$$\partial_\mu \mathbf{j}^\mu_\chi = -\chi \frac{e^3}{4\pi^2\hbar^2} \mathbf{E} \cdot \mathbf{B}\,, \tag{1.87}$$

where E is an electric and B a magnetic field and thus the current would not be conserved when E and B have a parallel component. This obvious contradiction to current conservation can be resolved by considering the complete system consisting of pairs of Weyl cones of opposite chirality and hence, current conservation is restored in total. The chiral anomaly still results in a measurable quantity, namely the anomalous Hall effect, which for a system with two Weyl cones is

$$\mathbf{j} = \frac{e^2}{2\pi^2\hbar^2} \mathbf{b} \times \mathbf{E} + \frac{e^2}{2\pi^2\hbar^2} b_0 \mathbf{B}\,, \tag{1.88}$$

where $\mathbf{b}$ is the momentum space separation of the two Weyl cones and b_0 is their separation in energy. Several experiments confirmed this effect in transport measurements[Hua+15; Zha+16]. Furthermore, a chiral magnetic effect[HQ13] exists.

1.5.5. Fermi arcs

A further interesting feature of Weyl semimetals are their surface states, called Fermi arcs[HQ13; Fan+16; PKV14; Oja13]. In usual materials, the Fermi surface on a two-dimensional surface is a closed circle, up to deformations. In Weyl semimetals the Fermi

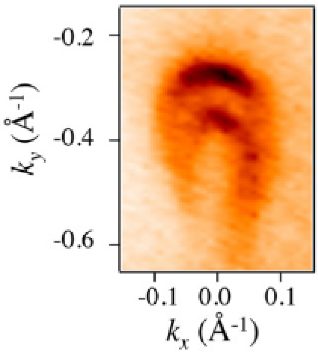

Figure 1.11.: Experimental observation of a Fermi arc state using Angle resolved photo emission spectroscopy (ARPES), taken from [Xu+15]. The darker tones correspond to the Fermi arcs that do not form a closed circle but end abruptly at two ends.

surface is “fractionalized” and only half of the usual Fermi circle lives on one surface, while the other half can be found on the opposed surface.[14] This Fermi arc starts and ends at surface projections of the Weyl cones. Figure 1.11 shows the experimental observation of a Fermi arc.

The following picture provides an intuitive explanation for the existence of Fermi arcs: If a two-dimensional momentum-space plane orthogonal to the vector connecting the Weyl points is moved along this vector, its Chern number changes when it crosses through a Weyl point, as each Weyl point radiates Chern flux[15]. We assume that this plane starts as topologically trivial at the BZ's boundary and moves along the direction in which the Weyl cones are separated. When it encounters the first Weyl point, it changes to be topologically nontrivial with Chern number ±1 and hence has gapless edge states. Once it encounters a Weyl point of opposite chirality it switches back to being topologically trivial. Combining all the edges of the two-dimensional sheets to construct the surface of a three-dimensional sample, these gapless edge states result in the Fermi arc and it is obvious that the Fermi arc connects the Weyl point surface projections[HQ13].

In [KTB17] we constructed exact solutions for topological surface states, including surface states in Weyl materials that lead to Fermi arcs. This construction is quite general and only relies on the lattice structure and some weak assumptions (locality and translation invariance) on the hopping elements of the tight-binding model. In Figure 1.12 an exemplary lattice is shown together with the inverse localization length $\xi^-1(\mathbf{k}) = \log|r_1(\mathbf{k})|$ for the lowest energy surface state in the pyrochlore model for the 2-in-2-out spin configuration. The hopping parameters are $t_{SOC}/t = 0.1$ as defined in

---

[14] In known materials, the Fermi circles split in two half-circles[Xu+15], but it is theoretically possible to split it into even shorter pieces[KTB17].

[15] Due to the periodicity of the BZ this plane is equivalent to the sphere on which we defined the Chern number of a Weyl point above.

[KTB17]. In the areas colored red, the surface state is localized to the bottom surface, while it is located to the top surface in the blue areas. The black line is the Fermi surface, which switches surface two times (where it crosses from red to blue areas or vice versa). The tight-binding model was obtained as projection to the 2-in-2-out spin configuration of a spinful model given in [YI14], other cases are also discussed in [KTB17].

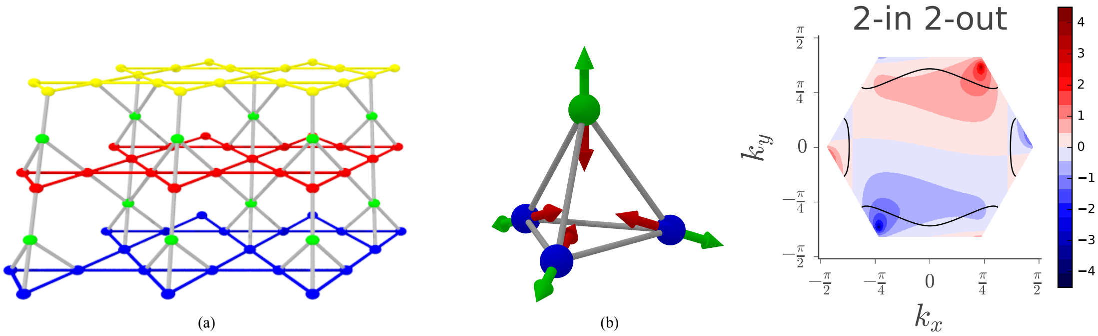

(a)

(b)

Figure 1.12.: (a) The pyrochlore model consists of layers of kagome lattices stacked alternating with a triangular lattice (green). The kagome layers are shifted relative to each other and repeat every third layer. (b) A single tetrahedron of the pyrochlore lattice. The arrows indicate the preferred spin directions pointing towards (red) or away from (green) the center of a tetrahedron.

1.6. Numerical methods and computer programs

In all projects of this thesis numerical calculations were performed. The numerical applications range from integration of formulas obtained analytically for which an exact integration was not possible, over self-consistent solutions of (nonlinear) equations for the mean field calculations and the SCBA computations, to high-performance computations for disorder averages in the S-Matrix approach. All computer codes for this thesis were written in the Python programming language, using the packages numpy[WCV11] and scipy[Oli07] for numerical work and pandas[McK10] for the analysis of the data obtained during the computations. I developed a private python package to quickly study (topological) lattice models, especially in conjunction with the project [KTB17].

A common and ubiquitous problem in numerical work is to make sure that the results do not depend on numerical (i.e. unphysical) parameters. Such parameters include for example a (numerical) cutoff or the resolution used in the discretization of continuous variables. A general strategy to verify convergence is the following: starting with low values of the numerical parameter, where the result still (erroneously) depends on the parameter, one slowly increases the parameter until the result becomes independent of the parameter. In general, we verified numerical convergence for all computations. Due to the large number of numerical parameters and the repetitive nature of the convergence verification procedure, the exact convergence behaviour is not always discussed in detail.

1.6.1. Chern numbers

A numerical implementation of (1.83) for arbitrary Hamiltonians together with the approach of integration of the dispersion on the two-dimensional sphere's surface in three-dimensional momentum space as described in chapter 1.5, allowed us to quickly verify the chirality and position of Weyl cones in lattice models[KTB17] and to connect exemplary lattice models to low energy models[Tre+15; Tre+17b; Tre+17a].

1.6.2. S-Matrix numerics

In chapter 1.1.5 we introduced the concept of scattering matrices, which we will use in chapters 2 and 3 to numerically compute the conductance and Fano factors of Weyl semimetals. In a clean system where electrons are ballistic, the computation of a scattering matrix amounts to solving a system of linear equations. In this case the transversal modes are independent and we can solve equations (1.34) using a plane wave ansatz for each transverse mode.

To numerically compute the scattering matrix of a disordered system, we use a scheme established in [Bar+07] which was adapted to isotropic Weyl cones in [Sbi+14]. In [Tre+17b] (see chapter 3) this scheme was further adapted to general Weyl cones with anisotropies and tilt as discussed in chapter 1.5. The general idea of this scheme is to obtain the scattering matrix of the full system as the combined scattering matrix of alternating short slices of length Δz of ballistic (clean) transport and infinitesimal slices of disorder, introducing some mixing of the modes. For this approximation to be valid, the parameter Δz has to be much smaller than the correlation length ξ of the disorder given by

$$\xi = \frac{2}{q_0} \tag{1.89}$$

with q_0 as defined in (1.52).

S-matrix for a disorder slice and the Born approximation

To capture the effect of a smooth disorder potential as given in (1.52), we approximate it by using infinitely short slices of disorder placed along the transport direction (here the z axis)[Sbi+14; Sbi16] as

$$V(x, y, z) = \sum_n V_n(x, y)\Delta z \delta(z - z_n) \tag{1.90}$$

with V_n being the average of the corresponding finite slice

$$V_n(x, y) = \frac{1}{\Delta z} \int_{z_{n-1}}^{z_n} \mathrm{d}z V(x, y, z)\,. \tag{1.91}$$

This approximation is valid when we choose $\Delta z \ll \xi$. The scattering matrix then can be computed in the Born approximation, where the reflection part turns out to be 0 due to nonzero wave function overlap. The transmission part is

$$t \simeq 1 + iT \quad \text{with} \qquad T_{nm} = \frac{1}{\hbar} \left\langle \phi^{-}_{Rm} \,\middle|\, V_n(x,y)\Delta z \,\middle|\, \phi^{+}_{Ln} \right\rangle . \tag{1.92}$$

While the Born approximation is good as long as $T \ll 1$, which we can always achieve by choosing an appropriate Δz, it leads to non-unitary scattering matrices. As unitarity is an important requirement for scattering matrices we need to restore it here. We do so by replacing

$$t \simeq 1 + iT \to \left(1 + \frac{iT}{2}\right)\left(1 - \frac{iT}{2}^{-1}\right) \tag{1.93}$$

which is equivalent up to first order, but unitary by construction. The equivalence to first order is sufficient, as we use a first order approximation.

Convergence and details of the implementation

We checked for convergence upon changes of the parameters Δz, the width of the sample (see Figure 1.2) which corresponds to the resolution in momentum space and the momentum cutoff (i.e. the number of modes taken into account) corresponding to the real space resolution. We compared different boundary conditions, notably periodic boundary condition (PBC) and antiperiodic boundary conditions (APBC). The choice of boundary conditions changes the quantization condition, i.e. which transversal wavevectors are allowed. Coinciding results for PBC and APBC are a clear signature of the results' independence of the sample's boundary and therefore a good check when we want to access bulk properties. While it is common to use a square of discretised momenta, where the cutoff is applied to each momentum component individually, we chose to apply the cutoff to the absolute value, leaving us with a circular disc of momenta, a choice that is both physically more sensible and numerically more efficient.

Additionally we developed a version using GPUs (graphics processing unit, known as "graphics cards") for the matrix computation. To this end we wrote a python wrapper for the magma library[TDB10; TDB17].

Combining all the numerical procedures described in this chapter we are able to compute the scattering matrices for disordered systems. An exemplary result of such a calculation is shown in Figure 1.13, displaying the transmission probabilities for one of the disorder realizations, which were used to obtain the results of chapter 2.

1.6.3. SCBA numerics

The SCBA as presented in chapter 1.2.3 leads to a self consistent (matrix) equation that we want to solve numerically. We solve this equation iteratively by repeated and alternating evaluations of the equations (1.60) and (1.61), always using the solution

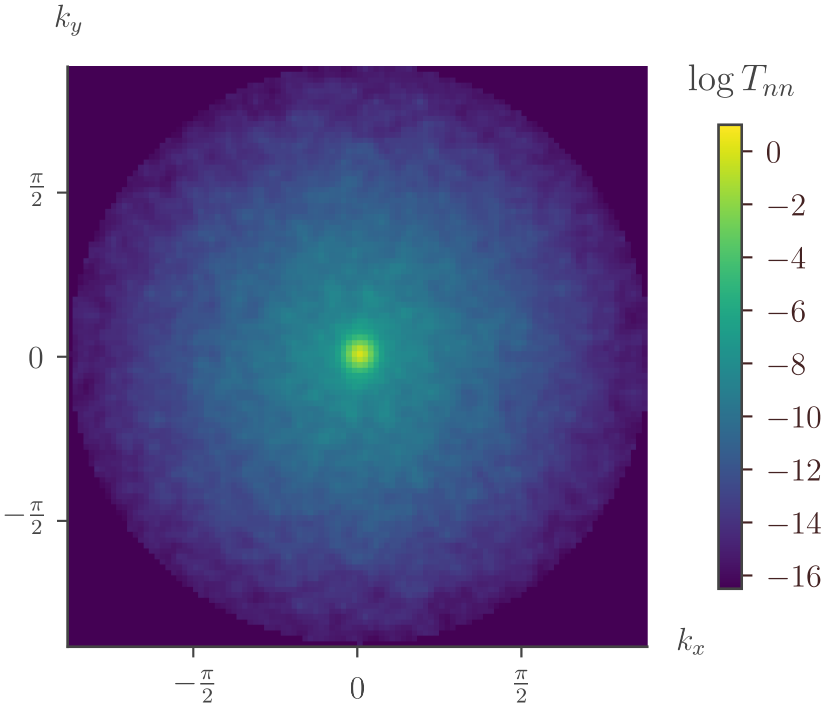

Figure 1.13.: Visualization of the transmission values T_{nn} of the scattering matrix of a disordered system with the following parameters: tilt $a_y = 0.25$, length $L = 20$, width $W = 120$, number of transverse modes $N = 11449$, using the circular momentum cutoff in k_x, k_y. The color scale corresponds to $\log T_{nn}$, showing that the values of T_{nn} at the momentum cutoff have values as low as 10^{-16}.

of the previous step as input. It can be favorable to derive equivalent self-consistency equations for two different quantities (as in [OK14]) to avoid the sharp peak of G that is hard to treat numerically. We stop the iteration once the absolute change (integrated over momentum space) of G falls below a cutoff value defined beforehand.

In the case of a tilted Weyl semimetal we can exploit the rotational symmetry around the direction of the tilt and, working in spherical coordinates k, θ, ϕ, analytically integrate over ϕ, leaving us with only a two-dimensional problem to solve numerically on a k, θ grid. The k-grid runs from 0 to a cutoff k_{max} in steps of dk and the θ grid will be N_θ equally spaced numbers in the range $[0, \pi]$. Further we have to use a small but finite imaginary ε to avoid division by 0.

Once we obtained the final self-consistent $\mathbf{G}$ we can derive an effective clean theory corresponding to the disorder system by matching a $\mathbf{G}_0$ with renormalized parameters to the small $\mathbf{k}$ expansion of $\mathbf{G}$. For the numerical results we use a least-squares fit to a region of small k values adapting the relevant parameters in question, which for chapter 3 are the tilt a and the Fermi velocity v_F. Additionally we check that for small enough k the results do not depend on the precise cutoff used for the fitting procedure. All integrations are numerically performed using the Simpson's rule, that performs a quadratic interpolation of the integrand given at evenly spaced points.

We compute the functions X, Y on a grid in k, θ.

1.6.4. Iterative solution of the mean field equations

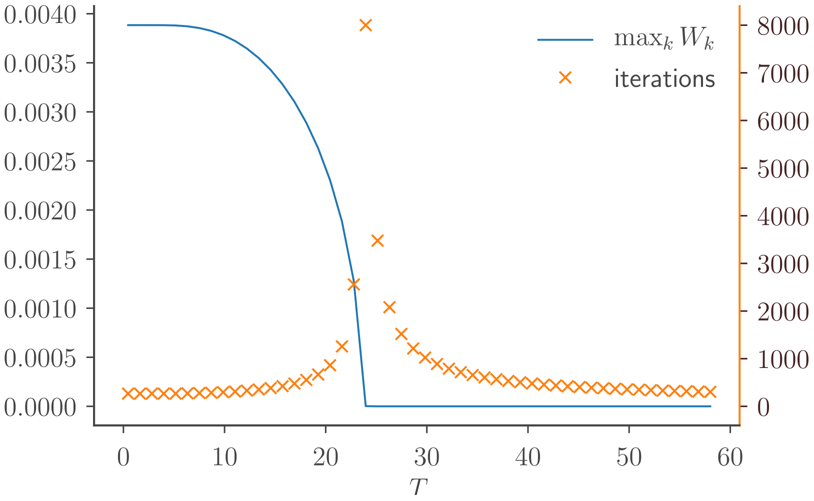

Figure 1.14.: Number of iterations (orange cross) until the mean-field calculation reached convergence over a range of temperatures. The quantity $\max_k W_k$, which is iteratively computed in the mean field calculation, is shown as a blue line (arbitrary units). It is directly related to the order parameter $\langle b^\dagger a \rangle$. The number of iterations is highest at the phase transition.

Solving mean field equations is similar to solving the SCBA equations discussed above, as they also represent a set of self-consistent equations. We use again an iterative approach to solve them. The algorithm that computes the means with respect to some Hamiltonian H and then a new effective Hamiltonian using these means according to equations (1.71) or (1.73) is denoted with $A(H)$. Then the iterative process is to compute $H^j = A(H^{j-1})$, starting with H^0 where some random values for the means are used[16], until $H^j = H^{j-1}$ (up to some defined numerical precision). Unfortunately, this approach is prone to oscillations and therefore it can be helpful to introduce some mixing m and define the Hamiltonian of step j as

$$H^j = (1-m)A(H^{j-1}) + mH^{j-1} \,. \tag{1.94}$$

---

[16] We are looking for a stable solution of the self-consistent equations. Often they have an unstable solution where the mean field is exactly equal to zero. Therefore we have to start with random values for the mean field, since otherwise the iterative algorithm gets stuck at the unstable solution.

We used two approaches relying on the gap equation (only for 2 × 2 problems) and the mean field equation which gave consistent results. Apart from using numerical methods to solve the mean field equations we use the computer algebra system (CAS) SymPy [Meu+17] to derive all the matrix elements of the mean-field expansion in the first place, as this turns out to be a tedious task to do by hand.

Figure 1.14 shows data from the mean field calculation of chapter 4. We display $\max_k W_k$, which is directly related to the order parameter, as W_k is the quantity we evaluate numerically in solving the gap equation. It is defined as

$$W_k = \sum_{k'} UP(k,k')\langle b^\dagger_{k'-Q} a_{k'}\rangle \tag{1.95}$$

in terms of the interaction strength U, the matrix elements P and the operators a and b. All quantities are defined in chapter 4 and appendix C.5 in more detail. The number of iterations needed to reach convergence depends strongly on the distance to phase transition, as shown in Figure 1.14. Away from the phase transition some ten iterations are usually enough, close to the phase transition more and more iterations (up to several thousand) are needed to achieve sufficient convergence.

2. Quantum transport in Dirac materials: signatures of tilted and anisotropic Dirac and Weyl cones

In this chapter, which is based on the publication [Tre+15], we calculate conductance and noise for quantum transport at the nodal point for arbitrarily tilted and anisotropic Dirac or Weyl cones using the Landauer formula introduced in chapter 1.1.5. In [Tre+15] the relevance of the tilt for the properties of Weyl semimetals was mentioned for the first time, a contribution especially acknowledged in the commentary [Bee15]. We emphasize in this chapter, that tilted and anisotropic dispersions are generic in the absence of certain discrete symmetries, such as particle-hole and lattice point group symmetries. These symmetries are generally not present in Weyl semimetals, as discussed in chapter 1.5. We apply our general considerations to specific lattice models of strained graphene and a pyrochlore Weyl semimetal. The conductance properties of type-II Weyl semimetals depend not only on the Weyl cone's dispersion, as in type-I Weyl semimetals, but also on details of the emering finite fermi surface. Therefore we ignore tilts larger than the critical value and do not discuss type-II Weyl semimetals in this chapter. However, it is interesting to note that the tight-binding model of pyrochlore, which serves as an example for type-I Weyl semimetals here, can also be tuned to the type-II phase.

2.1. Introduction

The past decade has witnessed an explosive increase in the study of electronic systems dispersing linearly around isolated band touching points[WBB14]. Notably, this includes graphene[Nov+04; Nov+05], various two-dimensional organic compounds[Goe+08], and the surface states of three-dimensional topological insulators[FKM07; MB07; Roy09; Zha+10]. In three dimensions, a Dirac semimetal[Fan+03; Mur07], which has two coinciding linear band touching points with opposite chirality, was observed experimentally[Liu+14b; Liu+14a], and the first Weyl semimetal[Wan+11; HQ13], which has non-degenerate band-touching points, was observed very recently[Xu+15; Lu+15; Lv+15]. Subsequently the first transport measurements on Weyl semimetals were performed[Hua+15; Zha+15]. A Weyl semimetal phase is also predicted to occur, e.g., in multilayer structures[BB11] and pyrochlore iridates[Wan+11].

By virtue of stochiometry, the Fermi level lies exactly at the nodal point of the low-energy "cones" in many of these materials, and their electronic behavior is neither that of insulators — there is no gap — nor that of conventional metals — there is a vanishing density of states at the nodal point. Indeed it has been shown experimentally[Nov+05; Zha+05] and theoretically[Two+06; Kat06; Bai+14] that the conductivity σ reaches a minimal but finite value at a nodal point in two dimensions, whereas a nodal point in three dimensions is characterized by a finite conductance G, its conductivity σ being zero[Bai+14; Sbi+14]. The Fano factor F, defined as the ratio of shot noise power and current, was found to be an excellent indicator of the quantum nature of electronic transport at the nodal point, taking the universal sub-Poissonian value $F = 1/3$ in graphene[Two+06]. In Weyl semimetals F was found to discriminate between a pseudoballistic regime[Bai+14] at weak disorder and a diffusive regime at strong disorder[Sbi+14]. Unlike the conductance G, which retains a dependence on the ratio W/L of sample width W and sample length L, the Fano factor F is independent of both W and L.

Anisotropy and tilt of the cones are often neglected, essentially for two distinct reasons: (i) they are forbidden by symmetry in important special cases, such as graphene, and (ii) they do not alter the topology of the low-energy theory. Here, however, we demonstrate that tilts and, to a lesser extent, anisotropies lead to clear signatures in quantum transport, affecting both the conductance and the Fano factor in absence of disorder. We find the tilt dependence of the Fano factor F remarkable, because in many cases of interest F was found to be a number with a considerable degree of universality[BB92; JPB94; BM94; Two+06; Bai+14]. Our results apply — with various degrees of numerical relevance — to a number of experimentally relevant systems for which tilted and anisotropic conical dispersion either occur generically, as in the case of Weyl semimetals, or for which the forbidding symmetries are easily broken, such as strained graphene.

2.2. Tilted and anisotropic cones

In the vicinity of a nodal point, a generic Dirac or Weyl Hamiltonian can be written as

$$H = \sum_{i,j} v_{ij} k_i \sigma_j + (a_i k_i - u)\sigma_0, \tag{2.1}$$

where the sum is over $i, j = x, y$ or $i, j = x, y, z$ for dimensionalities $d = 2$ and $d = 3$, respectively. Further $\sigma_{x,y,z}$ are the Pauli matrices and σ_0 is the 2×2 unit matrix. The dispersion is shown schematically in Fig. 2.1. The "tilt" term proportional to a_i is typically discarded, as it does not affect the eigenspinors and, hence, the topology of the band structure. As we show below, inclusion of this term does affect transport at the nodal point, however. Tilts can occur only if particle-hole symmetry is absent, and tilt is additionally constrained by point group symmetries. With a suitable choice of the pseudospin quantization axis, the anisotropy matrix v_{ij} can be brought to upper diagonal form, $v_{yx} = v_{zx} = v_{zy} = 0$. Anisotropies are generic if the cone is not located at a high symmetry point in the Brillouin zone.

Considering graphene as an important example, we note that the trigonal "warping" of Dirac cones respects the crystalline symmetries and leads to anisotropies, but only

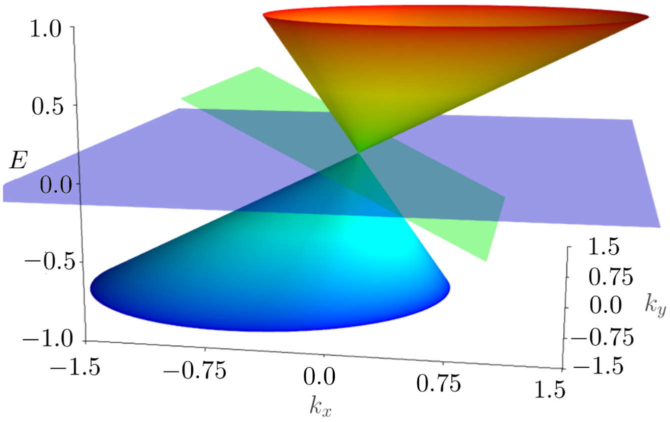

Figure 2.1.: A tilted Dirac cone in two dimensions. The momentum coordinates are labeled k_x and k_y; the third dimension represents energy. Transparent planes indicate zero-energy plane (violet) and tilt $\mathbf{a} = (-0.5, 0)$ (green plane), respectively.

at quadratic order in the momentum k. The anisotropies to linear order (2.1), which amount to a "squeezing" of the cone along some direction, are, just as any tilt of the cone, forbidden by the threefold point group symmetry of the honeycomb lattice, combined with the location of the Dirac cones at high-symmetry points in the Brillouin zone. However, as soon as the threefold rotation symmetry is relaxed anisotropies occur. If, in addition, second-nearest-neighbor hopping is also taken into account the particle-hole symmetry is lost, and the cones acquire finite tilts. This scenario applies to strained graphene and will be discussed in more detail below. For three-dimensional Weyl semimetals, the band touching occur at lower symmetry points; hence anisotropies and tilts are ubiquitous.

2.3. Transport: low-energy theory

We calculate the conductance G and the Fano factor F for a region of length L and width W, taking the limit $W \gg L$ in order to eliminate a spurious dependence on the transverse boundary conditions[Two+06]. We choose the x axis in the transport direction, so that the nodal semimetal corresponds to the region $0 < x < L$, whereas the source and drain leads have $x < 0$ and $x > L$, respectively. The potential u is set to zero for $0 < x < L$, to model transport at the nodal point. We take the limit $u \to \infty$ for $x < 0$ and $x > L$ to model strongly doped leads.

The transverse momentum $k_\perp = k_y$ $(d = 2)$ or $k_\perp = (k_y, k_z)$ $(d = 3)$ is conserved, and for each value of $k_\perp$ we calculate the transmission coefficient $T(k_\perp)$ by matching wave functions in the sample and the leads (see Appendix A for details). The conductance G

per cone is then given by the Landauer formula

$$G = \frac{e^2}{h}\left(\frac{W}{2\pi}\right)^{d-1}\int \mathrm{d}^{d-1}k_\perp T(k_\perp). \tag{2.2}$$

The aspect-ratio dependence can be partially eliminated by changing to the dimensionless conductance referred to a cube, defined by the relations

$$G = \frac{e^2}{h}\left(\frac{W}{L}\right)^{d-1} g. \tag{2.3}$$

In two dimensions g is identical to the conductivity σ. In three dimensions, a finite value for g in the limit $W, L \to \infty$ implies a vanishing conductivity $\sigma = GL/W^2 = (e^2/h)g/L$. The Fano factor, the ratio of shot noise and current, is given by[Büt90]

$$F = \frac{\int \mathrm{d}^{d-1}k_\perp T(k_\perp)(1-T(k_\perp))}{\int \mathrm{d}^{d-1}k_\perp T(k_\perp)}. \tag{2.4}$$

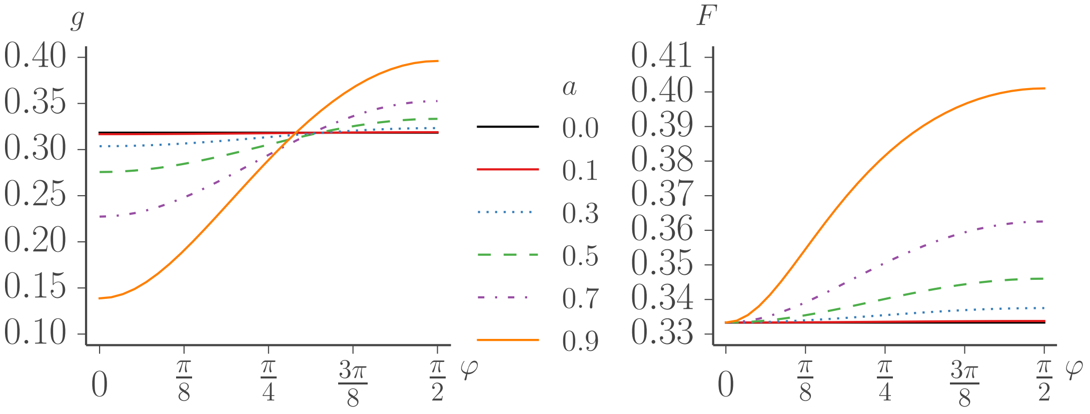

Figure 2.2.: Dimensionless conductance g and Fano factor F for a tilted two-dimensional Dirac cone, as a function of the angle φ between transport and tilt direction. The tilt strength a is given in the legend.

2.3.1. No anisotropy, no tilt

For the isotropic cone without tilt ($a_i = 0, v_{ij} = v_0\delta_{ij}$) the conductance and Fano factor are known from the literature[Two+06; Sbi+14; Bai+14],

$$g = \frac{1}{\pi}, \qquad F = \frac{1}{3}, \qquad (d=2), \tag{2.5}$$

$$g = \frac{\ln 2}{2\pi}, \qquad F = \frac{1+2\ln 2}{6\ln 2}, \qquad (d=3). \tag{2.6}$$

2.3.2. Anisotropy, no tilt

For the general anisotropic case but without tilt, $a_i = 0$, $i = 1, \ldots, d$, one finds

$$g = \frac{1}{\pi} \frac{v_{xx}^2 + v_{xy}^2}{v_{xx} v_{yy}} \qquad (d = 2), \tag{2.7}$$

while the Fano factor is unaffected by the anisotropy; i.e., F is given by Eq. (2.5). For the diagonal case ($v_{xy} = 0$) this result can be understood as a simple scaling of the y coordinate, which affects the conductance g, but not the Fano factor F. In three dimensions the exact result in the diagonal case ($v_{xy} = v_{xz} = v_{yz} = 0$) is given by the corresponding rescaling

$$g = \frac{\ln 2}{2\pi} \frac{v_{xx}^2}{v_{yy} v_{zz}} \qquad (d = 3), \tag{2.8}$$

while there is no simple formula for the general case. Still, the Fano factor remains unaffected by any anisotropy and is given by Eq. (2.6).

2.3.3. No anisotropy, tilted cones

Although a closed analytical solution for a tilted Dirac cone is possible in two dimensions, the explicit expressions are too lengthy to be reproduced here. Instead, we will present a numerical evaluation of the solution for representative values of the tilt parameters a_x, a_y, and a_z for fixed values of $v_{ij} = \delta_{ij}$. Without anisotropy the dimensionless conductance g and the Fano factor depend on the total magnitude $a^2 = a_x^2 + a_y^2$ ($d = 2$) or $a^2 = a_x^2 + a_y^2 + a_z^2$ of the tilt and the angle $\varphi = \arccos(|a_x|/a)$ between the tilt axis and the transport direction only. The limit $a = 1$ corresponds to a maximally tilted cone with a flat band along the tilt direction. Results are shown in Figs. 2.2 and 2.3 for $d = 2$ and $d = 3$ and for representative values of the tilt strength a.

We note that the results are quantitatively different in two and three dimensions, but qualitatively very similar. There is an important difference between a tilt parallel to the transport direction, where g decreases upon increasing the tilt strength, and a tilt perpendicular to the transport direction, where g increases with increasing tilt strength. The Fano factor F is unaffected by a tilt in the transport direction, and increases with increasing tilt if there is a finite angle between the tilt direction and the transport axis. Interestingly, upon averaging over all orientations of the tilt axis, we find a systematic but small decrease in conductance for both two and three dimensions. The main conclusion, however, is that the Fano factor is no longer a universal number once the tilt of the dispersion is taken into account, but depends on the magnitude and direction of the tilt.

The analytical solution for a two-dimensional Dirac cone takes a simple form if the tilt axis and the transport direction are collinear ($\varphi = 0$). In that case one finds $g = (1/\pi)\sqrt{1 - a^2}$, $F = 1/3$. Further, for small tilt strengths it is possible to expand the

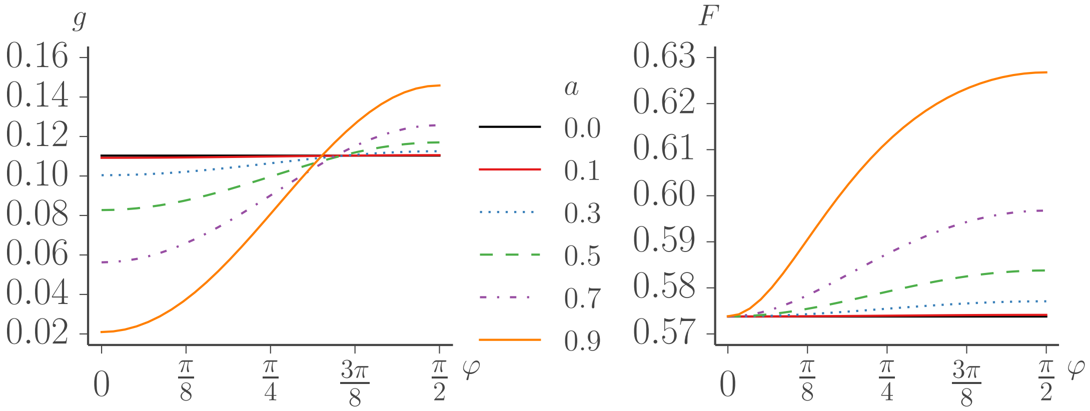

Figure 2.3.: Same as in Fig. 2.2, but for a three-dimensional Weyl cone.

analytical solution in two dimensions. We find

$$g = \frac{1}{\pi} + \frac{a^2}{2\pi}\left(\frac{4}{3}\sin^2\varphi - 1\right) + \mathcal{O}(a^4), \tag{2.9}$$

$$F = \frac{1}{3} + \frac{2a^2}{45}\sin^2\varphi + \mathcal{O}(a^4), \tag{2.10}$$

which deviates less than 1% from the exact value up to $a = 0.5$.

2.3.4. Anisotropy and tilted cones

In the presence of both anisotropy and tilt the dimensionless conductance and the Fano factor are qualitatively similar as in the absence of anisotropy. However, for a tilt in transport direction the Fano factor changes if the anisotropies are not orientated along the axis of the reference frames, i.e., if one of v_{xy}, v_{xz} or v_{yz} is nonzero.

2.4. Application to lattice models

In generic lattice models, the cones are both anisotropic and tilted, and moreover, contributions from an even number of cones must be taken into account simultaneously. Below, we provide explicit results for two specific tight-binding models.

2.4.1. Strained graphene

In “intrinsic,” unstrained graphene the Dirac cones are located at high symmetry points in the Brillouin zone. The application of strain changes the positions of the Dirac points and the cones are no longer protected by crystalline symmetries. Whereas the simplest tight-binding model with nearest-neighbor hopping only is particle-hole symmetric, which rules out a tilt of the Dirac cones, realistic tight-binding models have longer-range hopping, which lifts the particle-hole symmetry[Cha+91]. As an example, we now apply the above calculations to the model of quinoid-type strained graphene, as described by Goerbig *et al.* in Ref. [Goe+08]. Transport properties of strained graphene have been studied earlier[PAP11], but without the inclusion of a tilt of the Dirac cones.

A schematic of the tight-binding model for quinoid-type strained graphene is shown in the inset of Fig. 2.4. It consists of a honeycomb lattice which is extended/compressed in the direction perpendicular to the lattice vector **s**, such that each hexagon has four "short" bonds of length a and two "long" bonds of length a' for positive strain $\epsilon > 0$. Strain is measured in terms of a dimensionless strain parameter $\epsilon = a'/a - 1$. The tight-binding model of Ref. [Goe+08] contains nearest-neighbor hopping amplitudes as well as next-nearest-neighbor hopping, and we take the magnitudes of the hopping amplitudes from Ref. [Goe+08]. Figure 2.4 shows the conductance g for strains $0 < |\epsilon| < 0.3$ and three representative angles φ. The strain is perpendicular to the **s** direction (as depicted in Fig. 2.4). The angle φ is defined as the angle between the transport direction and **s**. The tilt is of order $a/v \sim 0.06$ (v being the velocity in tilt direction) for the (already quite unrealistic) strain $\epsilon = 0.3$ [Goe+08]. As a consequence of this numerically small value of the tilt strength, the relative change in Fano factor remains small, $\lesssim 0.1\%$ for $\epsilon < 0.3$. While this variation is probably out of reach of experimental detection, it shows that Fano factor $F = 1/3$ is not strictly "universal" in graphene but can be changed by the breaking of symmetries.

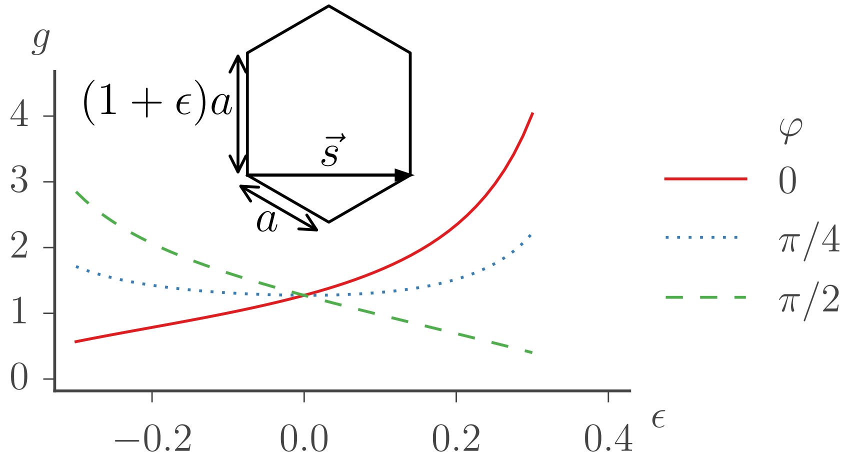

Figure 2.4.: Dimensionless conductance g of a strained graphene sheet as a function of the strain ϵ for different orientations φ (the angle between transport direction and **s**) and summed over both Dirac cones and spin. The inset shows a hexagon of the graphene lattice for $\epsilon = 0.2$.

2.4.2. Weyl semimetal

As an example in three dimensions we consider a tight-binding model of a spin-orbit coupled pyrochlore slab which hosts a Weyl semimetal phase with Weyl cones that may be significantly tilted[TB12; Ber+15]. In this case the lattice structure is layered, see Fig. 2.5, so that it is intrinsically anisotropic and no external strain needs to be applied in order to lift any symmetries forbidding a tilt of the Weyl cone. The model consists of a tight-binding Hamiltonian that contains spin-orbit coupling, in-plane and interplane nearest-neighbor hopping amplitudes, and in-plane next-nearest-neighbor hopping amplitudes. It was found to have a Weyl-semimetal phase for a certain range of parameter space, with a tilt of the Weyl cone that depends on the magnitude of the next-nearest-neighbor hopping amplitude t_2. There are six Weyl cones, located on the Γ–M lines[Ber+15] in the projected two-dimensional Brillouin zone of the slab geometry. The Weyl points are related to each other by the sixfold symmetry of the underlying lattice. We have numerically determined the position as well as tilt and anisotropy parameters as a function of the next-nearest-neighbor hopping t_2, keeping the other model parameters, defined in the lower right panel of Fig. 2.5, fixed $(t_1 = -1, t_\perp = 2, \lambda_1 = 0.3, \lambda_2 = 0.2)$, and calculated the dimensionless conductance g and the Fano factor F. The results are shown in Fig. 2.5 for an in-plane transport direction aligned with one of the crystal axes as indicated in the inset. The dependence on the orientation of the pyrochlore slab is very weak, less than 1% for both g and F, which can be understood as a consequence of there being six different contributing cones: when rotating the sample, some cones are rotated "away" from the transport direction, while others are rotated "towards" the transport direction. The changes in transport properties in different cones then have opposite signs (cf. Fig. 2.3), leading to a very weak angular dependence of g and F. The magnitude of the dimensionless conductance g and the Fano factor F can however differ substantially from the values calculated in the absence of a tilt.

2.5. Discussion

We have investigated the effect of anisotropies and tilts of Dirac and Weyl cones on quantum transport properties at the nodal point. Neither anisotropies nor tilts change the topology of the band structure and for this reason they are often neglected. We showed that a tilt nevertheless affects the dimensionless conductance g and Fano factor F. The latter observation is remarkable, since the Fano factor is often found to be a universal number, that does not depend on system-specific details.

Applying our results to the example of strained graphene, we found that the inclusion of a tilt of the Dirac cone leads to a sizable directional dependence of the conductance g. For realistic strains, the tilt effect on the Fano factor F is nonzero, though numerically very small — underlining the symmetry protected nature of "universal" quantum transport in two-dimensional Dirac materials. The consequences of a tilted dispersion, including a shift of the Fano factor F, may be more significant for other two-dimensional materials possessing more strongly tilted Dirac cones, such as the organic compound α–

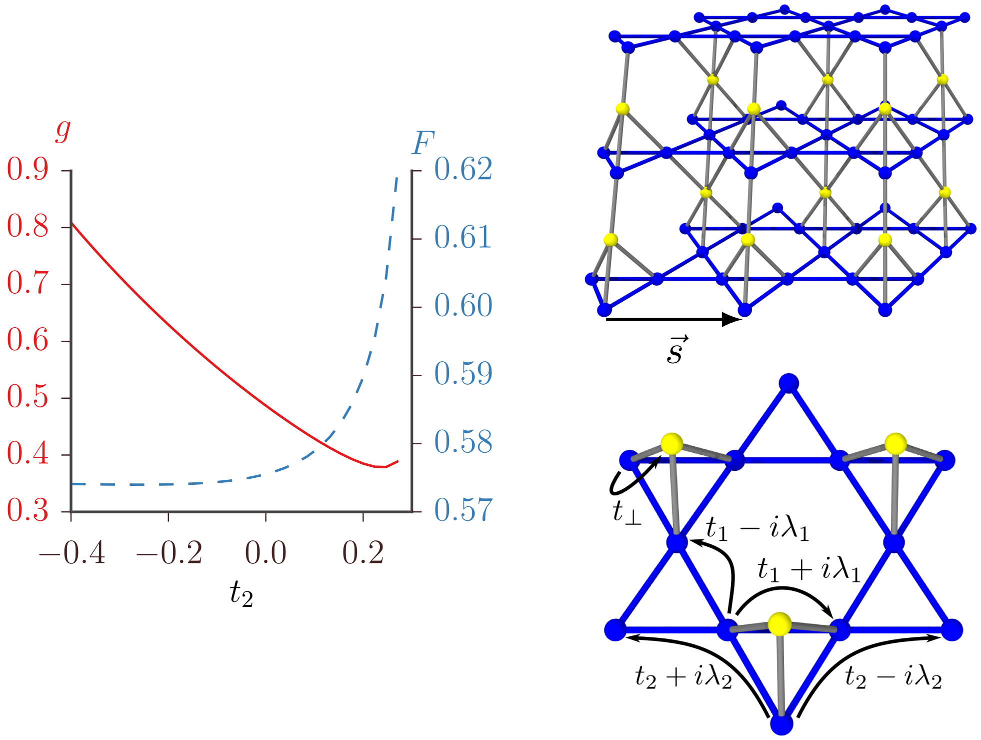

Figure 2.5.: Dimensionless conductance g (solid line) and Fano factor F (dashed line) for a pyrochlore slab as a function of the in-plane next-nearest-neighbor hopping amplitude t_2 (left panel). Transport direction is parallel to the crystal axis $\mathbf{s}$ (as shown in the upper right panel). Hopping parameters are indicated in the lower right panel.

(BEDT-TTF)$_2$I$_3$ [Goe+08; KKS06].

While the first observations of Weyl semimetals are a great experimental success, they all observed time-reversal symmetric Weyl semimetals[Xu+15; Lu+15; Lv+15; Hua+15; Zha+15]. These Weyl semimetals have additional states crossing the Fermi level opposed to the still hypothetical time-reversal symmetry breaking Weyl semimetals, which are predicted in the pyrochlore iridates[Wan+11], where the only states crossing the Fermi level are Weyl nodes, as is the case in our example of a pyrochlore slab. Hence the full transport properties could be obtained from the combined contribution of the Weyl nodes, whereas in the experimentally observed materials one should account also for the other states at the Fermi level.

In a recent work it was proposed that the Fano factor can be used as a universal quantity to discriminate different transport regimes in a disordered Weyl semimetal[Sbi+14]: In a calculation that did not include tilt or anisotropy, F was found to take the ballistic value (2.6) below a critical disorder strength, whereas F approaches the *smaller* diffusive value $F = 1/3$ at larger disorder. Our present results indicate that there is no universal value for the Fano factor in the ballistic limit. However, we also find that a tilt of the Weyl cone can only increase F, so that the Fano factor continues to be a powerful indicator discriminating the pseudoballistic and diffusive regimes.

For tilted and anisotropic cones the conductance varies strongly with transport direction and can be either higher or lower than the conductance of the symmetric cone. In contrast the Fano factor is only sensitive to the tilt of the cone and, whereas it still depends on the angle between tilt and transport direction, the Fano factor always increases for tilted cones. These insights should be useful for the experimental identification and characterization of a range of Weyl and Dirac materials by means of transport measurements.

3. Tilted disordered Weyl semimetals

In this chapter we investigate the combined effect of a tilted Weyl dispersion and the presence of potential disorder, generalizing the results of the previous chapter to disordered systems. In particular, we address the influence of a tilt on the disorder-induced phase transition between a quasi-ballistic phase at weak disorder, in which the disorder is an irrelevant perturbation, and a diffusive phase at strong disorder. This chapter is based on the publication [Tre+17b] and makes use of a variety of methods, namely the SCBA introduced in chapter 1.2.3 and transport numerics using the S-Matrix formalism as detailed in the chapters 1.1.5 and 1.6.2. While the SCBA is known to be only qualitatively correct in Weyl systems, as discussed in the introduction, the later work [SF17] performed a full renormalization group analysis of the same phase transition and confirmed all results we present in this chapter qualitatively and quantitatively found results differing by a consistent factor of ~ 2 from ours.

3.1. Introduction

The theory of Weyl semimetals was presented in depth in chapter 1.5. The conventional understanding of a Weyl semimetal is a system that, in the vicinity of the band touching points, is accurately described by the two-band Weyl Hamiltonian

$$H_0 = \hbar v \mathbf{k} \cdot \boldsymbol{\sigma}, \tag{3.1}$$

whose elegant form is dictated by Lorentz invariance and the requirement of a linear dispersion of the crossing bands. Here, momentum and energy are measured relative to the momentum and energy of the band crossing point, and $\boldsymbol{\sigma} = (\sigma_1, \sigma_2, \sigma_3)$ is the Pauli matrix. However, as was only appreciated recently, symmetry breaking terms such as an anisotropic velocity and a "tilt" of the Weyl dispersion (see Fig. 3.1) occur generically in Weyl materials and may have profound consequences for thermodynamic and transport properties[Ber+15; Tre+15; Sol+15; XCZ14; XZZ15; RKN15; Bee15; XD16; Den+16; Xu+16; Hua+16; Wan+16; Bel+16b; Koe+16]. Explicitly, a generic linear band crossing is described by

$$H_0 = \sum_{i,j=1}^{3} \hbar v_{ij} k_i \sigma_j + \sum_{i=1}^{3} v_{ii} a_i k_i \sigma_0 \ , \tag{3.2}$$

where the v_{ij} now describe an anisotropic velocity, the a_i represent a uniform linear tilting of both bands, and σ_0 is the 2×2 unit matrix. While the tilt looks most innocent—being proportional to the unit matrix σ_0 it does not alter the eigenstates of the model—it turns out to be the more interesting symmetry-breaking term. Whereas tilting terms have been considered early on in two-dimensional systems as consequences of perturbations[Kob+07; Goe+08], the topological stability of Weyl points[Wan+11], or, viewed alternatively, the generic nature of non-degenerate band crossings[Her37] in three dimensions allows for much stronger tilting. In fact, it was first shown in simple toy models[Ber+15], and later in more realistic materials simulations[Sol+15] and in models of superfluids[XZZ15], that the Weyl dispersion can easily be tilted over to the extent that a finite Fermi surface is formed, with hole and electron pockets touching at the Weyl point. These systems have been called "Type-II Weyl semimetals" and have, following their prediction in WTe_2, now been observed in a number of materials[Den+16; Xu+16; Hua+16; Wan+16; Bel+16b; Koe+16].

The effect of smaller, sub-critical tilts, which preserve the point-like nature of the Fermi surface, is more of a quantitative than of a qualitative nature, although even small tilts influence transport properties of Weyl semimetals in a unique way. When the Fermi level lies exactly at the nodal point, a Weyl semimetal of size L^3 has a vanishing conductivity σ, but a non-vanishing L-independent conductance $g = \sigma L$[Bai+14; Sbi+14]. The finite conductance is reminiscent of the universal minimal conductance $g = e^2/4\pi h$ predicted and observed in graphene[Two+06; Kat06], with the important distinction that in two dimensions a finite minimal conductance corresponds to a non-zero conductivity due to its different scaling with system size ($g = \sigma L^{d-2}$ in d dimensions). As shown in chapter 2 and in [Tre+15], the value of the minimal conductance g in a Weyl semimetal depends on the tilt. Moreover, tilt was also found to affect the value of the "Fano factor" $F = P/2eI$ at the Weyl point (the ratio of shot noise power P to current I [Tre+15]), which was otherwise found to be a universal number $F = (1 + 2\ln 2)/(6\ln 2)$[Bai+14; Sbi+14], independent of weak disorder, sample geometry, or anisotropy in the Weyl dispersion.

In this chapter we consider the combined effect of a (sub-critical) tilt of the Weyl dispersion and the presence of potential disorder, which is the second important addition to the Weyl Hamiltonian (3.1) required for the description of realistic condensed matter realizations of a Weyl semimetal. For isotropic Weyl cones the remarkable properties of the ideal system—in addition to the anomalous transport properties described above these include the vanishing density of states at the Weyl point—are known to persist up to a finite disorder strength, beyond which a diffusive phase with nonzero density of states at the Weyl point and nonzero conductivity sets in[Fra86; Sbi+14; SDB16; Kob+14; SRG15; SBB15; PGS15; LCF16; RJS16; SR17]. The Fano factor F takes a different, but again universal value $F = 1/3$ in the diffusive phase.

Our main finding, which we support with a combination of analytical and numerical arguments, is that the main effect of tilting the Weyl dispersion is to reduce the critical disorder strength K_c for the transition between the "pseudo-ballistic" weak-disorder phase and the diffusive strong-disorder phase. Such a result can be expected intuitively, based on the consideration that in the weak-disorder phase there is a vanishing density of states at the Weyl point, and disorder acts by virtual excitations to states of higher energy, where the range of reachable energies is determined by the disorder strength[SRG15; SR17]. Tilting the Weyl dispersion lowers the energy of some states

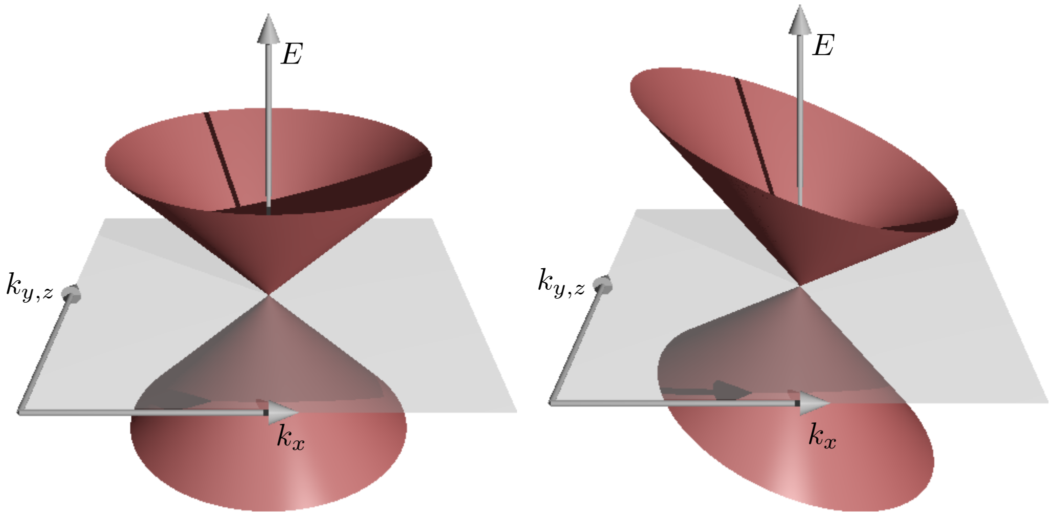

Figure 3.1.: Illustration of a tilted Weyl dispersion, projected to two momentum dimensions. The left panel shows the isotropic case ($a = 0$); the right panel shows a dispersion tilted in the negative x direction with tilt parameter $a = 0.4$.

while raising the energy of others. The net effect, however, is that there are more states available in a given energy range than in the isotropic cone, see Fig. 3.1. Explicitly, the density of states $\nu(\varepsilon)$ depends on the tilt parameter a as

$$\nu(\varepsilon) = \frac{\nu_0(\varepsilon)}{(1-a^2)^2} \geq \nu_0(\varepsilon), \tag{3.3}$$

where $\nu_0(\varepsilon)$ is the density of states without tilt. This implies that the disorder of the same strength K can be expected to have a stronger influence on a tilted Weyl dispersion, and it is natural to expect a lower critical disorder strength K_c for cones with larger tilt.

Upon approaching the critical tilt $a = 1$ the critical disorder strength K_c goes to zero—again, not a surprise given the diverging density of states for $a \to 1$. This implies, however, that in the presence of disorder the tilt-driven transition between type-I and type-II Weyl semimetals will be preceded (and, hence, masked) by the tilt-driven transition from the pseudo-ballistic weak-disorder phase into the diffusive strong-disorder phase.

The remainder of this chapter is organized as follows: In Sec. 3.2 we introduce to the specific model employed throughout this chapter, which contains a tilted dispersion as well as a random potential. In Sec. 3.3 we employ the self-consistent Born approximation to show how a tilted dispersion affects the disorder-induced phase transition. We then corroborate these results by two distinct numerical approaches: We use the kernel polynomial method[Wei+06] to compute the density of states in a tight-binding model using the same disorder type as in the SCBA, see Sec. 3.4, and we study transport properties in finite size systems using a scattering matrix approach, see Sec. 3.5. The use of numerical methods to confirm our conclusions is necessary, since the self-consistent Born approximation is known to be an uncontrolled approximation for the disorder-induced phase transition in Weyl semimetals[Sbi+14]. We conclude in Sec. 3.6.

3.2. Model

We consider a single disordered Weyl node described by the Hamiltonian

$$H = H_0 + U, \quad H_0 = v(\mathbf{k} \cdot \boldsymbol{\sigma} + a k_z \sigma_0), \tag{3.4}$$

where without loss of generality we have chosen the tilt to be in the z direction. Momentum and energy are measured with respect to the Weyl node. We have chosen units such that $\hbar = 1$. The critical tilt is $a = 1$, and we will consider sub-critical tilts $0 \leq a < 1$ only.

The disorder potential U is taken to be a Gaussian random potential with zero average and with two-point correlation function

$$\langle U(\mathbf{q}) U(\mathbf{q}') \rangle = \frac{K \xi h^2 v^2}{L^3} e^{-\frac{q^2 \xi^2}{2}} \delta_{\mathbf{q},\mathbf{q}'} \tag{3.5}$$

for a finite system of size L^3. Here ξ is the correlation length of the disorder potential and K is the dimensionless disorder strength. The restriction to a single Weyl node requires that the correlation length ξ is much larger than the inverse distance between the Weyl nodes.

We have chosen not to include anisotropy of the Weyl dispersion in to the Hamiltonian (3.4) [compare with Eq. (3.2)]. Although anisotropies are as ubiquitous in real materials as the tilts, they can largely be understood by simple means of rescaling of the coordinate axes, rendering the Weyl dispersion isotropic but the disorder anisotropic[Tre+15; RKN15]. Through such a rescaling procedure, anisotropies were found to affect the conductance g (since g depends on sample geometry), but not the Fano factor F. Tilts, on the other hand, cannot be removed by the rescaling procedure, and were found to affect both g and F in the absence of disorder[Tre+15].

In the following three Sections we calculate the critical disorder strength K_{c} for the disorder-induced transition to a diffusive phase using three different methods. Section 3.3 employs the self-consistent Born approximation and addresses the density of states, using the model described above. Section 3.4 uses the kernel-polynomial method to calculate the density of states for a tight-binding model for which the continuum model (3.4) is the low-energy limit. Section 3.5 considers transport properties of the continuum model (3.4), but for a system of size $W^2 \times L$, where the sample width W (transverse to the transport direction) is chosen much larger than its length L (in the transport direction) to ensure that the transport properties do not depend on the choice of the boundary conditions in the direction transverse to the current flow.

3.3. Density of states from SCBA

To study the density of states of the model (3.4) we employ the self-consistent Born approximation (SCBA). We closely follow a similar calculation of Ominato and Koshino for a Weyl dispersion without tilt[OK14].

Before we turn to a description of our calculations, we note that the SCBA relies on a diagrammatic expansion that is known to neglect important contributions. For a Weyl dispersion without tilt, the SCBA is known to yield critical disorder strengths K_c, which are larger by a factor ~ 2 than the ones obtained by more precise numerical simulations[Sbi+14]. We nevertheless see the SCBA as a useful approximation for a qualitative understanding of the way in which a tilted Weyl dispersion affects the critical disorder strength. Furthermore, the SCBA allows us to access the disorder-induced renormalizations of tilt and Fermi velocity.

The disorder-averaged density of states $\nu(\varepsilon)$ is expressed in terms of the (2×2 matrix) Green function as

$$\nu(\varepsilon) = -\frac{1}{\pi L^3} \mathrm{Im} \sum_{\mathbf{k}} \mathrm{Tr} \left\langle G(\mathbf{k}, \varepsilon + i0^+) \right\rangle , \tag{3.6}$$

where the brackets $\langle \ldots \rangle$ indicate the disorder average. In the SCBA the disorder-averaged Green function is expressed as

$$\langle G(\mathbf{k}, \varepsilon) \rangle = \frac{1}{(\varepsilon - vak_z)\sigma_0 - v\mathbf{k} \cdot \sigma - \Sigma(\mathbf{k}, \varepsilon)}, \tag{3.7}$$

with the SCBA approximation for the self-energy

$$\Sigma(\mathbf{k}, \varepsilon) = \sum_{\mathbf{k}'} G(\mathbf{k}', \varepsilon) \langle |U(\mathbf{k} - \mathbf{k}')|^2 \rangle, \tag{3.8}$$

where the disorder average $\langle |U(\mathbf{q})|^2 \rangle$ is given by (3.5). The self-consistent integral equations (3.7) and (3.8) are solved numerically. Details on the numerical procedure are given in appendix B. The critical disorder strength K_c is found as that disorder strength for which the density of states $\nu(0)$ at the Weyl point becomes finite, whereas $\nu(0) = 0$ for $K < K_\mathrm{c}$. Our main results are summarized in Fig. 3.2.

The SCBA phase diagram of Fig. 3.2 confirms the intuitive picture of the introduction: the critical disorder strength decreases with increasing tilt and approaches 0 when the tilt strength a approaches the critical value $a = 1$. This is consistent, since as a finite density of states develops when the cone tips over ($a \geq 1$), we expect a diffusive phase at arbitrarily small disorder strengths for super-critical tilt.

The SCBA not only allows us to find the tilt-dependence of the critical disorder strength K_c, the expansion of the self-energy $\Sigma(\mathbf{k}, 0)$ for small momenta at zero energy also allows us to find a disorder-renormalized Fermi velocity $\tilde{v}$ and tilt $\tilde{a}$. Taking into account rotation invariance around the z axis, the small-$\mathbf{k}$ expansion of the self-energy reads

$$\Sigma(\mathbf{k}, 0) = v(\alpha \mathbf{k} \cdot \sigma + \beta a k_z \sigma_0) + \mathcal{O}(k^2), \tag{3.9}$$

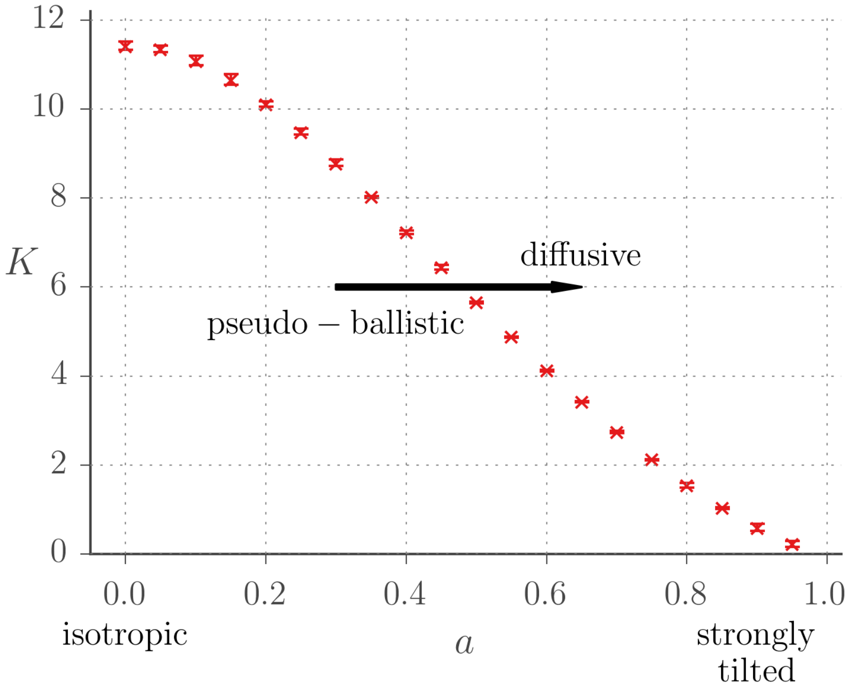

Figure 3.2.: Phase diagram for the tilted Weyl cone obtained from the SCBA. The numerical uncertainty for K_c is shown as errorbars (see appendix for a discussion).

from which we obtain

$$\tilde{v} = v(1+\alpha), \quad \tilde{a} = a\frac{1+\beta}{1+\alpha}. \tag{3.10}$$

Our result for the renormalized Fermi energy $\tilde{v}$ is consistent with that of Ref. [OK14] and will not be discussed further here. The renormalized dimensionless tilt $\tilde{a}$ is shown in Fig. 3.3, as a function of disorder strength K. Figure 3.3 suggests that there is not only the single fixed point of the clean and isotropic Weyl cone (in the renormalization-group sense), but rather a continuous family of fixed points at no disorder which are distinguished by their tilt. Also note that while disorder $K < K_\mathrm{c}$ leads to an increased dimensionless tilt, in the SCBA approximation sub-critical disorder cannot lead to an "over-tilting" of the Weyl dispersion. In other words, the disorder-induced phase transition to a diffusive phase with a finite density of states at the Fermi level always takes place *before* the tilt-induced transition to a type-II Weyl semimetal, which also has a finite density of states at the nodal point. (This is consistent with the tilt-dependence of the critical disorder strength shown in Fig. 3.2, which shows that the critical disorder strength approaches zero in the limit $a \to 1$.) This observation remains valid if the disorder-induced renormalization of the tilt is included, see Fig. 3.3.

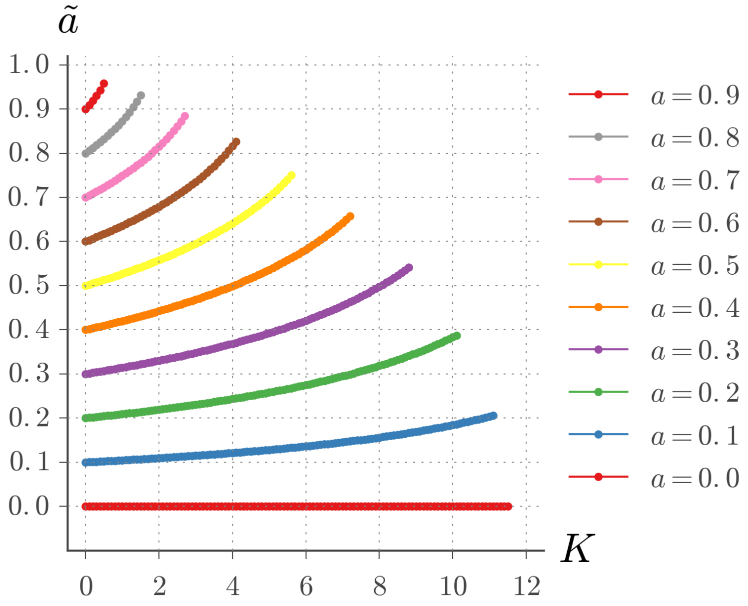

Figure 3.3.: Effective SCBA tilt $\tilde{a}$ vs. dimensionless disorder strength K in the weak-disorder phase $K < K_c$.

3.4. Density of states from KPM

To complement the SCBA analysis we now report a numerical calculation of the density of states, using the kernel polynomial method (KPM)[Wei+06]. The KPM is a numerically efficient method to approximate the density of states of large lattice Hamiltonians H represented as sparse matrices. As a first step, the Hamiltonian is rescaled so that the spectrum fits in the interval $[-1, 1]$. The density of states is then expanded in Chebyshev polynomials. The expansion coefficients (up to a certain order, usually a few thousand) can be expressed as a trace over a polynomial of H which can be well approximated numerically by using a few random states. Employing identities for Chebyshev polynomials, the expansion coefficients can be efficiently calculated by iteration involving only matrix-vector products. Finally, residual Gibbs oscillations in the density of states are suppressed using an appropriate smoothing Kernel.

We consider the two-band lattice model[TV13]

$$\begin{aligned} H_0\left(\mathbf{k}\right) =& \frac{v}{b}\left[\sigma_x \sin bk_x + \sigma_y \sin bk_y \right.\\ & \left. -\sigma_z \cos bk_z - \sigma_0 a \cos bk_z\right] \end{aligned} \tag{3.11}$$

where b is the lattice constant. The model (3.11) features eight Weyl points at momenta $\mathbf{k}(\tau_x, \tau_y, \tau_z) = (k_x(\tau_x), k_y(\tau_y), k_z(\tau_z))$ for $\tau_{x,y,z} = \pm 1$ with $k_x(\tau_x) = (\pi/2b)(1-\tau_x)$, $k_y(\tau_y) = (\pi/2b)(1-\tau_y)$, $k_z(\tau_z) = \tau_z \pi/2b$. We add a disorder potential as in Eq. (3.5), with correlation length $\xi = 5b$, which ensures that (i) the smooth disorder correlations are well represented on the discrete lattice and (ii) the inter-node scattering rate is suppressed as compared to the intra-node rate by a factor of order $\exp[-\pi^2\xi^2/2b^2] < 10^{-19}$, such that the physics can be regarded as effectively single-node.

In Fig. 3.4, top panel, we show the KPM results for the density of states $\nu(\varepsilon) = 0$ without tilt (left panel, solid curves) and with dimensionless tilt $a = 0.5$ (right). We also show the predictions of the SCBA (dashed curves). For weak disorder and away from zero energy, the KPM and SCBA results are in good agreement, but the comparison with the numerical results also shows that the SCBA overestimates the critical disorder strength K_c above which the zero-energy density of states becomes finite. The figure suggests, however, that this overestimation happens equally for zero tilt and for finite tilt, so that the trend predicted by the SCBA is indeed confirmed by the KPM.

The bottom panel of Fig. 3.4 shows the density of states $\nu(0)$ at the nodal point as a function of the disorder strength for different values of the tilt parameter. Again, these results confirm the trend predicted by the SCBA, that larger tilt corresponds to a lower critical disorder strength. However, a precise determination of K_c is beyond the capabilities of the KPM method[SBB15].

3.5. Quantum transport

The disorder-induced phase transition is not only characterized by its effect on the density of states at the nodal point $\nu(\varepsilon)$, which is zero for $K < K_\mathrm{c}$ and finite for $K > K_\mathrm{c}$, the transition also strongly affects transport properties, such as the conductance or shot noise power. In this Section we show that the characteristic transport properties at the nodal point found for a Weyl dispersion without tilt persist for a tilted dispersion, and we provide more evidence in support of the result of the previous Sections, that the critical disorder strength is reduced in the presence of a tilted Weyl dispersion.

We calculate the transmission matrix t of a finite sample of length L in the transport direction (which we take to be the x-direction) and width W in the transversal (y and z) directions. The method is explained in detail in Ref. [Sbi+14]. With a width W the two-point correlation function (3.5) of the disorder potential is replaced by

$$\langle U(\mathbf{q})U(\mathbf{q}')\rangle = \frac{K\xi h^2 v^2}{W^2 L} e^{-\frac{q^2\xi^2}{2}} \delta_{\mathbf{q},\mathbf{q}'}. \tag{3.12}$$

The conductance G per Weyl node and the Fano factor F are expressed in terms of t as

$$G = \frac{e^2}{h} \operatorname{Tr} tt^\dagger, \tag{3.13}$$

$$F = 1 - \frac{\operatorname{Tr}(tt^\dagger)^2}{\operatorname{Tr} tt^\dagger}, \tag{3.14}$$

where the trace is taken with respect to the transverse momenta. To approach bulk results as closely as possible, we choose the sample width $W \gg L$ and verify that

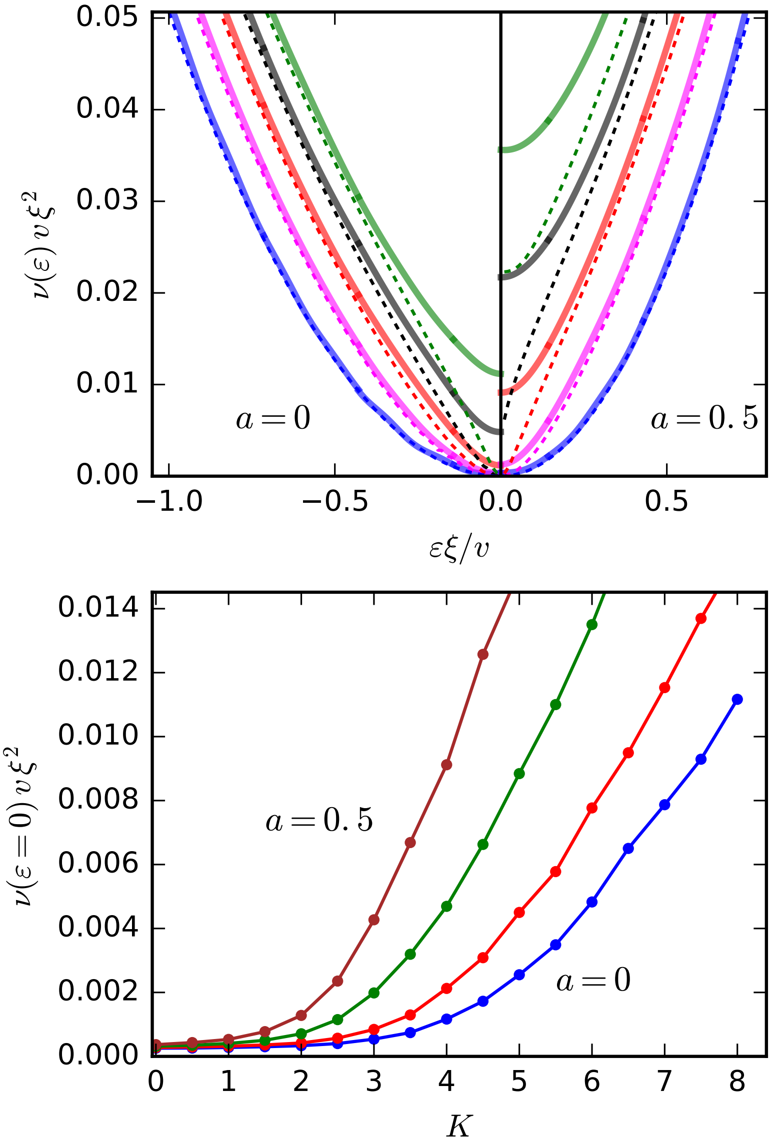

Figure 3.4.: Top: Density of states $\nu(\varepsilon)$ as a function of energy ε without tilt (left, $a = 0$) and with tilt (right, $a = 0.5$), as calculated by the kernel polynomial method for disorder strengths $K = 0, 2, 4, 6, 8$ (bottom to top). The dashed lines denote the SCBA results, Eq. (3.6). [For $K = 0$, the SCBA coincides with the zero-disorder density of states of Eq. (3.3).] Bottom: Density of states $\nu(0)$ at the nodal point versus disorder strength for different values of the tilt, $a = 0$, 0.25, 0.4, 0.5 (right to left). The calculations were carried out for an average over 20 realizations of the random potential, for a cubic lattice of size $L/b = 200$, with 30 random vectors for calculating the trace in the KPM and an expansion order of roughly 1000. The density of states is normalized to a single Weyl node.

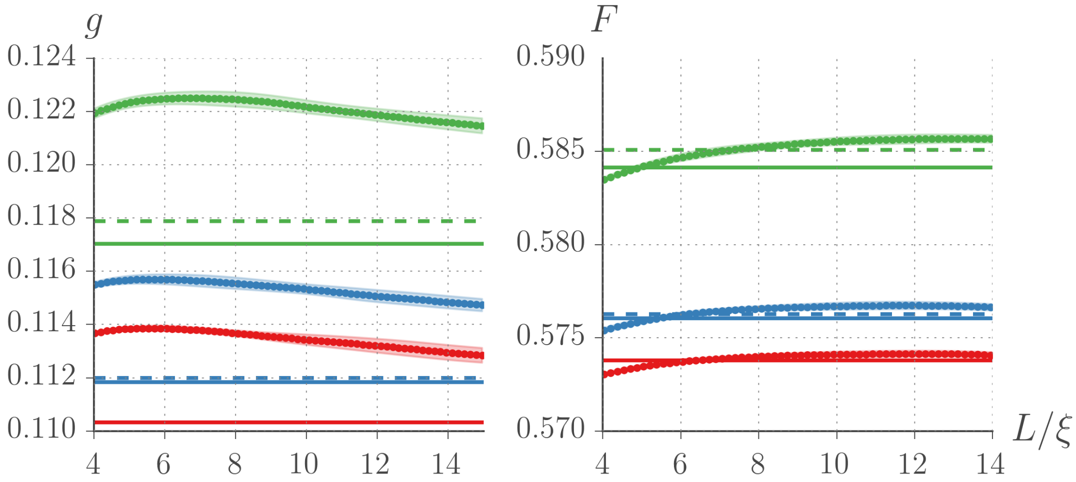

Figure 3.5.: Dimensionless conductance g, rescaled for a system of size L^3 and Fano factor F for sub-critical disorder strength $K = 1$ and for tilt parameter $a = 0$, 0.25, and 0.5 (bottom to top). The data points show results from numerical calculations, as described in the text. The solid and dashed line indicate the values expected without disorder and for a clean system with disorder-renormalized tilt $\tilde{a}$, respectively. We have not shown data for $L < 4$, which are dominated by finite-size effects. The numerical curves are based on an average over at least 10 disorder realizations. The error bars show the residual statistical error.

the conductance is proportional to W^2 and is independent of the boundary conditions chosen in the transverse direction. We present results for the dimensionless conductance rescaled for a cubic sample of size L^3, $G = (e^2/h)(W^2/L^2)g$. The conductivity σ is calculated from the standard relation $\sigma = (e^2/h)g/L$. The conductance g and Fano factor F without disorder, but with a tilted dispersion, were calculated in chapter 2 which is based on Ref. [Tre+15].

Figure 3.5 shows the dimensionless conductance g and the Fano factor versus system size L for disorder strength $K = 1$ and for the tilt parameter $a = 0$, 0.25, and 0.5. The disorder strength $K = 1$ is sub-critical for all three values of a considered. The figure also shows the conductance and Fano factor expected for a clean Weyl semimetal and for a clean Weyl semimetal with SCBA-renormalized tilt $\tilde{a}$. Especially the conductance data still show a considerable size dependence, even for the largest system sizes we could reach. Nevertheless, the data leave no doubt that the conductance remains bounded as a function of L, indicating that the conductivity $\sigma = (e^2/h)g/L$ is zero in the thermodynamic limit, which implies that the transport characteristics of the quasi-ballistic weak-disorder phase persist in the presence of a tilted Weyl dispersion. Moreover, the finite-size data also show that the conductance increases with increasing tilt, consistent with the analysis of the clean limit in Ref. [Tre+15] and with the expectation that tilt drives the system closer to the disorder-induced phase transition. However, the finite-size effects are too large to permit a more quantitative analysis. In particular, the finite-size effects are too large to quantitatively confirm or disprove the SCBA expectation for the conductance.

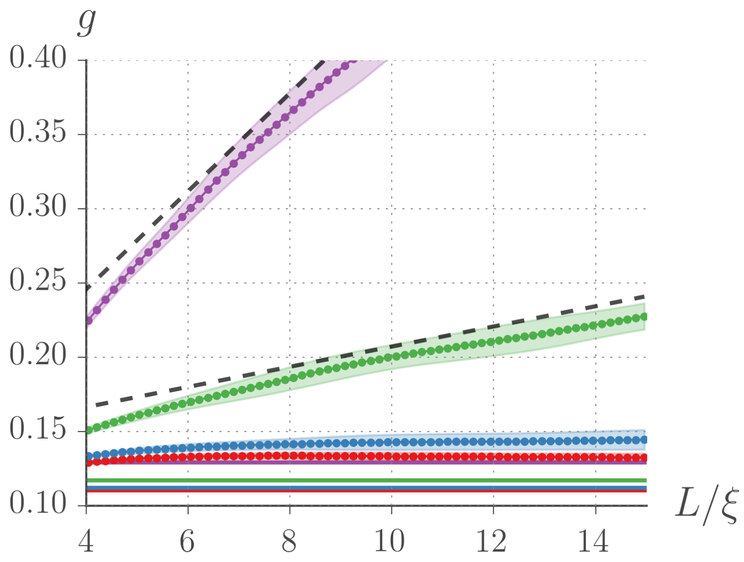

Figure 3.6.: Dimensionless conductance g as a function of system size L for disorder strength $K = 4$ and tilt parameters $a = 0$, 0.25, 0.5, and 0.75 (bottom to top). The data points show results from numerical calculations after averaging over at least 10 disorder realizations. The error bars show the residual statistical error. We have not shown data for $L < 4$, which are dominated by finite-size effects. The conductance is bounded for $a = 0$ and $a = 0.25$ (bottom two data sets), which is characteristic of the quasi-ballistic weak-disorder phase. For $a = 0.5$ and $a = 0.75$ the conductance is proportional to the system size L for large L (top two data sets), characteristic of the diffusive strong-disorder phase. The dashed lines indicate a linear increase with L and are shown as a guide to the eye.

Figure 3.6 shows the dimensionless conductance g versus system size for disorder strength $K = 4$, chosen such that the disorder is sub-critical without tilt, but above critical with large tilt. The progression of the curves shown in the figure corresponds to the horizontal arrow in Fig. 3.2 (although the value of the disorder strength K is less than in Fig. 3.2, reflecting the overestimation of the critical disorder strength in the SCBA). As in the previous figure, finite-size effects are considerable, nevertheless the asymptotic dependences characteristic of the weak-disorder phase (g vs. L bounded) and of the strong-disorder phase ($g \propto L$ for large L) are clearly visible for small and large tilt, respectively. Figure 3.6 thus illustrates how variation of the tilt can be used to scan through the disorder-induced phase transition between the quasi-ballistic weak-disorder phase and the diffusive strong-disorder phase. The Fano factor F of the finite samples is subject to large fluctuations near the critical disorder strength and data is not shown.

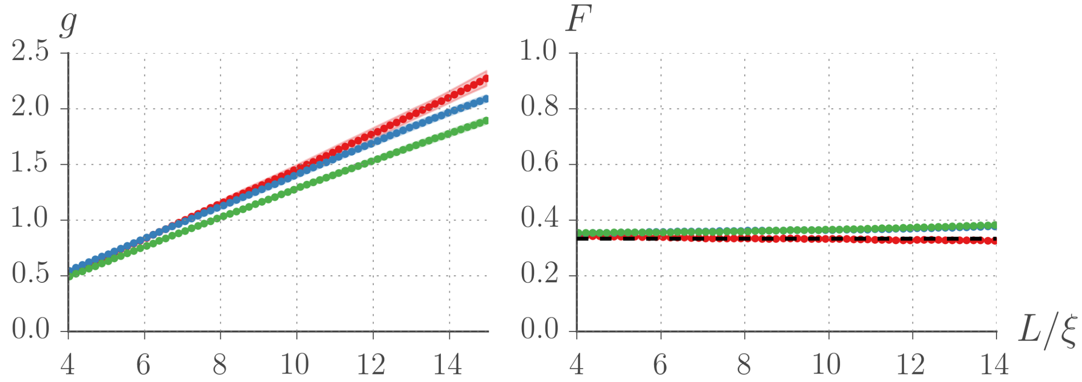

Figure 3.7.: Dimensionless conductance g and Fano factor F as a function of system size L for disorder strength $K = 30$ and tilt parameters $a = 0$, 0.25, and 0.5 (red, blue, green, i.e. top to bottom in the left panel). The data points show results from numerical calculations after averaging over at least 10 disorder realizations. The error bars show the residual statistical error. Data for $L < 4$ are dominated by finite-size effects and are not shown. The dashed black line in the right panel indicates the Fano factor $F = 1/3$ expected in the diffusive regime.

The case of very strong disorder is shown in Fig. 3.7, which shows conductance and Fano factor for $K = 30$, which is well above the critical value regardless of the tilt a. For all values of the tilt the conductance increases linearly with L, consistent with a finite conductivity $\sigma = (e^2/h)g/L$ in the thermodynamic limit. Up to small deviations (which we cannot explain, but which are ubiquitous in transport calculations) the Fano factor is at the value $F = 1/3$ appropriate for the diffusive phase. In any case, our numerical calculations show that both conductance and Fano factor can be used to distinguish the weak-disorder and strong-disorder phases. In fact, in the presence of tilt the difference between the Fano factor for the weak-disorder and strong-disorder phases is even larger than without tilt, see Fig. 3.5.

3.6. Discussion

In this chapter we have studied how the combination of potential disorder and a tilted Weyl dispersion affects the zero-energy density of states and transport properties of a Weyl semimetal. Our main conclusions, supported via calculations of the density of states using the self-consistent Born approximation (SCBA), calculations of the density of states for a tight-binding model using the kernel polynomial method (KPM), and calculations of the conductance and Fano factor using the scattering approach, are that (1) the existence of a disorder-induced phase transition between a quasi-ballistic weak-disorder phase with zero density of states and finite conductance at the nodal point and a diffusive strong-disorder phase characterized by a finite conductivity and a finite density of states at the nodal point is unaffected by the presence of a tilt of the Weyl dispersion, and (2) the critical disorder strength for the transition decreases upon increasing the tilt. Importantly, the critical disorder strength approaches zero as the tilt approaches the critical tilt, so that in the presence of disorder the tilt-induced phase transition from a “type-I” Weyl semimetal (with a point-like Fermi surface) to a “type-II” Weyl semimetal (with finite particle and hole pockets at the nodal point) is always preceded by a disorder-induced transition to a diffusive phase with a finite density of states at the nodal point.

Another conclusion of our findings is that there is a family of weak-disorder pseudoballistic fixed points, all of them being effectively disorder-free, but distinguished by their effective tilt. The value of the tilt—*i.e.* which fixed point one is in—can be deduced from the Fano factor, which is a nontrivial function of the tilt parameter a [Tre+15]. (In principle, the dimensionless conductance g also depends on the tilt but, unlike the Fano factor, g also depends on a possible anisotropy of the Weyl dispersion, which the Fano factor F does not.)

In principle tilted spectra can also occur in two-dimensional systems with a Dirac dispersion, such as graphene. In that context one expects that tilt, too, will quantitatively influence transport properties and the density of states. However, in two dimensions there is no disorder-induced phase transition between a quasi-ballistic and a diffusive regime, and the effect of tilt will be mainly quantitative, and not qualitative. Moreover, in graphene, certainly the two-dimensional Dirac material studied the most, the Dirac points are at high symmetry points in the Brillouin Zone, at which anisotropies and tilts are prohibited by crystalline symmetries.

While our findings suggest that the tilt-induced transition between type-I and type-II Weyl semimetals may be obscured by the presence of disorder, they also suggest that tilt can be used as a parameter that drives the system through the disorder-induced transition between quasi-ballistic and diffusive phases. In general strain or pressure induces a change of the lattice geometry, which in turn influences the tilt. While the magnitude of the tilt is directly influenced by the hopping parameters of a lattice model[Tre+15], the experimental feasibility depends on the specific material and the corresponding tilt’s susceptibility to strain or pressure. Such limitations may make it necessary to start the tilt-induced phase transition already at a close-to-critical disorder strength, so that only a relatively minor change in the band structure is enough to drive the system through the quasi-ballistic-to-diffusive phase transition. (We note that pressure or strain may also result in a change of Fermi velocity, which would also influence K_c, and may be an additional factor that helps/obstructs the observation of the phase transition.)

4. Charge density wave instabilities of type-II Weyl semimetals in a strong magnetic field

The transport phenomena studied in the previous chapters were essentially single particle phenomena. On single particle phenomena in Weyl semimetals exists a large body of literature, but whether interesting many-body effects due to interactions arise in Weyl systems remains much less explored. In this chapter, based on the publication [Tre+17a], we investigate the effect of interactions in a microscopic model of a type-II Weyl semimetal in a strong magnetic field, motivated by the observation of very large and surprisingly robust magnetoresistance in several type-II Weyl semimetals. We will identify a charge density wave (CDW) instability even for weak interactions stemming from the emergent nesting properties of the type-II Weyl Landau level dispersion and observe a cascade of CDW transitions in decreasing temperature. The implications of these results on magnetotransport properties are discussed in chapter 5.

4.1. Introduction

The theory of Weyl fermions in condensed matter systems is presented in detail in chapter 1.5. Much recent attention has focused on type-II Weyl semimetals[Sol+15] whose linear dispersion is so strongly tilted[Ber+15; XZZ15; Goe+08; Tre+15] that it forms electron and hole pockets. Several materials in this class, including WTe_2 [Ali+14], WP_2 [Aut+16; Kum+17] and $\mathrm{Mo}_x\mathrm{W}_{1-x}\mathrm{Te}_2$ [Bel+16a], have in parallel attracted ample attention due to their remarkable magnetotransport properties. While a single particle analysis reveals a novel twist on the chiral anomaly in type-II Weyl semimetals[UB16; TCG17; YYY16], there is no commonly accepted explanation of the observed magnetotransport properties nor an understanding of whether they are at all rooted in the topological properties of these materials, highlighting the need for an understanding of many-body effects.

Exotic interaction effects in Weyl semimetals[Men+16; Ber+15], some taking place only in systems with tilted Weyl cones[Ber+15], have recently been explored. More conventional phenomena such as density wave instabilities have so-far only been discussed in type-I Weyl semimetals where, however, they require a significant critical interaction strength at zero magnetic field[WCA12; WZ13; Lau+16; RGJ17], consider the chemical potential away from the Weyl node[WY16] or only appear in a magnetic field as effective one-dimensional instabilities of the chiral mode[YLR11; RS15b; ZS17]. Further spin ordering in Weyl semimetals has been studied[SZW15]. A Weyl semimetal in a strong magnetic field was experimentally studied in [Mol+16], where the connection of Fermi arc surface states to chiral bulk modes was observed.

In this chapter we show that the electron- and hole-like pockets of the overtilted cones in type-II Weyl semimetals generically render these systems much more susceptible to interaction effects. In particular we show that in a magnetic field the Landau level dispersion acquires nesting-like features between a large number of Landau level bands which triggers a CDW transition for small interactions. As this emergent weak coupling instability in a magnetic field neither requires perfect particle-hole compensation nor nesting of the zero field band structure we argue that CDW phases are a common property of the high field regime of type-II Weyl semimetals.

Our starting point is a simple microscopic Hamiltonian $H = H_0 + H_{\text{int}}$ with a quadratic lattice model H_0 featuring Weyl nodes and a local density-density interaction H_{int}. We show that in a field a weak coupling intra-cone CDW instability with a wavevector related to the electron and hole pocket separation appears. Our qualitative discussion is corroborated by a microscopic calculation for which we derive a continuum description. Going beyond lowest order in the momenta is necessary to describe closed electron and hole pockets. We note that this is in general crucial for a correct low energy description in type-II Weyl systems.

This chapter is structured as follows: First we introduce a simple microscopic model of a type-II Weyl semimetal. Calculating the dispersion of Landau levels in a magnetic field both in the lattice and in the corresponding continuum description, we give an intuitive argument for a CDW instability based on emergent nesting features. Second, we develop the mean-field theory for generic interactions in a type-II Weyl cone in a magnetic field. Third, we present self-consistent CDW solutions as a function of temperature and magnetic field. Finally, we discuss implications for experiments.

4.2. The model

We first concentrate on the non-interacting bandstructure governed by

$$\begin{aligned} H_0(\mathbf{k}) = &\left(M - \cos k_x - \cos k_y\right)\sigma^x + \sin k_y \sigma^y \\ &+ \sin k_z \sigma^z + \left(t_1 \sin k_z + t_2 \sin 2k_z\right)\sigma^0 \end{aligned} \tag{4.1}$$

in which the tilt of the Weyl cones can be easily tuned to feature electron and hole pockets, e.g. at $M = 1$, $t_1 + 2t_2 > 1$ this model has type-II Weyl nodes at $\mathbf{k}_W = (\pm\pi/2, 0, 0)$. Since we are interested in intra-cone instabilities we can expand around one of the cones yielding a low energy continuum description

$$\begin{aligned} H_0^{\text{e}ff}(\mathbf{k}) = &\pm k_x \sigma^x + k_y \sigma^y + (k_z - \frac{1}{6}k_z^3)\sigma^z \\ &+ \left((t_1 + 2t_2)k_z - \frac{1}{6}(t_1 + 8t_2)k_z^3\right)\sigma^0. \end{aligned} \tag{4.2}$$

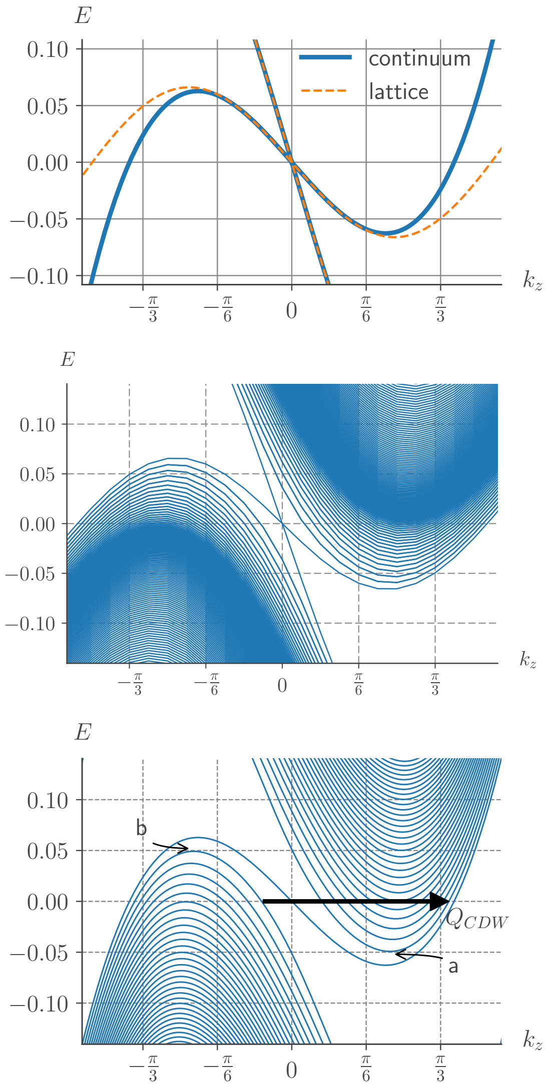

Figure 4.1.: Comparison of the dispersion of the lattice model and the continuum theory without magnetic field (top panel). The dispersion of the lattice model in a magnetic field is shown in the middle panel (with two Weyl cones at different k_x superposed) and the corresponding dispersion of the continuum theory (single cone) in the bottom panel. The parameters of the lattice model are $t_1 = -0.8, t_2 = -0.6, a_0 = 7\text{Å}$ and the parameters of the low energy theory are chosen to match the third order expansion of the lattice model. The magnetic field strength for the bottom row is $B = 86\,T$.

The momenta k_i ($i = x, y, z$) are in the range $-\pi < k_i \leq \pi$ and measured in $1/a_0$, where a_0 is the lattice spacing. We have omitted an overall prefactor $\hbar v$ which sets the energy scale in terms of Fermi velocity v. Importantly, we have expanded up to $\mathcal{O}(k_x^2, k_y^2, k_z^5)$

and included the next to leading order term in k_z. We are not aware that this has been done before but it is crucial for a correct low energy description with closed electron and hole pockets.

Throughout this manuscript we assume the realistic but exemplary values of $\hbar v =$ 1eV Å and $a_0 = 7$Å. The term proportional to t_2 is included to get smoother electron and hole pockets (see Figure 4.1) and to elucidate how longer range hopping terms can be included in the low order expansion. Our effective model inherits the perfect compensation between electron and hole pockets present in our tight binding model and which is also a prominent feature of WTe$_2$. However, as discussed below such perfect compensation is not a crucial ingredient of our CDW mechanism.

It is worth mentioning that there are also type-I nodes at $\mathbf{k} = (\pm\pi/2, 0, \pi)$ in this lattice model. However, these are unimportant for our considerations and could easily be removed at the price of a having a more complex lattice model.

We concentrate on magnetic fields along the $\mathbf{z}$ tilt direction of the cones leading to flat Landau levels in the k_x, k_y-plane dispersing only along the k_z direction. Then we can introduce the field via the usual vector potential $\mathbf{A}$ minimally coupled to the crystal momentum $\mathbf{\Pi} = \hbar\mathbf{k} - \frac{e}{c}\mathbf{A}$ and work with the usual ladder operators in the Landau level (LL) basis, see appendix C.2 for details of the mean field calculation, such that the spectrum is given by the eigenvalues of

$$\hat{H}_0^{\text{eff}} =(-\eta k_z + \gamma k_z^3)\sigma_0 + (k_z + \beta k_z^3)\sigma_z + \frac{\sqrt{2n}}{l_B}\sigma_x \tag{4.3}$$

with the Landau level index $n > 0$ and the magnetic length $l_B = \sqrt{\frac{\hbar}{eB}}$. The parameters $\eta = -(t_1 + 2t_2), \beta = -\frac{1}{6}, \gamma = -\frac{1}{6}(t_1 + 8t_2)$ are directly related to our lattice model, with $t_1 = -0.8, t_2 = -0.6$ for concreteness throughout this paper.

Furthermore, we obtain the transformation relating our original sublattice creation operators $c_{A/B,n,p,k_z}$, with p labeling the degenerate states within each LL, to new operators $a/b_{n,p,k_z}$ for to the electron and hole like bands

$$\begin{pmatrix} a_{n,p,k_z} \\ b_{n,p,k_z} \end{pmatrix} = \underbrace{\begin{pmatrix} u(k_z,n,B) & v(k_z,n,B) \\ -v(k_z,n,B) & u(k_z,n,B) \end{pmatrix}}_{\hat{U}(k_z,n,B)} \begin{pmatrix} c_{A,n,p,k_z} \\ c_{B,n,p,k_z} \end{pmatrix} \tag{4.4}$$

with $u(k_z,n,B)^2 + v(k_z,n,B)^2 = 1$. Their dispersions are given by

$$E_{a/b}(k_z,n) = -\eta k_z + \gamma k_z^3 \pm \sqrt{(k_z + \beta k_z^3)^2 + \frac{2}{l_B^2}|n|} \tag{4.5}$$

for $n \neq 0$, and for $n = 0$ the chiral level is given by

$$E_{k_z,0} = (1-\eta)k_z + (\beta+\gamma)k_z^3. \tag{4.6}$$

The LL dispersions are shown in the bottom panel of Fig. 4.1 which can be directly compared to the corresponding numerical tight-binding calculation in a field displayed in the middle panel. Both make apparent one of the main findings of this chapter — the size and shape of the two inverted pockets almost exactly match when shifted by the arrow Q_{CDW} indicated in Fig. 4.1. These nesting features between entire electron and hole pockets, $E_a(k_z) \approx -E_b(k_z + Q_{CDW})$, are for example well established in parent compounds of iron-based superconductors, where they lead to density wave instabilities even for small interactions[CEE08]. This is of course similar to the usual one-dimensional Peierls instability, which is cut off here by the broken inversion symmetry, but arguably more general.

A direct calculation of the corresponding LL- and pocket-resolved susceptibility, see Fig. C.1 in appendix C.1, confirms the qualitative picture: i) A dominant peak at Q_{CDW} appears in the inter-band component connecting electron and hole pockets; ii) The peak is maximal for scattering between bands with the same LL index n; iii) Due to a small asymmetry between the pockets, which also depends on the LL index, nesting is not perfect which cuts off a true singularity of the susceptibility and introduces a peculiar field dependence. Note that in the case of imperfect particle-hole compensation the pockets would be shifted in energy with respect to each other leading to dominant nesting between branches with different LL indices but the overall pictures remains valid.

4.3. Mean field ansatz

To study the formation of a CDW we add interactions to the single particle theory presented above. Due to the multi-band nature even the simplest contact interaction (strength U) is a sufficient approximation for a short range interaction, as we are interested in the coupling between two different bands. We project the contact interaction to LLs

$$H_{\text{int}} = \frac{U}{2} \sum_{\substack{n_1,n_2,n_3,n_4,\\ p_1,p_2,k_z,k'_z,\\ q_x,q_y,q_z}} e^{iq_y(p_1-p_2-q_x)} J_{n_4,n_1}(\mathbf{q}) J_{n_3,n_2}(-\mathbf{q}) \cdot \\ \sum_{\alpha,\beta=A,B} c^\dagger_{\alpha,n_1,p_1,k_z} c^\dagger_{\beta,n_2,p_2,k'_z} c_{\beta,n_3,p_2+q_x,k'_z+q_z} c_{\alpha,n_4,p_1-q_x,k_z-q_z} \tag{4.7}$$

which introduces additional momentum dependence[Goe11], see appendix C.5 for details.

From the main peaks of bare susceptibility we know that the leading CDW instability arises between electron and hole bands with the very same LL index n. This allows us to simplify the problem considerably by only considering interactions with all $n_{1,2,3,4} = n$ equal. Hence the different Landau levels decouple and we perform the following computations for a fixed Landau level index and combine results for different Landau levels later. Furthermore since the nesting connects the different branches (with creation operators a and b), we are interested in a CDW in $\langle a^\dagger b \rangle$. We introduce the generic CDW wavevector $\mathbf{Q} = (Q_x, Q_y, Q_z)$ to formulate the general mean field theory using the ansatz: $\langle a^\dagger_{p,k_z} b_{p-q_x,k_z-q_z}\rangle = \Delta(k_z, \mathbf{Q}) e^{-ipQ_y} e^{iQ_y q_x/2} \delta(q_x - Q_x)\delta(q_z - Q_z)$.

Our focus are CDWs along the k_z direction and therefore we concentrate on CDW vectors $\mathbf{Q} = \big(0, 0, Q\big)$. We decouple the interaction in the usual way which allows us to write the Hamiltonian in the bilinear form for each LL

$$H_{\mathrm{MF},n}\left(p, k_z\right) = \begin{pmatrix} a^\dagger_{p,k_z} & b^\dagger_{p,k_z-Q} \end{pmatrix} \begin{pmatrix} E_a(p,k_z) & P(k_z) \\ P(k_z)^* & E_b(p,k_z-Q) \end{pmatrix} \begin{pmatrix} a_{p,k_z} \\ b_{p,k_z-Q} \end{pmatrix}. \tag{4.8}$$

The details of the derivation of the off-diagonal elements P in terms of the projected interaction matrix elements[GLS04] and the order parameter Δ are given in appendix C.5. There, we also show that our ansatz gives real electron densities[FPA79]. Knowing P we obtain self-consistent solutions for Δ numerically and thereby determine whether the system supports a CDW or not.

As a check we have confirmed that the wave vector corresponding to the smallest critical interaction for a mean-field CDW transition indeed coincides with the main peak of the bare susceptibility at $Q = Q_{CDW}$.

4.4. Cascade of CDW transitions in temperature

While an independent determination of the CDW wave vector (Q_{CDW}) for each Landau level is possible we choose a common Q_{CDW} for all Landau levels to account for the inevitable inter-Landau-level-coupling, which we neglected in our approximation. This global Q_{CDW} is obtained by maximizing the number of gapped levels, hence represents the energetically most favorable configuration.

In Fig. 4.2 we show the numerical results for the critical temperature of the CDW transition at different magnetic fields and per Landau level n. It becomes clear that in lowering the temperature more and more Landau levels undergo the phase transition, hence we observe a *cascade of successive CDW transitions*. It is important to keep in mind that the magnetic field also changes the spacing between Landau levels and thereby the number of Landau levels crossing the Fermi energy (the degeneracy in each level increases accordingly). To account for this we count the total number of gapped levels at each temperature and magnetic field strength and compute the fraction of this number compared to the number of Landau levels crossing the Fermi energy in the corresponding non-interacting system. This fraction is shown in the bottom panel of Fig. 4.2 and turns out to be roughly independent of field.

4.5. Experimental signatures

Our scenario implies thermodynamic signatures of a high field phase transition, e.g. in specific heat or magnetization, see inset in Fig.4.3. The CDW real space modulation of the electronic density $\rho(\mathbf{r}) \propto \cos(Q_{CDW} \cdot r_z)$ should be detectable via X-ray scattering.

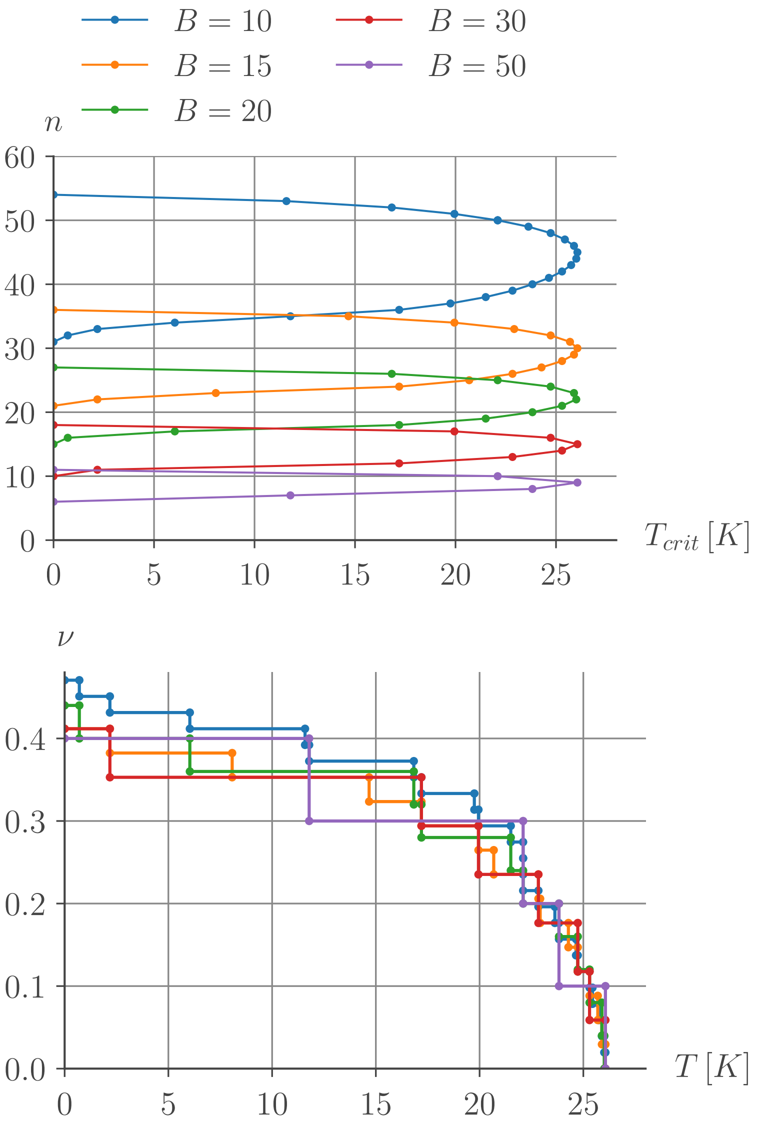

Figure 4.2.: Top panel: Highest critical temperature per Landau level for fixed interaction strength $U = 0.025$ and fixed wave vector $Q_{CDW} = 1.48$ (see discussion in the main text). Bottom panel: Fraction of levels crossing the Fermi energy (when no interaction is considered) that are gapped by a CDW. When lowering the temperature there is a cascade of consecutive CDW transitions leading to an increased fraction of gapped levels. Parameters are the same as for the top panel.

In addition, the suppression of electronic states around the chemical potential entails clear experimental signatures and should be observable for example via STM measurements. In Fig. 4.3 we compare the energy resolved density of states (DOS) as a function

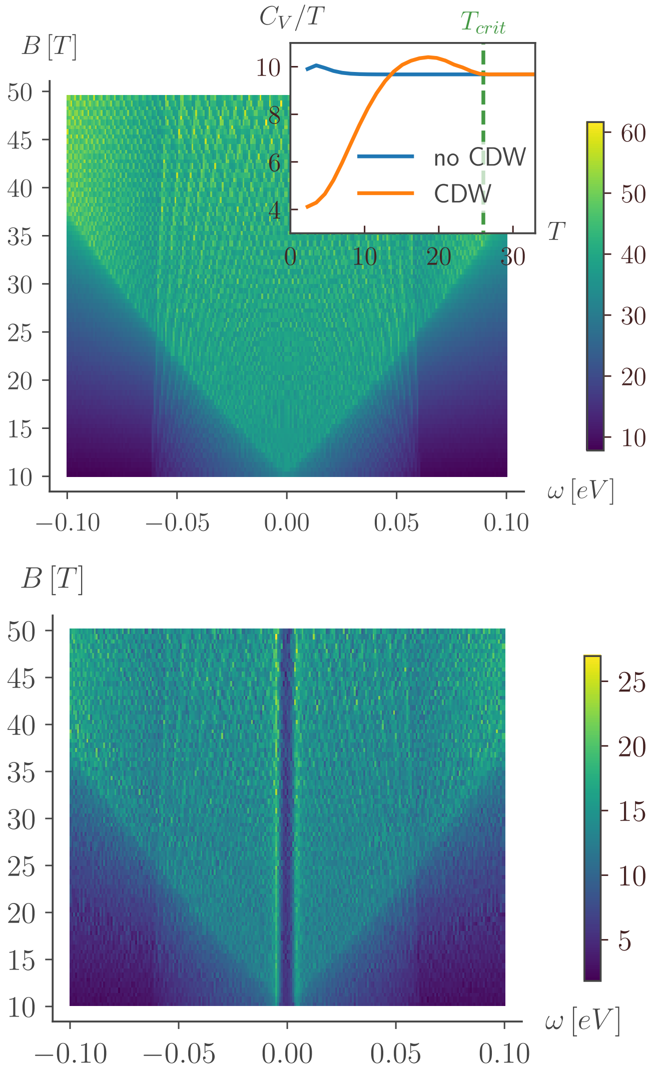

Figure 4.3.: DOS as a function of of magnetic field strength and energy, summed over the 50 lowest Landau levels. When including interactions (bottom panel, numerical result obtained at $T = 4.6K$) a gap opens compared to the case without interactions (top panel). Inset: Temperature dependence of heat capacity C_V/T (arbitrary units) at fixed magnetic field of $B = 20T$. As expected C_V/T is constant (blue line) without the CDW, but taking the CDW into account (orange line) deviations are clearly visible below the critical temperature indicated by the dashed green line.

of magnetic field between a non-interaction system (top panel) and the system with weak interactions (bottom panel). We observe a striking difference at zero energy (near the Weyl point) where the CDW clearly leads to a strong suppression of the DOS. As not all Landau levels are gapped by the CDW for small interactions there is some residual

DOS in this region, hence it is not a complete gap.

Note that the DOS oscillates due to the discreteness of Landau levels. We expect that the corresponding quantum oscillations in thermodynamic observables survive even in regimes in which the CDW opens a full gap[KC15].

Finally, if the magnetic field is not aligned in the direction of the tilt, as chosen in our set-up, the electron- and hole-like pockets of the LLs disappear[UB16] leading to a characteristic suppression of the CDW.

4.6. Discussion

We introduced an exemplary lattice model of a type-II Weyl semimetal and obtained a low energy description that takes finite electron and hole pockets into account. From this we identified emergent nesting properties that occur between electron- and hole-like Landau level branches once the Weyl semimetal is placed in a magnetic field. We developed a general mean-field theory of a Weyl semimetal in a field confirming the intuitive picture of a nesting induced CDW instability. The self-consistent calculations allowed us to trace its dependence on temperature and magnetic field.

Here we focused on the most relevant parts, i.e. intra Landau level couplings between different branches. While we made plausible why these approximations should be valid a more quantitative analysis of the inter Landau level couplings poses interesting questions for future research, as well as a full lattice calculation. We have pointed out several clear experimental signatures of the field induced CDW transition, e.g. in thermodynamics, STM and X-rays.

The reduction of the DOS would also lead to an increased magnetoresistance, which is a feature of great interest in many type-II Weyl systems, as discussed in the following chapter. A similar mechanism has been proposed to explain the magnetoresistance properties of graphite[YF81; Fau+13; LeB+17] Considering the parallel alignment of the tilt and the magnetic field our scenario is only directly applicable to WP_2 [Aut+16; Kum+17], while the geometry is different in the case of WTe_2 [Ali+14] and $Mo_xW_{1-x}Te_2$ [Bel+16a]. A more detailed study of transport properties is desirable and left for future research. However, if our scenario is mutatis mutandis applicable to the non-saturating magnetoresistance of these materials as well there are some immediate consequences: most saliently it would be in contrast to the semiclassical picture suggested in Ref. [Ali+14] which relies on on strict particle hole-symmetry. It is supported by the fact that the magneto transport of WTe_2 has an unusual temperature dependence and that $MoTe_2$ with similar properties is far from particle hole compensated[Thi+17]. Note, that the number of LLs crossing the Fermi level is determined by the magnetic field component $B^{\perp}$ projected along the tilt direction. Hence, a magnetoresistance from LL formation of the form $(B^{\perp})^2$ suggests a $\cos^2\theta$ angular dependence similar to measurements on WP_2 [Kum+17].

Finally, we note that for larger interactions the LL spectrum is fully gapped which should lead to a concomitant three-dimensional Hall plateau[Ber+07] similar to other systems with density wave induced three-dimensional Hall effects[McK+95; BKW95].

5. Quantum oscillations and magnetoresistance in type-II Weyl semimetals

In the previous chapter we studied interaction effects in type-II Weyl semimetals and found the formation of a CDW. Here, we investigate how this CDW affects the magnetoresistance properties, regarding the scaling behaviour and the temperature dependence of the magnetoresistance's oscillations. These findings may provide an additional route to observe the CDW and its consequences in experiments. Recently, several experiments on type-II Weyl semimetals reported a very large magnetoresistance[Ali+14; Zen+16; Kum+17]. The observed B^2 scaling of the magnetoresistance was hitherto explained by a semi-classical derivation. In this chapter, which is based on the publication [TBK18, in preparation], we provide a fully quantum mechanical computation of the magnetoresistance, using the Kubo formula introduced in chapter 1.1.4. Since there is currently a widespread interest in type-II Weyl semimetals with large magnetoresistance, this chapter is a timely contribution to the field.

5.1. Introduction

Immediately following the discovery of type-I Weyl semimetals, it was realized that type-I Weyl fermions were associated with novel transport phenomena, such as the chiral anomaly[NN83; LYQ13; SY12; Gru12; ZB12; GT13; Par+14; Hua+15; Zha+16; KGM15; KGM17; BKS18]. In contrast, due to the concealed nature of type-II Weyl fermions, it is a priori less obvious that they would lead to interesting measurable effects. However, transport measurements on type-II Weyl semimetals have arguably proven even more intriguing: most saliently, experiments on type-II Weyl semimetals found an extremely large magnetoresistance, which did not saturate until the highest accessible magnetic fields[Ali+14; Kum+17; Zen+16]. In all these experiments a scaling of the magnetoresistance close to B^2 was found. Furthermore, the magnetotransport in these materials is strongly dependent on the direction of the applied magnetic field.

In addition, a number of experiments found an unusual temperature dependence of transport properties[Tho+15; Wu+15; Fat+17; Ram+17]. On the one hand, these could be related to the strong temperature dependence of the chemical potential, as expected for a low density system when k_BT and the effective Fermi energy are of similar order of magnitude. On the other hand, it could be a direct signature of a many-body instability, such as a field induced excitonic insulator[Khv01] or a density wave transition[Tre+17a]. The CDW scenario was put forward in a recent work of us[Tre+17a] motivated by the observation that the Landau level structure of type-II Weyl semimetals[UB16] shows emergent nesting properties as illustrated in Fig. 5.1. At zero field, the electron and hole pockets have different shapes. However, a strong magnetic field leads to nested, quasi-one-dimensional electron and hole pockets prone to a CDW instability already for weak interactions. Such an intra-Weyl cone CDW would have a small wave vector and the associated breaking of translational symmetry should be observable in scattering experiments. Here, we show that a field induced CDW leads to a very rich phenomenology of magnetoresistance properties in type-II Weyl semimetals.

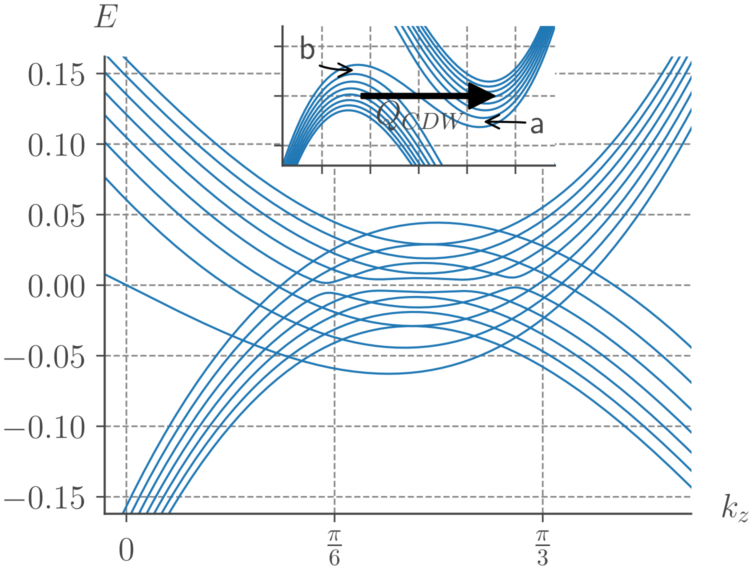

Figure 5.1.: Dispersion of a type-II Weyl semimetal with a magnetic field ($B = 7.5T$) induced CDW as given in (5.9). Energy is given in units of eV, k_z in reciprocal lattice vectors. The main panel shows the folded dispersion in the presence of a CDW, which gaps out part of the Landau levels, with the lower branch (b) shifted by Q_{CDW}. The inset highlights the field induced nesting property between electron and hole type pockets of the normal state with the CDW wave vector Q_{CDW}. It further includes labels for the two branches a and b.

5.2. Theory

We consider a generic and minimal model of a type-II Weyl semimetal, which can be theoretically derived as a low energy expansion of a lattice model[UB16] as given in [Tre+17a]. A crucial observation is to include not only terms linear in momentum but also the next non-zero terms (in this case k_z^3), to account for electron and hole pockets, see Fig.5.1.

We use the general low energy theory of a type-II Weyl semimetal with additional third-order terms in k_z along the tilt direction and concentrate on one of the Weyl cones:

$$\hat{H}_0^{\text{eff}} = (-\eta k_z + \gamma k_z^3)\sigma_0 + (k_z + \beta k_z^3)\sigma_z + k_x\sigma^x + k_y\sigma^y. \tag{5.1}$$

The parameters $\eta = -(t_1 + 2t_2), \beta = -\frac{1}{6}$ and $\gamma = -\frac{1}{6}(t_1 + 8t_2)$ are directly related to the lattice model's hopping parameters, where we choose $t_1 = -0.8$ and $t_2 = -0.6$. Throughout this work, for concreteness, we consider the exemplary values $\hbar v_F = 4\,\text{eV}\text{Å}$ and the lattice constant of $a_0 = 28\,\text{Å}$. In this simple tight binding model, the electron and hole pockets extend to a large fraction of the unit cell, whereas in typical materials they only cover a much smaller part. Here, the size of the unit cell is not important, as the size of the electron and hole pockets defines the relevant length scales. In consequence, we choose a relatively large lattice constant for the exemplary model to obtain small electron and hole pockets in momentum space, so that they are similar to the ones in actual materials.

For simplicity and transparency, we focus on situations with the magnetic field directed along the tilt of the Weyl cone, i.e. $B \parallel z$ when the tilt direction is along k_z, and only briefly comment on the generalization to generic directions in the discussion. The field $\mathbf{B} = \nabla \times \mathbf{A}$ is then introduced by a minimal coupling of the vector potential, which we consider to be $\mathbf{A} = (0, Bx, 0)$ in the Landau gauge, to the crystal momentum $\mathbf{\Pi} = \hbar\mathbf{k} - \frac{e}{c}\mathbf{A}$. We define the standard raising and lowering operators

$$a = \frac{l_B}{\sqrt{2}\hbar}\left(\Pi_x - i\Pi_y\right) \qquad \text{and} \qquad a^\dagger = \frac{l_B}{\sqrt{2}\hbar}\left(\Pi_x + i\Pi_y\right) \tag{5.2}$$

with $[a, a^\dagger] = 1$, where we introduced the magnetic length

$$l_B = \sqrt{\frac{\hbar}{eB}}\,. \tag{5.3}$$

Consequently, we arrive at the following Hamiltonian describing the low energy theory

$$H_0 = \int \mathrm{d}^3r \begin{pmatrix}\Psi_A^\dagger(\mathbf{r}) & \Psi_B^\dagger(\mathbf{r})\end{pmatrix} \hbar v_F \begin{pmatrix} (1-\eta)k_z + (\gamma+\beta)k_z^3 & \frac{\sqrt{2}}{l_B}\hat{a}^\dagger \\ \frac{\sqrt{2}}{l_B}\hat{a} & -(1+\eta)k_z + (\gamma-\beta)k_z^3 \end{pmatrix} \begin{pmatrix}\Psi_A(\mathbf{r}) \\ \Psi_B(\mathbf{r})\end{pmatrix} \tag{5.4}$$

with the wave functions

$$\Psi_A^\dagger(\mathbf{r}) = \sum_{n,p,k_z} e^{ik_z z}\psi_{n,p}(x,y)\hat{c}_{A,n,p,k_z} \tag{5.5}$$

$$\Psi_B^\dagger(\mathbf{r}) = \sum_{n,p,k_z} e^{ik_z z}\psi_{n-1,p}(x,y)\hat{c}_{B,n,p,k_z} \tag{5.6}$$

and the normalized Harmonic Oscillator wave functions

$$\psi_{n,p}(x,y) = \frac{1}{\sqrt{L}}e^{ipx}\left(\pi 2^{2n}(n!)^2\right)^{-1/4} e^{-\frac{1}{2}(y+p)^2} H_n(y+p) \tag{5.7}$$

including the Hermite polynomials H_n. Note, that there is an extra shift of the Landau level index from n to $n-1$ for the B sublattice part of the wave function.

In the braket notation we write the states as spinors in the A/B basis and perform a rotation such that the Hamiltonian becomes diagonal

$$\begin{pmatrix} |n, k_z, p, a\rangle \\ |n-1, k_z, p, b\rangle \end{pmatrix} = U(n, k_z, p) \begin{pmatrix} |n, k_z, p, A\rangle \\ |n-1, k_z, p, B\rangle \end{pmatrix} \tag{5.8}$$

where U is a unitary transformation that is easily obtained from (5.4). The energies, labeled by $s \in a, b$ for $|n, p, k_z, s\rangle$ are given by

$$E_{n,a/b}(k_z) = \hbar v_F \left(-\eta k_z + \gamma k_z^3 \pm \sqrt{(k_z + \beta k_z^3)^2 + \frac{2}{l_B^2}|n|} \right) \tag{5.9}$$

for $n \neq 0$. For $n = 0$, the energy of the chiral level is

$$E_{0,k_z} = \hbar v_F \left((1-\eta) k_z + (\beta + \gamma) k_z^3 \right) . \tag{5.10}$$

The Landau level degeneracy becomes apparent as E does not depend on p. Note that the chiral mode corresponds to the $(1\ 0)^T$ spinor already in the original basis. Therefore, there is no basis transformation $U(n=0)$ for the chiral level.

Following our recent work [Tre+17a], we take into account the effect of an interaction induced CDW. Due to the special Landau level dispersion, it is sufficient to restrict the analysis of the weak coupling instability to the simplest form of a contact interaction. This interaction, projected onto the Landau level bands, is given by

$$\begin{aligned} H_{\text{int}} = \frac{U}{2} \sum_{\substack{n_1, n_2, n_3, n_4, \\ p_1, p_2, k_z, k_z', \\ q_x, q_y, q_z}} & e^{i q_y (p_1 - p_2 - q_x)} J_{n_4, n_1}(\mathbf{q}) J_{n_3, n_2}(-\mathbf{q}) \\ & \cdot \sum_{\alpha, \beta = A, B} c^\dagger_{\alpha, n_1, p_1, k_z} c^\dagger_{\beta, n_2, p_2, k_z'} c_{\beta, n_3, p_2 + q_x, k_z' + q_z} c_{\alpha, n_4, p_1 - q_x, k_z - q_z} \, . \end{aligned} \tag{5.11}$$

Details of the matrix elements $J(q)$ and useful analytic simplifications of them are given in Appendix D for our choice of a uni-directional CDW with $q_x = q_y = 0$.

At strong magnetic fields, even weak interactions lead to CDW transitions because of the nesting between the electron and hole pockets, $E_{n,a}(k_z) \approx -E_{n,b}(k_z + Q_{CDW})$ (see Fig.5.1). In a mean-field framework, as presented in [Tre+17a], the quartic interactions are decoupled, leading to an effective CDW Hamiltonian

$$H_{\text{MF},n}(k_z) = \begin{pmatrix} a^\dagger_{n,k_z} & b^\dagger_{n,k_z - Q} \end{pmatrix} \begin{pmatrix} E_a(n, k_z) & P(k_z) \\ P(k_z)^* & E_b(n, k_z - Q) \end{pmatrix} \begin{pmatrix} a_{n,k_z} \\ b_{n,k_z - Q} \end{pmatrix} . \tag{5.12}$$

The analytical form of the off-diagonal matrix elements P is derived from the contact interaction projected to the Landau level band structure and given in [Tre+17a] and appendix C.5.

5.2.1. Kubo formula of the conductivity

We concentrate on the transport properties perpendicular to the magnetic field, which are obtained from the in-plane conductivity $\sigma_{\alpha\alpha}$ with $\alpha = x, y$. We apply the standard Kubo formula for conductivity which is given by[TC15; SY16]:

$$\sigma_{\alpha\beta}(\omega) = \frac{i\hbar}{2\pi l_B^2} \sum_{\zeta,\zeta'} \frac{f(E_{\zeta'}) - f(E_\zeta)}{E_\zeta - E_{\zeta'}} \frac{\left\langle \zeta \middle| \hat{j}_\alpha \middle| \zeta' \right\rangle \left\langle \zeta' \middle| \hat{j}_\beta \middle| \zeta \right\rangle}{\hbar\omega + E_{\zeta'} - E_\zeta + i\hbar/(2\tau)} \tag{5.13}$$

using the short-hand notation $\zeta = \{n, k_z, a/b\}$, $f(E)$ for the Fermi function, and τ as a scattering-induced lifetime. The summation over p is already executed and accounts for the Landau level degeneracy factor $\frac{1}{2\pi l_B}$. We assume a constant time τ due to impurity scattering. This simplifying assumption is motivated from the very weak frequency dependence of the density of states of a type-II Weyl semimetal with finite electron and hole pockets.

To evaluate the Kubo formula we calculate the current operators as

$$\hat{j}_\alpha = e\hat{v}_\alpha = \frac{e}{\hbar} \frac{\partial \hat{H}}{\partial \Pi_\alpha} \tag{5.14}$$

with the Hamiltonian matrix (5.4) in the form

$$H = \hbar v_F \begin{pmatrix} (1-\eta)k_z + (\gamma+\beta)k_z^3 & \frac{1}{\hbar}(\Pi_x + i\Pi_y) \\ \frac{1}{\hbar}(\Pi_x - i\Pi_y) & -(1+\eta)k_z + (\gamma-\beta)k_z^3 \end{pmatrix}, \tag{5.15}$$

so

$$\hat{j}_x = e v_F \sigma_x \tag{5.16}$$

$$\hat{j}_y = -e v_F \sigma_y \,. \tag{5.17}$$

From this, we obtain the relevant matrix elements in the basis of (5.4)

$$\left\langle n, k_z \middle| \hat{j}_x \middle| n', k_z' \right\rangle_{A/B} = \left\langle n, k_z \middle| \begin{pmatrix} 0 & \delta_{n,n'-1} \\ \delta_{n-1,n'} & 0 \end{pmatrix} \middle| n', k_z' \right\rangle_{A/B} . \tag{5.18}$$

These current operators are then transformed with two subsequent unitary transformations, first with (5.8) and second with the one that diagonalizes the CDW Hamiltonian (5.12) with the mean-field energies E_ζ appearing in the Kubo formula.

5.3. Results

The magnetoresistance is usually given in % and defined as

$$MR(B) = \frac{\rho(B) - \rho(0)}{\rho(0)} . \tag{5.19}$$

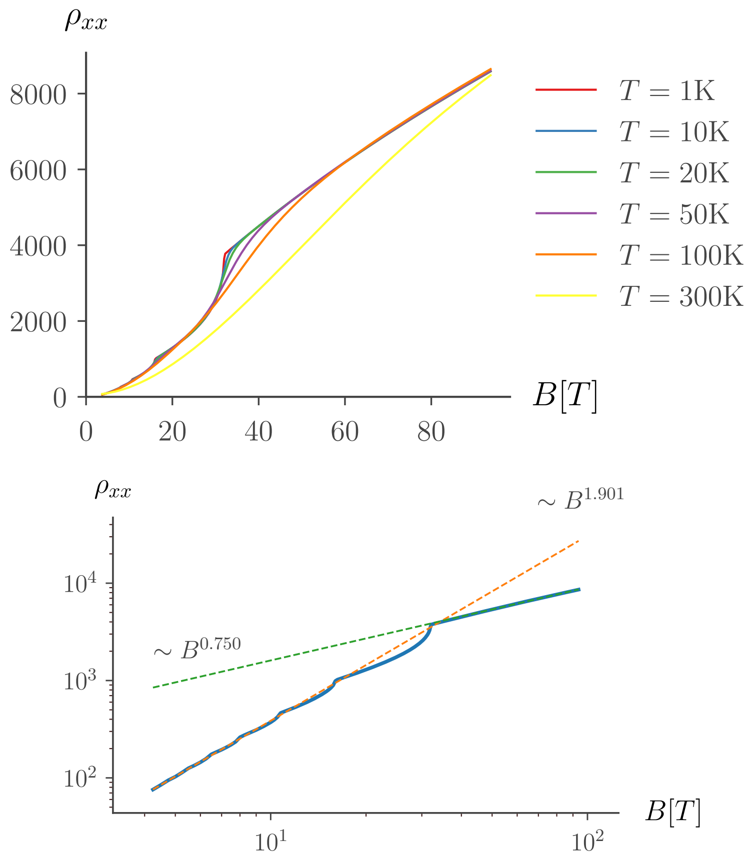

Figure 5.2.: Transversal resistivity ρ_{xx} (arbitrary units) vs. magnetic field (in Tesla) for different temperatures T. The top panel shows clearly the crossover around $B_Q \simeq 31$T and additionally pronounced quantum oscillations (at low temperatures and $B < B_Q$). The bottom panel displays the $T = 1K$ data of the top panel on a log-log scale. The dashed lines show least-squares fits for different regimes of B. The corresponding exponents for the fitted power law behaviour are indicated.

There is no CDW at zero magnetic field, therefore $\rho(0)$ is equal in the cases with and without interactions. We are mainly interested in the qualitative behaviour of the magnetoresistance and not in exact quantitative values, which would require a detailed microscopic description of a specific material. Hence, we concentrate on the behavior of the resistivity $\rho(B)$, which is qualitatively equivalent to the magnetoresistance. We consider the case with zero chemical potential, where the dispersion relation is particle-hole symmetric.

A hypothetical imbalance between particle and hole pockets leads quickly to a saturation of the magnetoresistance in the semiclassical picture. We verified that this prediction holds also for the quantum mechanical computation in the non-interacting case with a constant scattering time. An extension to the CDW case would require further adaptations to the mean-field calculations beyond the scope of the present work.

5.3.1. Magnetoresistance

In the compensated situation considered here, the Hall conductivity σ_{xy} vanishes and $\sigma_{xx} = \sigma_{yy}$ because of the rotational symmetry. Hence, the resistivity along the in-plane x-direction can be directly calculated from the corresponding conductivity

$$\rho_{xx} = \frac{\sigma_{xx}}{\sigma_{xx}^2 + \sigma_{xy}^2} = \frac{1}{\sigma_{xx}} \, . \tag{5.20}$$

First, we discuss the case without interactions and hence without CDW. The full temperature dependence as calculated from the Kubo formula (5.13) is shown in Fig. 5.2. For small fields, our results agree well with a semiclassical model of two bands with perfectly compensated particle and hole pockets[AM76] predicting a scaling of the resistivity as $\sim B^2$. Note that the numerical fit of the data yields powers of B slightly smaller than 2 because the oscillations at higher field are not symmetric around the expected B^2 background. Therefore, a numerical fit will weakly depend on the range of magnetic fields considered. At the same time we note that several experiments[Kum+17; Ali+14; Zen+16] experimentally found a scaling with powers between 1.8 and 2, similar to our results.

The semiclassical prediction obviously neglects the quantum oscillations due to discreteness of the Landau levels, which become more pronounced at higher magnetic fields and lower temperature. We define the magnetic field strength B_Q as the minimum field at which the lowest Landau level reaches the Fermi energy. Beyond this *quantum limit* $B > B_Q$ only the chiral mode contributes to the density of states at zero energy. In addition to the semiclassical quadratic scaling for $B \ll B_Q$ we observe a crossover to a different scaling $\rho \sim B^{0.75}$ above the quantum limit, see Fig. 5.2 (bottom panel).

The magnetic field strength associated with the crossover to the quantum limit is $B_Q \simeq 31T$ for our exemplary tight binding model. This magnetic field strength B_Q depends strongly on the size of the electron and hole pockets. We denote the size of the pocket with k_P. The corresponding length scale is given by $1/k_P$. As the magnetic length l_{B_Q} at the quantum limit is proportional to that length scale $1/k_P$, we find $B_Q \propto k_P^2$.

Next, we include the effect of a low temperature CDW transition. We will use the same exemplary parameters as in our previous work [Tre+17a]. There, we observed that at low temperatures a constant fraction ($\simeq 0.5$) of the Landau levels crossing the Fermi energy is gapped out by the CDW, regardless of the magnetic field. This statement is only valid in the regime $B \ll B_Q$ studied in [Tre+17a] where the fraction is nearly a continuous number, due to the large number of Landau levels. For higher fields, we expect this fraction to vary due to the discrete number of Landau levels. In the quantum limit there is no Landau level left that could be gapped by a CDW, therefore the fraction of Landau levels gapped by the CDW then drops to zero.

The resulting resistivity ρ_{xx} obtained from the mean-field results is shown in Fig. 5.3 for an intermediate regime of magnetic fields and compared to the case with no inter-

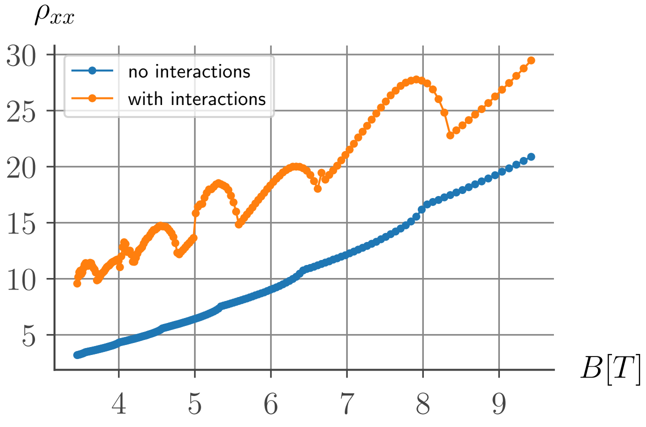

Figure 5.3.: Transversal resistivity ρ_{xx} (arbitrary units) for a Weyl semimetal without interactions and with an interaction induced CDW at a temperature of $T = 0.5K$.

actions. We observe an CDW-induced increase in resistivity by a factor of $\sim 2-4$ in the range of $1.25T < B < 3.75T$ for our choice of parameters. This relative increase is robust to different parameter sets for the lattice model and mean-field parameters (e.g. values of the interaction U), while the exact range of the magnetic field is still affected by the size of the pockets due to the scaling properties discussed above. Note that, upon approaching the quantum limit at B_Q, this factor slowly decreases with increasing B. We can intuitively understand this behaviour remembering that the fraction of gapped levels is constant at low magnetic fields and must change at high magnetic fields.

5.3.2. Quantum oscillations

In the large magnetic field regime quantum oscillations from the discrete nature of the Landau levels appear. In Fig. 5.4 we show quantum oscillations from low ($T = 0.5K$) to high ($T = 27.5K$) temperatures, where "high" temperature has to be understood in comparison to the critical temperature of the CDW.

The figure shows only the oscillatory part of ρ, where the power law behaviour was subtracted, vs. the inverse magnetic field. The power law is obtained by a numerical least-squares fit in log-log space. We conclude that the CDW formation significantly increases the amplitudes of the quantum oscillations in resistivity. Experimental observations of quantum oscillations usually consider the conductivity (the Shubnikov-De Haas effect), which, being the inverse resistivity, would be decreased by the CDW.

A main result of the present study concerns the impact of the CDW formation on the temperature dependence of the quantum oscillation amplitudes. We determine the amplitudes from the oscillatory part of ρ as shown in Fig. 5.4. We define the amplitude as the difference of a consecutive local maximum and minimum below a fixed magnetic field value, and we checked that the qualitative behaviour is independent of the magnetic field at which the amplitude is determined. In Fig. 5.5 we compare the decay of the

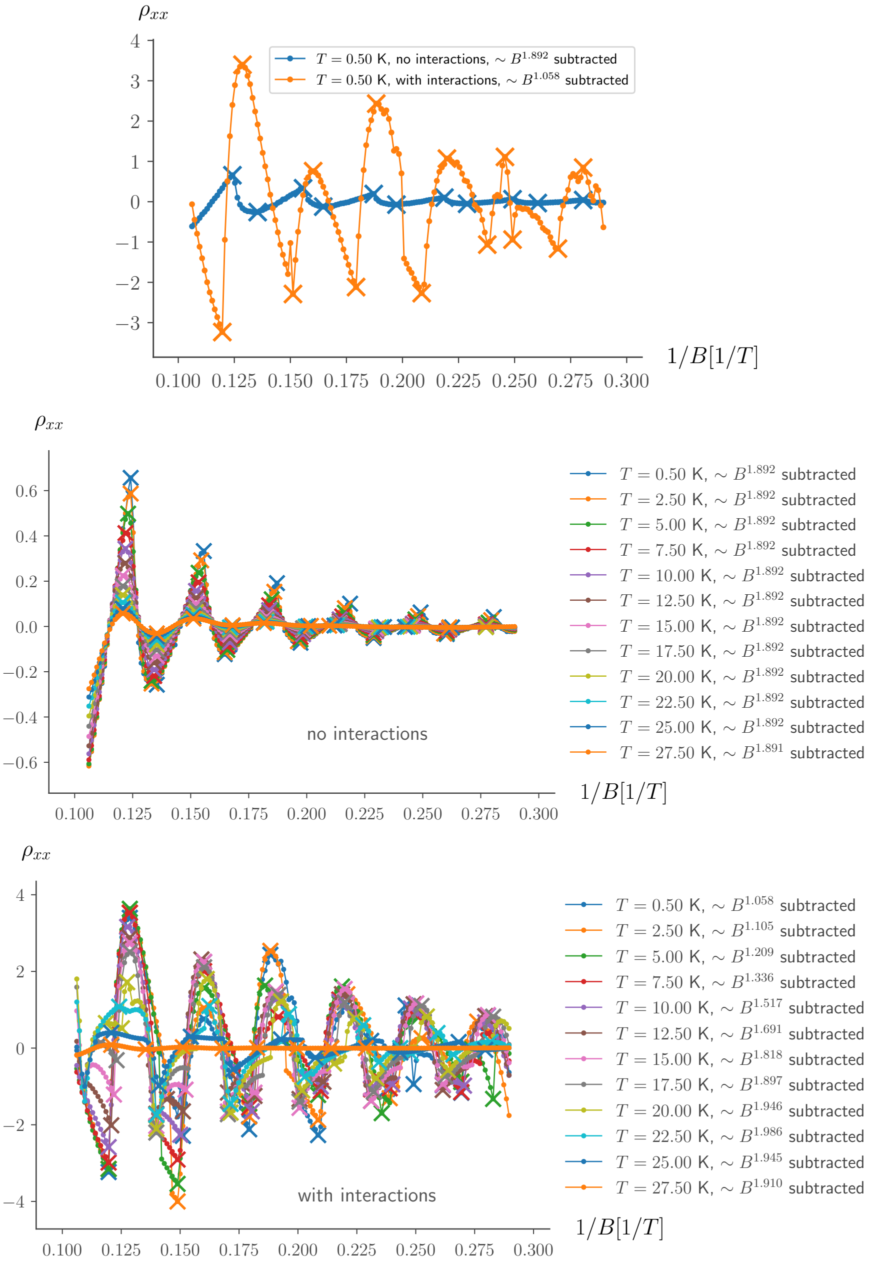

Figure 5.4.: Quantum oscillations compared with and without interactions. The power law background is subtracted as discussed in the main text. In the top panel oscillations with and without interactions are compared at $T = 0.5K$. The middle panel shows how oscillations without interactions evolve with different temperatures. The bottom panel displays the temperature evolution when including interactions.

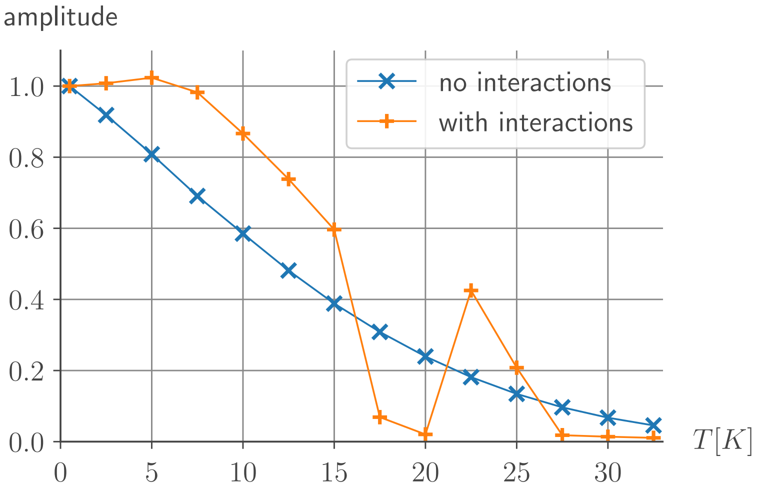

Figure 5.5.: Amplitudes of the magnetoresistance oscillations vs. temperature. Amplitudes are normalized to 1 at $T = 0.5K$ (the smallest temperature value considered) for the two cases independently. The numerical results are shown as crosses, the solid lines are a guide to the eye.

amplitude for increasing temperature for a representative case with and without CDW. While the case without CDW (blue cross) shows the usual monotonic decrease similar to the Lifshitz-Kosevich temperature dependence[Sho84], the system with CDW clearly deviates from this universal behavior. More importantly, we observe a clear plateau and then an increase of the amplitude for increasing T at very low temperatures. This result is in clear contrast to the monotonic decrease of the Lifshitz-Kosevich temperature dependence. We expect both signatures to be clearly visible in experiments.

We stress that the oscillations in the CDW case are less regular both in temperature and in magnetic field, as shown in the bottom panel of Fig. 5.4. This behaviour can be understood considering the cascade of CDW transitions discussed in [Tre+17a]. In the non-interacting case, there is only one way of gapping out Landau levels: by increasing the magnetic field and thereby the Landau level spacing, pushing Landau levels above the Fermi energy. In the interacting case, however, for each Landau level there is a competition between two mechanisms: gapping the Landau level by a CDW transition or by the simple increase of the Landau level spacing similar to the non-interacting case. Which mechanism is responsible for gapping out a specific Landau level depends on the magnetic field and on the temperature. This dependence is different for each Landau level[Tre+17a]. Together, this leads to the complex behaviour of the oscillations in the interacting case, as seen in Fig. 5.4 (bottom panel).

The highest critical CDW temperature for any Landau level is $\simeq 25K$ in our exemplary model. Below this temperature, the cascade of CDW transitions affects the oscillations, and the oscillation amplitude is not as clearly defined as in the non-interacting case. Following our fixed protocol of determining the oscillation amplitudes, we obtain the results shown in Fig. 5.5. These amplitudes correspond to the first set of consecutive minima and maxima, i.e. at the highest magnetic field as shown in Fig. 5.4, where local extrema are marked by crosses.

5.4. Discussion

We calculated the magnetoresistance of a type-II Weyl semimetal without and with a magnetic field induced CDW. Earlier, the unsaturated and (nearly) quadratic magnetoresistance of several compounds was attributed to the compensation of electron and hole pockets, based on semiclassical computations. Here, we confirmed this result for non-interacting type-II Weyl semimetals using a microscopic model and linear response theory. Further, we showed that a critical field strength B_Q exists, at which the quadratic scaling breaks down even for perfect compensation. We discussed how this field strength, which corresponds to the quantum limit, depends on the materials parameters.

We then focussed on the effects of interactions, which lead to a CDW transition as reported in [Tre+17a]. In terms of magnetoresistance this CDW transition leads to numerous effects: At low fields, the resistivity (and hence the magnetoresistance) is increased and at high fields the resistivity approaches again the values of the non-interacting case. Most importantly, the temperature dependence of the resistivity oscillations is in contrast to the universal Lifshitz-Kosevich behaviour. Therefore, magnetoresistance measurements are an appropriate tool to look for signatures of the conjectured CDW phase in type-II Weyl semimetals.

We note that the number of Landau levels crossing the Fermi level is determined by the magnetic field component $B^{\perp}$ projected onto the tilt direction. Hence, a magnetoresistance from Landau level formation of the form $(B^{\perp})^2$ suggests a $\cos^2\theta$ angular dependence similar to measurements on WP_2 [Kum+17].

At the time of this writing, it seems likely that all materials showing unsaturated magnetoresistance may indeed have perfectly compensated electron and hole pockets. This has been consensus for WTe_2. Another material, WP_2, likewise displaying an extreme magnetoresistance but with a more controversial provenance, has recently been argued to be particle-hole compensated as well[Raz+18]. For WTe_2 it indeed appears, that the extreme magnetoresistance is sensitively depending on fine-tuned particle hole symmetry[Gon+17; Cap+18].

We also note that an extreme magnetoresistance has been identified in the topologically trivial material LaAs[Yan+17]. In our setup it is quite clear that the topology of the Weyl node is not the root of this effect—nevertheless, the band structure of a type-II Weyl node is perfectly primed to allow this effect. Via the emergent nesting in a strong magnetic field, we argue that the appearance of a CDW is almost unavoidable.

Intriguing prospectives for future research include taking into account interactions within the $n = 0$ chiral Landau level, to consider finite frequency optical conductivity and to investigate the effect of doping away from particle-hole compensation. The latter generalization would include the relaxation of several approximations made and justified in [Tre+17a], including the simple contact interaction and the restriction of the interaction to Landau level branches with equal Landau level index.

Finally, beyond Weyl semimetals, it will be worthwhile to extend the general idea that field-induced density wave transitions can strongly affect the amplitude scaling of quantum oscillation measurements[Pez+17; Shi+18] and hence the interpretation of the corresponding data.

6. Conclusion

In this thesis we discussed the electric transport properties of tilted Weyl semimetals with the Fermi level at the nodal point. Hence, our results apply to materials with suitable stochiometry, which leads to the nodal point being at the Fermi level. Previously research on transport properties of Weyl semimetals focussed on isotropic Weyl cones exclusively. While in the context of high energy physics such an isotropy is dictated by the Lorentz invariance, there is no reason to expect Weyl cones in condensed matter realizations to be symmetric. We have discussed anisotropies and tilt, which both break this symmetry, and we found the tilt to be most intriguing.

In general, the research of this thesis was driven by the interest in a specific physical system — tilted Weyl semimetals — and was not aimed at developing new methods. Therefore, we mostly applied well-established methods, e.g. mean-field theory, linear response theory and the scattering matrix formalism. Nonetheless, each method was adapted to the specific problem, most often by combining analytic and numerical work. In general, we began by performing as many analytical simplifications and calculations as possible, until we reached a situation where the equations turned out to be unsolvable analytically. From this point on we applied numerical methods, which we implemented from scratch, relying only on programming libraries for basic mathematical operations[WCV11; Oli07]. The preparatory analytical work allowed us to study much larger systems numerically than we could have accessed by "brute force" or ab initio methods. Hence, the combination of analytics and numerics turned out to be a powerful solution. A good example for this general strategy is the mean field calculation in chapter 4, where the physical approximations and the analytical simplifications led to numerics which were effectively one-dimensional in the tilt direction. Additionally, the use of already established methods allowed us to quickly combine a variety of techniques to find convincing answers. A prime example of this approach is chapter 3, where we combined three methods (SCBA, S-Matrix and KPM) and an intuitive physical argument. Each method started from a different point of view and together the results provided a coherent picture, underlining their credibility.

We distinguished between tilted (type-I, chapters 2 and 3) and over-tilted (type-II, chapters 4 and 5) Weyl cones. For both classes, we found properties of the electronic transport that can serve as experimental signatures of a tilt. These signatures present a complementary way to experimentally access the tilting parameter in Weyl materials compared to directly imaging the dispersion using spectroscopy.

Notably, the publication [Tre+15], on which chapter 2 is based, was the first publication to discuss the relevance of the tilt and to point out observable consequences thereof. In chapter 2, we applied the scattering theory formulation to compute the dimensionless conductance g and the Fano factor F of tilted Weyl semimetals. We briefly discussed the ubiquitous anisotropies of Weyl cones, showing that they can be understood by a simple rescaling and do not lead to unexpected signatures. While the tilt does not alter the topology of the band structure, it nevertheless affects the dimensionless conductance g and Fano factor F. Especially the latter observation is remarkable, since the Fano factor is often found to be a universal number, that does not depend on system-specific details. We found that the influence of the tilt on the Fano factor is dependant on the relative orientation between tilt and transport direction. Still, the Fano factor will only increase with a tilt compared to the isotropic case and hence it could be a valuable experimental signature to identify tilted cones by transport measurements.

We extended the discussion to the case of two-dimensional Dirac cones as well, where tilts result in similar effects. It turns out, however, that due to the symmetry properties in the most pertinent example graphene, the tilt will only show up under lattice deformations and will typically be relatively small. For other two-dimensional materials, e.g. α–(BEDT-TTF)$_2$I$_3$ [Goe+08], the tilt of the linear dispersion might be stronger, but we note that the Dirac cone in two dimensions is not topologically protected and hence less stable than the Weyl cones in three dimensions. Hence, the experimental signatures of a tilt are presumably much harder to observe in two-dimensional materials.

In chapter 3 we studied again the dimensionless conductance and the Fano factor for tilted Weyl cones, but included the effect of disorder. To this end we applied several methods, whose combined results yielded a coherent picture. The methods included the self-consistent Born approximation, a numerical scheme based on the concatenation of scattering matrices and the kernel polynomial method.

The existence of a disorder-induced phase transition from a quasi-ballistic weak disorder phase to a diffusive strong disorder phase was already known for isotropic Weyl cones[Sbi+14]. We found that this phase transition continues to exist in the presence of a tilt, but the critical disorder strength is reduced with increasing tilt. As the tilt approaches the critical value, where one band of the Weyl cone is completely flat in the linear approximation, the critical disorder strength approaches zero. So in the presence of disorder, the tilt-induced phase transition from a type-I Weyl semimetal (with a point-like Fermi surface) to a type-II Weyl semimetal (with finite particle and hole pockets at the nodal point) is always preceded, at any finite disorder strength, by a disorder-induced transition to a diffusive phase with a finite density of states at the nodal point.

We further concluded that there is a family of weak-disorder fixed points distinguished by their effective tilt. The value of this effective tilt in turn affects the Fano factor, as discussed for the bare tilt in chapter 2. This again highlights how valuable the Fano factor is as an experimental signature.

Lattice deformations, like strain or pressure, generally induce changes in the band structure which also affect the tilt. As the critical disorder strength of the disorder phase transition depends on the tilt, it might be possible to drive a system through this phase transition by changing external parameters. This opens up a completely new route for the observation of the disorder phase transition, as the disorder realization itself in condensed matter samples cannot be easily controlled after the sample creation. It might be necessary, however, to start the tilt-induced phase transition already at a close-to-critical disorder strength, so that only a relatively minor change in the band structure is sufficient to drive the system through the quasi-ballistic-to-diffusive phase transition.

When looking for the experimental signatures, which we proposed for type-I Weyl semimetals, it is important to keep in mind the full band structure of the material under consideration. The first experiments finding Weyl semimetals were all observing time-reversal symmetric Weyl semimetals[Xu+15; Lu+15; Lv+15; Hua+15; Zha+15] with additional states crossing the Fermi level. Later experiments also reported the observation of time-reversal symmetry breaking Weyl semimetals[Bor+15; Liu+17b; Chi+16; Liu+17a]. In the reported materials additional states at the Fermi level are also present and in some of them the Weyl cones are not exactly at the Fermi energy. Therefore, the full transport properties in all Weyl semimetals known to date will be a combination of contributions of the Weyl nodes and the other states at the Fermi level. There are other, still hypothetical, time-reversal symmetry breaking Weyl semimetals, which are predicted in the pyrochlore iridates[Wan+11; Ber+15; KTB17], where the only states crossing the Fermi level are Weyl nodes. In these materials it would be easier to observe the sole contribution of the Weyl nodes.

In the second part of this thesis we turned our attention to type-II Weyl semimetals, where the tilt is so strong, that finite electron and hole pockets form around the nodal point. In chapter 4 we studied a low energy theory of type-II Weyl semimetals, which was based on an exemplary lattice model. We specified the importance of the higher order terms in the low energy description to capture the effects of the pockets. When placed in a magnetic field, the band structure is altered and forms Landau levels that are flat in two dimensions. Including these higher order terms in the low energy description allowed us to describe the nesting property, which occurs along the tilting direction between electron- and hole-like Landau level branches. We developed a general mean-field theory of a type-II Weyl semimetal in a magnetic field, so that we were able to take interactions into account. The mean field calculation confirmed our intuitive picture of a nesting-induced CDW instability. Further, we were able to trace the CDWs dependence on temperature and magnetic field. Based on these results we proposed several clear experimental signatures of the field-induced CDW transition. To keep the computations tractable, we introduced and justified several approximations, including a simple contact interaction and restricted inter Landau level couplings. The relaxation of each of these approximations would lead to interesting new questions and research possibilities.

Based on the results of chapter 4, we calculated the resistivity of a type-II Weyl semimetal in a magnetic field in chapter 5. We compared the case without and with interactions. In the case of a non-interacting type-II Weyl semimetal, we confirmed the unsaturated and (nearly) quadratic magnetoresistance for compensated electron and hole pockets, which was previously explained in a semi-classical picture, using a microscopic model and linear response theory. Further, we showed that a critical field strength B_Q exists, at which the quadratic scaling breaks down even for perfect compensation. We discussed how this field strength depends on the material's parameters.

Next, we focussed on the effects of interactions, which lead to a CDW transition as reported in [Tre+17a]. In the case of interacting type-II Weyl semimetals, a CDW develops as discussed in chapter 4, which leads to numerous effects in terms of magnetoresistance properties: At low fields the resistivity (and hence the magnetoresistance) increases relative to the non-interacting case by a numerical factor, while at very high fields (above the quantum limit) the resistivity approaches again the values of the non-interacting case. More strikingly, the temperature dependence of the resistivity oscillations is no longer monotonic, which is in contrast to the universal Lifshitz-Kosevich behaviour. Therefore magnetoresistance measurements are an appropriate tool to look for signatures of the CDW phase in type-II Weyl semimetals and it will be interesting to see to which degree our predictions of a CDW can be confirmed experimentally. Although there are no experimental results published yet, we know of several experimental groups interested in devising experiments to find CDWs in type-II Weyl semimetals.

Until now it seems that all type-II Weyl materials showing (nearly) unsaturated magnetoresistance, e.g. WTe_2 and WP_2, indeed have perfectly compensated electron and hole pockets. The question how magnetoresistance evolves in the interacting but non-compensated case remains interesting and is left for future research.

A. Wave function matching

We calculate ballistic transport in a scattering region of length L and width W as described in the main text. The Hamiltonian is given by

$$H = \sum_{ij} v_{ij} k_i \sigma_j + (a_i k_i - u)\sigma_0 \,. \tag{A.1}$$

The $a_i k_i$ terms can be interpreted as a tilt of the cone and v_{ij} as a $d \times d$ matrix describing the anisotropy of the dispersion, where it is sufficient to have nonzero entries on the upper triangular to describe all possible anisotropies of a cone. The dispersion is given by

$$\begin{aligned} \epsilon_{1,2}(k) &= -u + a_x k_x + a_y k_y + a_z k_z \\ &\pm \sqrt{k_x^2(v_{xx}^2 + v_{xy}^2 + v_{xz}^2) + 2k_x(k_y(v_{xy}v_{yy} + v_{xz}v_{yz}) + k_z v_{xz} v_{zz}) + k_y^2(v_{yy}^2 + v_{yz}^2) + 2k_y k_z v_{yz} v_{zz} + k_z^2 v_{zz}^2} \,. \end{aligned} \tag{A.2}$$

Whenever the above square-root expression occurs we will abbreviate it as $\sqrt{\cdots}$. Then the spinors are

$$\chi_{1,2} = \begin{pmatrix} -\dfrac{k_x v_{xx} - i\,(k_x v_{xy} + k_y v_{yy})}{k_x v_{xz} + k_y v_{yz} + k_z v_{zz} \mp \sqrt{\cdots}} \\ 1 \end{pmatrix} \tag{A.3}$$

and the velocities used to normalize incoming and outgoing plane waves are $v(k) = \partial_k \epsilon(k)$. We consider the limit of highly doped leads ($u \to \infty$) in $u = 0$ in the scattering region. The transverse momentum $k_\perp = k_y$ ($d = 2$) and $k_\perp = (k_y, k_z)$ ($d = 3$) is quantized due to the finite width W,

$$k_y = \frac{2\pi n}{W} \qquad\qquad k_z = \frac{2\pi m}{W} \,. \tag{A.4}$$

For any mode of given momentum k_y, k_z we determine the x component of the wave vectors k_{in}, k_r, k_t of the incoming, reflected, and transmitted wave and the x component in the scattering region $\tilde{k}_{1,2}$ by solving Eq. (A.2) for $\epsilon(k) = 0$. Then we calculate the transmission and reflection amplitude by wave function matching at the beginning and the end of the scattering region ($x = 0, L$):

$$\frac{1}{\sqrt{v_{\text{in}}}}\chi_{\text{in}} + \frac{r}{\sqrt{v_r}}\chi_r = \alpha\chi_1 + \beta\chi_2 \,, \tag{A.5}$$

$$\frac{t}{\sqrt{v_t}}\chi_t = \alpha\chi_1 \exp^{i\tilde{k}_1 L} + \beta\chi_2 \exp^{i\tilde{k}_2 L} \,. \tag{A.6}$$

The total transmission probability can be obtained by summing over all modes:

$$T = \sum_{k_\perp} |t(k_\perp)|^2 \,. \tag{A.7}$$

In the limit $\frac{L}{W} \to 0$ one may replace the sum by an integral which gives Eq. (2.2) of the main text.

B. Numerical procedure SCBA

In this appendix we provide further details on the calculation of the density of states using the self-consistent Born approximation (SCBA), see Section 3.3. Since there is rotational symmetry around the tilt direction (the z axis), the parameter dependence of the self-energy $\Sigma(\mathbf{k},\varepsilon)$ can be restricted, and $\Sigma(\mathbf{k},\varepsilon)$ can be parameterized as

$$\begin{aligned}\Sigma(\mathbf{k},\varepsilon) =& \Sigma_0(k,\theta,\varepsilon)+\Sigma_3(k,\theta,\varepsilon)\sigma_3\\ &+\Sigma_\perp(k,\theta,\varepsilon)(\sigma_1\cos\varphi+\sigma_2\sin\varphi),\end{aligned} \tag{B.1}$$

where θ is the angle between $\mathbf{k}$ and the z axis and φ is the azimuthal angle corresponding to $\mathbf{k}$. Using the short-hand notations (with dependence on k, θ, and ε left implicit)

$$\begin{aligned}X &= \varepsilon - va\cos(\theta)k - \Sigma_0(k,\theta,\varepsilon),\\ X_\perp &= vk\sin\theta+\Sigma_\perp(k,\theta,\varepsilon),\\ X_3 &= vk\cos\theta+\Sigma_z(k,\theta,\varepsilon),\end{aligned} \tag{B.2}$$

we can write the self-consistency condition for the Green function and self-energy as

$$\begin{aligned}G =& \frac{1}{X^2-X_\perp^2-X_3^3}\\ &\times\left[X\sigma_0+X_\perp(\sigma_1\cos\varphi+\sigma_2\sin\varphi)+X_3\sigma_3\right],\end{aligned} \tag{B.3}$$

$$\Sigma_\mu = \frac{1}{(2\pi)^3}\int_0^\infty dk'\int_0^\pi d\theta' \frac{X'_\mu\sin\theta'}{X'^2-X'^2_\perp-X'^2_3}B_\mu(\mathbf{k}-\mathbf{k}'), \tag{B.4}$$

with $\mu = 0$, $\perp$, 3 and

$$\begin{aligned}B_0(\mathbf{k}-\mathbf{k}') &= K\int_0^{2\pi} d\varphi' e^{-|\mathbf{k}-\mathbf{k}'|^2\xi^2/2}\\ &= 2\pi K e^{-(k^2+k'^2-2kk'\cos(\theta)\cos(\theta'))\xi^2/2}\\ &\quad\times I_0(2kk'\xi^2\sin\theta\sin\theta'),\end{aligned} \tag{B.5}$$

$$\begin{aligned}B_\perp(\mathbf{k}-\mathbf{k}') =& K\int_0^{2\pi} d\varphi' e^{-|\mathbf{k}-\mathbf{k}'|^2\xi^2/2}e^{-i\varphi}\\ &= 2\pi K e^{-(k^2+k'^2-2kk'\cos(\theta)\cos(\theta'))\xi^2/2}\\ &\quad\times I_1(2kk'\xi^2\sin\theta\sin\theta'),\end{aligned} \tag{B.6}$$

$$B_3(\mathbf{k}-\mathbf{k}') = B_0(\mathbf{k}-\mathbf{k}'), \tag{B.7}$$

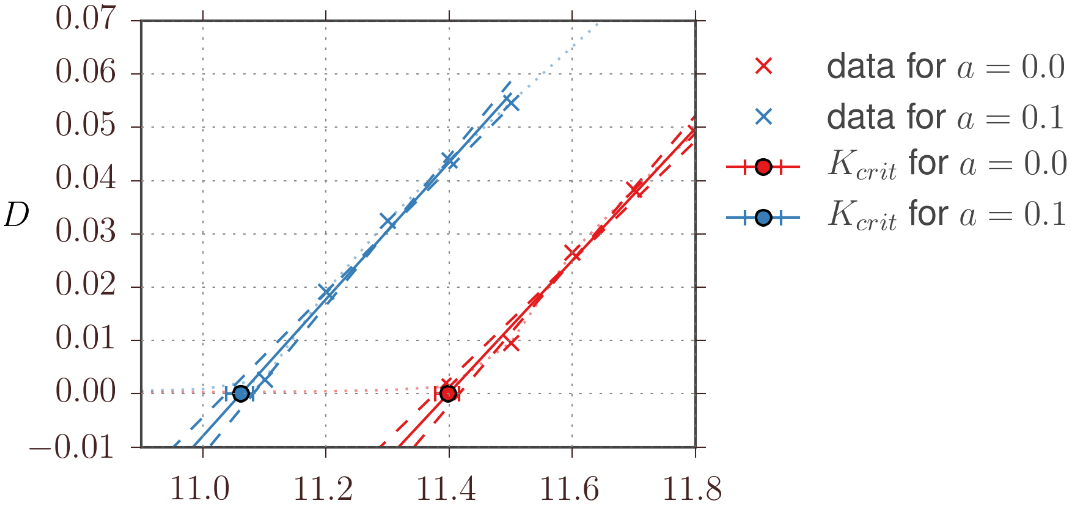

Figure B.1.: Linear fit to D in the region where $D > D_{\text{threshold}}$ to determine K_c.

where I_0 and I_1 are modified Bessel functions. Self-consistency equations for X_0, $X_\perp$, and X_3 then immediately follow from the definitions (B.2).

For the numerical computation we have to compute G at small but finite imaginary values for the energy ε. Combined with the need to use a finite grid in momentum energy space to perform the integrations this leads to a slight rounding of the onset of a finite density of states upon entering the diffusive phase from the weak-disorder regime. This obstructs a direct determination of the critical disorder strength from the density-of-states calculations in the SCBA. We have estimated the precise location of the critical disorder strength from a linear fit of density of states for disorder strengths just above the critical disorder strength. An example of such a linear fit is shown in Fig. B.1. The fitting procedure leaves a small residual error for the value of K_c, which is shown by the error bars in Fig. 3.2.

C. Derivations for “Charge density wave instabilities of type-II Weyl semimetals in a strong magnetic field”

C.1. Susceptibility predictions for Q_{CDW}

We use the standard formula to compute the susceptibility[GLS04]

$$\Pi_{nn'}^{\lambda\lambda'}(\mathbf{q},\omega) = \lim_{\delta\to 0}\sum_{\mathbf{q}'} \frac{n_F\left(E_\lambda(\mathbf{q}',n)\right) - n_F\left(E_{\lambda'}\left(\mathbf{q}'+\mathbf{q},n'\right)\right)}{E_\lambda(\mathbf{q}',n) - E_{\lambda'}(\mathbf{q}'+\mathbf{q},n') + \omega + i\delta} \tag{C.1}$$

using the Fermi function n_F, which depends on temperature, Π is shown for some representative parameters in Fig. C.1. In the right panel of this figure we show that q corresponding to the highest peak in susceptibility is indeed the optimal Q_{CDW} (lowest critical interaction strength) for the charge density wave.

C.2. Landau level spectrum and interaction

As discussed in the main text, the magnetic field $\mathbf{B} = \nabla\times\mathbf{A}$ is introduced by a minimal coupling of the vector potential, which we consider to be $\mathbf{A} = (0, Bx, 0)$ in the Landau gauge, to the crystal momentum $\mathbf{\Pi} = \hbar\mathbf{k} - \frac{e}{c}\mathbf{A}$. Then we obtain the standard raising and lowering operators $a = \frac{l_B}{\sqrt{2}\hbar}\left(\Pi_x - i\Pi_y\right)$ and $a^\dagger = \frac{l_B}{\sqrt{2}\hbar}\left(\Pi_x + i\Pi_y\right)$ with $[a, a^\dagger] = 1$. And consequently we arrive at the following Hamiltonian describing the low energy theory

$$H_0 = \int \mathrm{d}^3r \left(\Psi_A^\dagger(\mathbf{r}) \quad \Psi_B^\dagger(\mathbf{r})\right) \begin{pmatrix} (1-\eta)k_z + (\gamma+\beta)k_z^3 & \frac{\sqrt{2}}{l_B}\hat{a}^\dagger \\ \frac{\sqrt{2}}{l_B}\hat{a} & -(1+\eta)k_z + (\gamma-\beta)k_z^3 \end{pmatrix} \begin{pmatrix} \Psi_A(\mathbf{r}) \\ \Psi_B(\mathbf{r}) \end{pmatrix} \tag{C.2}$$

with

$$\Psi_A^\dagger(\mathbf{r}) = \sum_{n,p,k_z} e^{ik_z z}\psi_{n,p}(x,y)\hat{c}_{A,n,p,k_z} \tag{C.3}$$

$$\psi_{n,p}(x,y) = \frac{1}{\sqrt{L}} e^{ipx}\left(\pi 2^{2n}(n!)^2\right)^{-1/4} e^{-\frac{1}{2}(y+p)^2} H_n(y+p) \tag{C.4}$$

while for B there is a shift from n to $n-1$

$$\Psi_B^\dagger(\mathbf{r}) = \sum_{n,p,k_z} e^{ik_z z}\psi_{n-1,p}(x,y)\hat{c}_{B,n,p,k_z} \tag{C.5}$$

where ψ are properly normalized Harmonic oscillator wave functions including the Hermite polynomials H_n.

The generic interaction is given by

$$H_{\text{int}} = \frac{1}{2} \sum_{\alpha,\beta=A,B} \int \mathrm{d}^3\mathbf{r}_1 \int \mathrm{d}^3\mathbf{r}_2 \Psi^\dagger_\alpha(\mathbf{r}_1)\Psi^\dagger_\beta(\mathbf{r}_2) U(\mathbf{r}_1-\mathbf{r}_2)\Psi_\beta(\mathbf{r}_2)\Psi_\alpha(\mathbf{r}_1) \tag{C.6}$$

where the contact interaction corresponds to the interaction potential $U(\mathbf{r}) = \delta(\mathbf{r})$. Note, in using the contact interaction we avoid introducing another scale, but we checked that the qualitative findings presented in the following can be reproduced using longer ranged interactions including Coulomb.

Projecting this contact interaction onto the Landau levels we obtain Eq. 7 in the main text with

$$\begin{aligned} H_{\text{int}} &= \frac{1}{2} \sum_{\substack{n_1,n_2,n_3,n_4,\\ p_1,p_2,k_z,k'_z,\\ q_x,q_y,q_z}} e^{iq_y(p_1-p_2-q_x)} M_{n_1,n_2,n_3,n_4}(\mathbf{q}) \\ &\quad \cdot \sum_{\alpha,\beta=A,B} c^\dagger_{\alpha,n_1,p_1,k_z} c^\dagger_{\beta,n_2,p_2,k'_z} c_{\beta,n_3,p_2+q_x,k'_z+q_z} c_{\alpha,n_4,p_1-q_x,k_z-q_z} \end{aligned} \tag{C.7}$$

$$M_{n_1,n_2,n_3,n_4}(\mathbf{q}) = U(\mathbf{q}) \underbrace{J_{n_4,n_1}(q_x,q_y) J_{n_3,n_2}(-q_x,-q_y)}_{F(q_x,q_y)} \tag{C.8}$$

with $c_{\alpha=B,n} \to c_{B,n+1}$, the Fourier transformed interaction potential $U(\mathbf{q})$ and the factor F due to the wave functions overlap. Here all in-plane momenta are measured in units of l_B. Using the wave functions from Eq. (C.5) we get for J [BR83]

$$J_{m,n}(q_x,q_y) = \sqrt{\frac{n!}{m!}} e^{-|q|^2/4} \left(\frac{q_x+iq_y}{\sqrt{2}}\right)^{m-n} L_n^{m-n}\left(\frac{|q|^2}{2}\right) \quad \text{with } |q|^2 = q_x^2+q_y^2 \quad \text{for } \ m<n \tag{C.9}$$

$$J_{m,n}(q_x,q_y) = J^*_{n,m}(-q_x,-q_y)\,. \tag{C.10}$$

The full Hamiltonian then reads

$$H = H_0 + H_{int}\,. \tag{C.11}$$

C.3. Density wave order parameter

The intra LL branch components

$$\langle a^\dagger_{p,k_z} a_{p-q_x,k_z-q_z}\rangle = n_a(k_z) e^{-ipQ_y} e^{iQ_y q_x/2} \delta(q_x-Q_x)\delta(q_z) \tag{C.12}$$

$$\langle b^\dagger_{p,k_z} b_{p-q_x,k_z-q_z}\rangle = n_b(k_z) e^{-ipQ_y} e^{iQ_y q_x/2} \delta(q_x-Q_x)\delta(q_z) \tag{C.13}$$

only shift the chemical potential which can be fixed independently. To motivate the ansatz for our CDW order parameter, we show in the following explicitly that the resulting electron density is real and modulated in the form $\cos(Q_z \cdot r_z)$.

For now we look only at the density of the c_A part and we fix n and B so we do not write out dependencies on these variables:

$$\rho_A(\mathbf{r}) = \sum_{\mathbf{q}} e^{i\mathbf{q}\cdot\mathbf{r}} \rho_A(\mathbf{q}) \tag{C.14}$$

where

$$\rho_A(\mathbf{q}) = \sum_{p_1,k_z} e^{iq_y(p_1-q_x/2)} \langle c^\dagger_{A,p_1,k_z} c_{A,p_1-q_x,k_z-q_z}\rangle \tag{C.15}$$

so that

$$\begin{aligned}
\rho_A(\mathbf{r}) &= \sum_{\mathbf{q}} e^{i\mathbf{q}\cdot\mathbf{r}} \sum_{p_1,k_z} e^{iq_y(p_1-q_x/2)} \langle c^\dagger_{A,p_1,k_z} c_{A,p_1-q_x,k_z-q_z}\rangle && \text{(C.16)}\\
&= \sum_{\mathbf{q}} e^{i\mathbf{q}\cdot\mathbf{r}} \sum_{p_1,k_z} e^{iq_y(p_1-q_x/2)} \\
&\quad \langle (u(k_z)a^\dagger_{p_1,k_z} - v(k_z)b^\dagger_{p_1,k_z})(u(k_z-q_z)a_{p_1-q_x,k_z-q_z} - v(k_z-q_z)b_{p_1-q_x,k_z-q_z})\rangle && \text{(C.17)}\\
&= \sum_{\mathbf{q}} e^{i\mathbf{q}\cdot\mathbf{r}} \sum_{p_1,k_z} e^{iq_y(p_1-q_x/2)} \Big(u(k_z)u(k_z-q_z)\langle a^\dagger_{p_1,k_z} a_{p_1-q_x,k_z-q_z}\rangle && \text{(C.18)}\\
&\quad + v(k_z)v(k_z-q_z)\langle b^\dagger_{p_1,k_z} b_{p_1-q_x,k_z-q_z}\rangle && \text{(C.19)}\\
&\quad + u(k_z)v(k_z-q_z)\langle a^\dagger_{p_1,k_z} b_{p_1-q_x,k_z-q_z}\rangle && \text{(C.20)}\\
&\quad + v(k_z)u(k_z-q_z)\langle b^\dagger_{p_1,k_z} a_{p_1-q_x,k_z-q_z}\rangle \Big) && \text{(C.21)}
\end{aligned}$$

where the first two summands, Eqs. (C.18) and (C.19), are just given by

$$\sum_{k_z} u(k_z)^2 n_A(k_z) + v(k_z)^2 n_B(k_z)\,. \tag{C.22}$$

So we consider the second part in detail, Eqs. (C.20) and (C.21), using the ansatz from above. We obtain the corresponding $\langle b^\dagger a\rangle$ terms by shifting variables:

$$\begin{aligned}
&\sum_{\mathbf{q}} e^{i\mathbf{q}\cdot\mathbf{r}} \sum_{p_1,k_z} e^{iq_y(p_1-q_x/2)} \Big(u(k_z)v(k_z-q_z)\Delta(k_z,\mathbf{Q}) e^{-ip_1Q_y} e^{iQ_yq_x/2} \delta(q_x-Q_x)\delta(q_z-Q_z) \\
&\qquad + v(k_z)u(k_z-q_z)\Delta^*(k_z+q_z,\mathbf{Q}) e^{ip_1Q_y} e^{-iQ_yq_x/2} \delta(q_x+Q_x)\delta(q_z+Q_z)\Big)
\end{aligned} \tag{C.23}$$

then $\sum_{p_1} e^{ip_1(q_y \pm Q_y)}$ gives a $\delta(q_y \pm Q_y)$, such that

$$\begin{aligned}= \sum_{\mathbf{q}} e^{i\mathbf{q}\cdot\mathbf{r}} \sum_{k_z} e^{-iq_y q_x/2} \Big(& u(k_z)v(k_z - q_z)\Delta(k_z, \mathbf{Q}) e^{iQ_y q_x/2} \delta(q_x - Q_x)\delta(q_y - Q_y)\delta(q_z - Q_z) \\ & + v(k_z)u(k_z - q_z)\Delta^*(k_z - q_z, \mathbf{Q}) e^{-iQ_y q_x/2} \delta(q_x + Q_x)\delta(q_y + Q_y)\delta(q_z + Q_z) \Big), \end{aligned} \tag{C.24}$$

making use of all the delta functions and using $\mathbf{Q} = (Q_x, Q_y, Q_z)$ we get

$$\begin{aligned}= \sum_{k_z} \Big(& e^{i\mathbf{Q}\cdot\mathbf{r}} u(k_z)v(k_z - Q_z)\Delta(k_z, \mathbf{Q}) \\ & + e^{-i\mathbf{Q}\cdot\mathbf{r}} v(k_z)u(k_z + Q_z)\Delta^*(k_z + Q_z, \mathbf{Q}) \Big). \end{aligned} \tag{C.25}$$

Now we shift the k_z of the second summand to $k_z \to k_z - Q_z$, as the summation over k_z goes from $-\infty$ to $+\infty$ and $\lim_{k_z \to \pm\infty} v(k_z) = 0$ this poses no problems. Finally we get

$$\rho_A(\mathbf{r}) = \sum_{k_z} u(k_z)v(k_z - Q_z)\Big(e^{i\mathbf{Q}\cdot\mathbf{r}} \Delta(k_z, \mathbf{Q}) + e^{-i\mathbf{Q}\cdot\mathbf{r}} \Delta^*(k_z, \mathbf{Q}) \Big) \tag{C.26}$$

which is manifestly real.

C.4. Fock term

In the mean field expansion we need to pay special attention to the Fock terms and we use a trick from [GLS04]. Starting from an exemplary Fock term in the mean field expansion

$$\sum_{\mathbf{q}, p_1, p_2, k_z, k_z'} e^{iq_y(p_1 - p_2 - q_x)} M(\mathbf{q}) \langle c^\dagger_{p_1, k_z} c_{p_2 + q_x, k_z' - q_z} \rangle c^\dagger_{p_2, k_z'} c_{p_1 - q_x, k_z - q_z} \tag{C.27}$$

following the steps of [GLS04] we arrive at

$$= \sum_{p_x, p_y, s_z,} \frac{1}{N_B} \sum_{q_x, q_y} e^{i(q_y p_x - p_y q_x)} M(\mathbf{q}) \sum_{y_+, y_-} e^{ip_y(y_+ - y_- - p_x)} \langle c^\dagger_{y_+, k_z} c_{y_+ - p_x, k_z - s_z} \rangle c^\dagger_{y_-, k_z'} c_{y_- + p_x, k_z' + s_z} \tag{C.28}$$

where we used the replacements $p_x = p_1 - p_2 - q_x$, $\quad R = \frac{p_1 + p_2}{2}$, $\quad y_\pm = R \pm \left(\frac{q_x + p_x}{2}\right)$ and inserting the clever 1, N_B being the number of states in the Landau level:

The indices A, B of the c operators are not specified here, but the order of the operators stays fixed.

Renaming variables as $y_+ \to p_1, y_- \to p_2, s_z \to q_z, p_x \leftrightarrow q_x, p_y \leftrightarrow q_y$ we get

$$\sum_{\mathbf{q}, p_1, p_2, k_z, k_z'} e^{iq_y(p_1 - p_2 - q_x)} \tilde{M}(\mathbf{q}) \langle c^\dagger_{p_1, k_z} c_{p_1 - q_x, k_z - q_z} \rangle c^\dagger_{p_2, k_z'} c_{p_2 + q_x, k_z' + q_z}, \tag{C.29}$$

where

$$\tilde{M}(\mathbf{q}) = \frac{1}{N_B} \sum_{p_x, p_y} e^{i(p_y q_x - p_x q_y)} M(\mathbf{p}) \tag{C.30}$$

which is (up to a rotation) the Fourier transform of $M(\mathbf{q})$ in the q_x, q_y plane.

C.5. Projected mean-field matrix elements

We start with the interaction matrix from above for the Hartree terms, and use (C.30) for the Fock terms to get the matrix elements in the c-basis. First we write the Hamiltonian (C.11) as a matrix:

$$H = \begin{pmatrix} c^\dagger_{A,p_1,k_z} c^\dagger_{A,p_2,k'_z} & c^\dagger_{A,p_1,k_z} c^\dagger_{B,p_2,k'_z} & c^\dagger_{B,p_1,k_z} c^\dagger_{A,p_2,k'_z} & c^\dagger_{B,p_1,k_z} c^\dagger_{B,p_2,k'_z} \end{pmatrix} H_c \begin{pmatrix} c_{A,p_2+q_x,k'_z+q_z} c_{A,p_1-q_x,k_z-q_z} \\ c_{A,p_2+q_x,k'_z+q_z} c_{B,p_1-q_x,k_z-q_z} \\ c_{B,p_2+q_x,k'_z+q_z} c_{A,p_1-q_x,k_z-q_z} \\ c_{B,p_2+q_x,k'_z+q_z} c_{B,p_1-q_x,k_z-q_z} \end{pmatrix} \tag{C.31}$$

$$= \begin{pmatrix} a^\dagger_{p_1,k_z} a^\dagger_{p_2,k'_z} & a^\dagger_{p_1,k_z} b^\dagger_{p_2,k'_z} & b^\dagger_{p_1,k_z} a^\dagger_{p_2,k'_z} & b^\dagger_{p_1,k_z} b^\dagger_{p_2,k'_z} \end{pmatrix} H_a \begin{pmatrix} a_{p_2+q_x,k'_z+q_z} a_{p_1-q_x,k_z-q_z} \\ a_{p_2+q_x,k'_z+q_z} b_{p_1-q_x,k_z-q_z} \\ b_{p_2+q_x,k'_z+q_z} a_{p_1-q_x,k_z-q_z} \\ b_{p_2+q_x,k'_z+q_z} b_{p_1-q_x,k_z-q_z} \end{pmatrix} \tag{C.32}$$

with

$$H_a = U_4(k_z, k'_z)\, H_c\, U_4^T(k'_z + q_z, k_z - q_z) \tag{C.33}$$

where

$$U_4(k_1, k_2) = U(k_1, B) \otimes U(k_2, B) \tag{C.34}$$

To obtain the matrix elements P used in the mean-field Hamiltonian in the main text, we write each of the 16 terms of this Hamiltonian in a mean field expansion and collect the terms with the corresponding operators including necessary shifts of variables to write it in the basis of a_{k_z}.

C.6. CDW contribution to the heat capacity C_V

The formation of the CDW leads to the usual thermodynamic signatures around T_c. This is shown explicitly in the inset of Fig. 3 where we have calculated the heat capacity for the model with and without the CDW via

$$C_V^\alpha \propto -\frac{\partial U_\alpha}{\partial T} \text{ with } U_\alpha = N_B \sum_i E_i^\alpha n_F(E_i^\alpha) \tag{C.35}$$

where E_i^α with $\alpha =$CDW ($\alpha = 0$) are the energy levels with (without) the CDW formation and the multi-label i refers to the LL index, the momentum k_z and the electron- and hole-like band index.

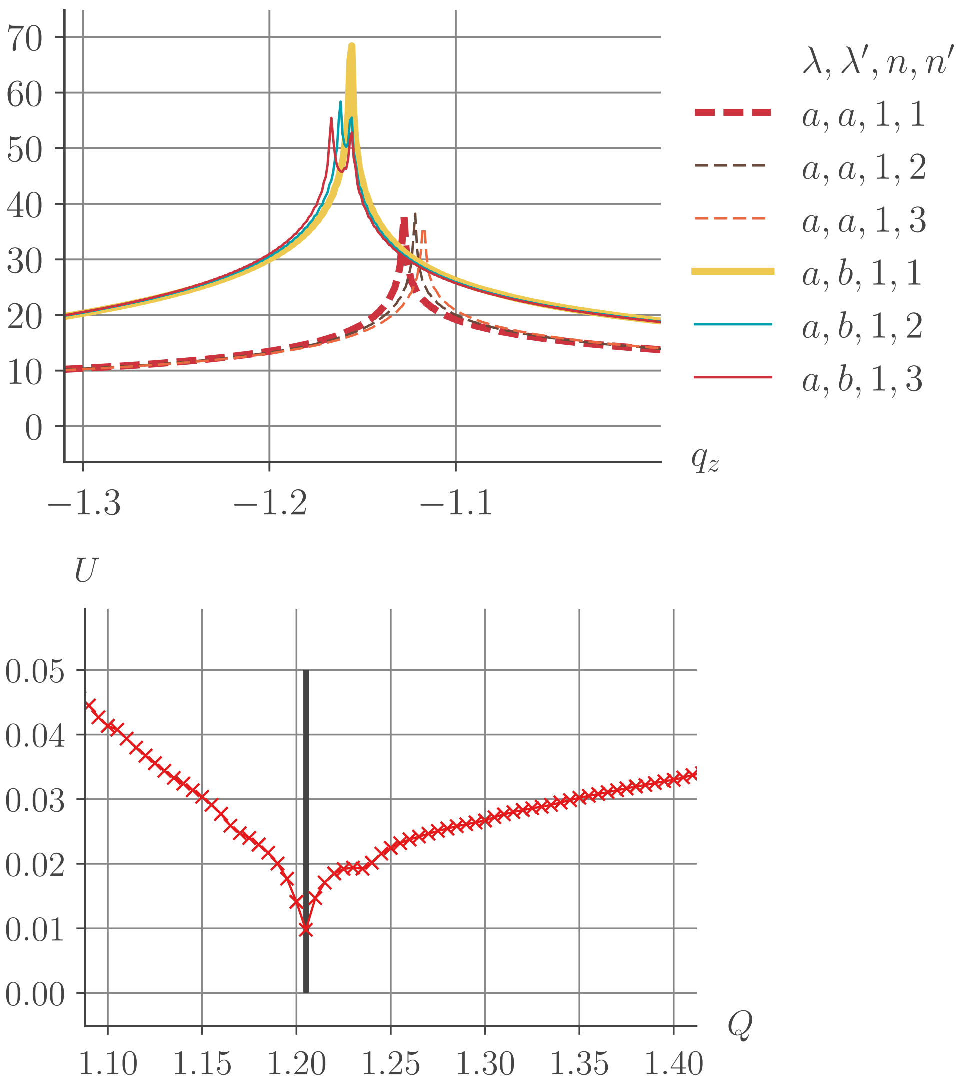

Figure C.1.: Top panel: Susceptibility (arbitrary units) in the non-interacting case with parameters at $B = 20\text{T}$, $T = 0.46\text{K}$, $\omega = 0$. The maximal susceptibility is reached for $\lambda = a, \lambda' = b$ and $n = n'$. Bottom panel: Critical interaction strength in dependence of CDW wavevector Q for a single Landau level $(n = 1, B = 10)$. The solid vertical line corresponds to the prediction from the susceptibility calculation.

D. Mean-field matrix elements simplifications

After the publication of [Tre+17a] we gained some more insight in the structure of the interaction matrix elements, also generalizing to arbitrary combinations of Landau level indices $n_{1,2,3,4}$, as defined in chapter 4 and C.2. Recall the matrix elements formula

$$M_{n_1,n_2,n_3,n_4}(\mathbf{q}) = U(\mathbf{q})\, \underbrace{J_{n_4,n_1}(q_x, q_y) J_{n_3,n_2}(-q_x, -q_y)}_{F(q_x,q_y)} \tag{D.1}$$

$$J_{m,n}(q_x, q_y) = \sqrt{\frac{n!}{m!}} e^{-|q|^2/4} \left(\frac{q_x + iq_y}{\sqrt{2}}\right)^{m-n} L_n^{m-n}\left(\frac{|q|^2}{2}\right) \quad \text{with } |q|^2 = q_x^2 + q_y^2 \quad \text{for} \;\; m < n \tag{D.2}$$

$$J_{m,n}\left(q_x, q_y\right) = J^*_{n,m}\left(-q_x, -q_y\right), \tag{D.3}$$

that we want to evaluate at finite k_z but $q_x = q_y = 0$. The following analytic results are obtained in the basis of the c_A, c_B operators, therefore a basis transformation introducing a dependence on n, k_z and B needs still to be applied.

D.1. Hartree terms

In $J_{m,n}$ there appears a factor of $(q_x \pm iq_y)^{m-n}$, as the matrix elements for the Hartree terms are evaluated at $q_x = q_y = 0$, this factor cancels any contribution for $m \neq n$ and the only contribution is for $m = n$, giving a factor of 1, as $L_n^0(0) = 1$. Due to the shift of $c_{\alpha=B,n} \to c_{B,n+1}$, the factor J corresponding to c_{B,n_i} depends on $n_i - 1$, leading to the full interaction matrix:

$$\begin{bmatrix} \delta_{n_1 n_4}\delta_{n_2 n_3} & \delta_{n_1,n_4-1}\delta_{n_2 n_3} & \delta_{n_1 n_4}\delta_{n_2,n_3-1} & \delta_{n_1,n_4-1}\delta_{n_2,n_3-1} \\ \delta_{n_1 n_4}\delta_{n_3,n_2-1} & \delta_{n_1,n_4-1}\delta_{n_3,n_2-1} & \delta_{n_1 n_4}\delta_{n_2-1,n_3-1} & \delta_{n_1,n_4-1}\delta_{n_2-1,n_3-1} \\ \delta_{n_2 n_3}\delta_{n_4,n_1-1} & \delta_{n_2 n_3}\delta_{n_1-1,n_4-1} & \delta_{n_2,n_3-1}\delta_{n_4,n_1-1} & \delta_{n_2,n_3-1}\delta_{n_1-1,n_4-1} \\ \delta_{n_3,n_2-1}\delta_{n_4,n_1-1} & \delta_{n_3,n_2-1}\delta_{n_1-1,n_4-1} & \delta_{n_4,n_1-1}\delta_{n_2-1,n_3-1} & \delta_{n_1-1,n_4-1}\delta_{n_2-1,n_3-1} \end{bmatrix} \tag{D.4}$$

D.2. Fock terms

To calculate the Fock terms of the mean-field expansion we can use the rewriting introduced in chapter C.4. Therefore we are interested in $\tilde{M}(\mathbf{q})$ at $\mathbf{q} = 0$, which turns out to be the integral over q_x, q_y of the M Introducing the complex variable $z = q_x + iq_y$ this integral is equivalent to the integral over the complex plane, and the argument of the Laguerre polynomials becomes $|z|^2$. For each factor of J in the matrix element we get z^α with $\alpha = m - n$ being the second index of the associated Laguerre polynomial. Further we distinguish $\alpha = n_4 - n_1$ and $\alpha' = n_3 - n_2$ and we use the polar notation $z = re^{i\varphi}$. Note that negative α corresponds to exchanging the two indices of the Laguerre polynomial and additionally introduces a complex conjugation. Now two cases can occur:

1. $\alpha = -\alpha'$: this leads to an integral of the form

   $$\int_C \mathrm{d}z z^\alpha z^{*-\alpha} L_n^\alpha L_{n'}^\alpha e^{-z^2} = \int_C \mathrm{d}z |z|^{2\alpha} L_n^\alpha L_{n'}^\alpha e^{-|z|^2} \tag{D.5}$$

   which is exactly the orthogonality relation of the associated Laguerre polynomials, leading to $\delta_{n,n'}$, with $n = \max n1, n4$ and $n' = \max n2, n3$ with the appropriate ± 1 shift for the B operators.

2. $\alpha \neq -\alpha'$: We introduce β as $\alpha' = -\alpha - \beta$ and manifestly nonzero β The integrand now includes a factor of $|z|^{2\alpha} z^\beta$ (or $z^{*\beta}$). The part $|z|^{2\alpha} L_n^\alpha L_{n'}^\alpha e^{-|z|^2}$ of the integrand only depends on $|z|$, i.e. is independent of the complex phase, and consequently the integral over the complex plane can be split into integrations over r and φ, and the integration $\int \mathrm{d}\varphi z^n$ is 0. As a negative value of α always is related to the complex conjugate of J with positive α, this case rules out any contribution of elements where the product of two Laguerre polynomials with different α indices occurs.

Together this leads to the following matrix elements of $\tilde{M}$ (wrapping the 4×4 matrix to two lines):

$$\left[\begin{matrix}
\delta_{-n_1+n_4,n_2-n_3}\delta_{\max(n_1,n_4),\max(n_2,n_3)} & \delta_{n_2-n_3,-n_1+n_4-1}\delta_{\max(n_1,n_4-1),\max(n_2,n_3)} \\
\delta_{-n_1+n_4,n_2-n_3-1}\delta_{\max(n_1,n_4),\max(n_3,n_2-1)} & \delta_{-n_1+n_4-1,n_2-n_3-1}\delta_{\max(n_1,n_4-1),\max(n_3,n_2-1)} \\
\delta_{n_2-n_3,-n_1+n_4+1}\delta_{\max(n_2,n_3),\max(n_4,n_1-1)} & \delta_{-n_1+n_4,n_2-n_3}\delta_{\max(n_2,n_3),\max(n_1-1,n_4-1)} \\
\delta_{-n_1+n_4+1,n_2-n_3-1}\delta_{\max(n_3,n_2-1),\max(n_4,n_1-1)} & \delta_{-n_1+n_4,n_2-n_3-1}\delta_{\max(n_3,n_2-1),\max(n_1-1,n_4-1)}
\end{matrix}\right.$$

$$\left.\begin{matrix}
\delta_{-n_1+n_4,n_2-n_3+1}\delta_{\max(n_1,n_4),\max(n_2,n_3-1)} & \delta_{-n_1+n_4-1,n_2-n_3+1}\delta_{\max(n_1,n_4-1),\max(n_2,n_3-1)} \\
\delta_{-n_1+n_4,n_2-n_3}\delta_{\max(n_1,n_4),\max(n_2-1,n_3-1)} & \delta_{n_2-n_3,-n_1+n_4-1}\delta_{\max(n_1,n_4-1),\max(n_2-1,n_3-1)} \\
\delta_{-n_1+n_4+1,n_2-n_3+1}\delta_{\max(n_2,n_3-1),\max(n_4,n_1-1)} & \delta_{-n_1+n_4,n_2-n_3+1}\delta_{\max(n_2,n_3-1),\max(n_1-1,n_4-1)} \\
\delta_{n_2-n_3,-n_1+n_4+1}\delta_{\max(n_4,n_1-1),\max(n_2-1,n_3-1)} & \delta_{-n_1+n_4,n_2-n_3}\delta_{\max(n_1-1,n_4-1),\max(n_2-1,n_3-1)}
\end{matrix}\right] \tag{D.6}$$

In most of the cases n_1 has to be equal (up to ±1) to n_3, while it is independent of n_2, n_4, which in turn are equal up to ±1 as well. This is comparable to the situation of the Hartree results were n_1, n_4 were independent of n_2, n_3, but here with switched pairs. One can easily verify this when n_1, n_3 are much larger (or smaller) than n_2, n_4, as the terms $\delta_{\max(n_1,n_4),\max(n_2,n_3)}$ then can be simplified, regardless of some ±1.

E. Bibliography

[Ali+14] M. N. Ali, J. Xiong, S. Flynn, J. Tao, Q. D. Gibson, L. M. Schoop, T. Liang, N. Haldolaarachchige, M. Hirschberger, N. P. Ong, and R. Cava. “Large, non-saturating magnetoresistance in WTe2”. In: *Nature* 514 (Sept. 2014), pp. 205–208. ISSN: 1476-4687. URL: `http://dx.doi.org/10.1038/nature13763`.

[AM07] E. Akkermans and G. Montambaux. *Mesoscopic Physics of Electrons and Photons*. Cambridge University Press, 2007. URL: `https://doi.org/10.1017/cbo9780511618833`.

[AM76] N. W. Ashcroft and N. Mermin. *Solid State Physics*. Holt, Rinehart and Winston, 1976.

[AS10] A. Altland and B. D. Simons. *Condensed Matter Field Theory*. Englisch. 2nd ed. Cambridge ; New York: Cambridge University Press, 2010. ISBN: 978-0-521-76975-4.

[Aut+16] G. Autés, D. Gresch, M. Troyer, A. A. Soluyanov, and O. V. Yazyev. “Robust Type-II Weyl Semimetal Phase in Transition Metal Diphosphides $X\mathrm{P}_2$ (X = Mo, W)”. In: *Phys. Rev. Lett.* 117 (6 Aug. 2016), p. 066402. URL: `https://link.aps.org/doi/10.1103/PhysRevLett.117.066402`.

[Bai+14] P. Baireuther, J. M. Edge, I. C. Fulga, C. W. J. Beenakker, and J. Tworzydło. “Quantum phase transitions of a disordered antiferromagnetic topological insulator”. In: *Phys. Rev. B* 89.3 (2014), p. 035410. URL: `http://link.aps.org/doi/10.1103/PhysRevB.89.035410`.

[Bar+07] J. H. Bardarson, J. Tworzydło, P. W. Brouwer, and C. W. J. Beenakker. “One-Parameter Scaling at the Dirac Point in Graphene”. In: *Phys. Rev. Lett.* 99.10 (Sept. 2007), p. 106801. URL: `https://journals.aps.org/prl/abstract/10.1103/PhysRevLett.99.106801`.

[Bau+15] Y. Baum, E. Berg, S. A. Parameswaran, and A. Stern. “Current at a Distance and Resonant Transparency in Weyl Semimetals”. In: *Phys. Rev. X* 5 (4 Dec. 2015), p. 041046. URL: `https://link.aps.org/doi/10.1103/PhysRevX.5.041046`.

[BB11] A. A. Burkov and L. Balents. “Weyl Semimetal in a Topological Insulator Multilayer”. In: *Phys. Rev. Lett.* 107.12 (2011), p. 127205. URL: `http://link.aps.org/doi/10.1103/PhysRevLett.107.127205`.

[BB92] C. Beenakker and M. Büttiker. "Suppression of shot noise in metallic diffusive conductors". In: *Phys. Rev. B* 46.3 (July 15, 1992), pp. 1889–1892. URL: `http://link.aps.org/doi/10.1103/PhysRevB.46.1889`.

[Bee15] C. Beenakker. "Tipping the Weyl Cone". In: *Journal Club for Condensed Matter Physics* August 2015 (2015). URL: `http://www.condmatjournalclub.org/?p=2644`.

[Bel+16a] I. Belopolski, D. S. Sanchez, Y. Ishida, X. Pan, P. Yu, S.-Y. Xu, G. Chang, T.-R. Chang, H. Zheng, N. Alidoust, G. Bian, M. Neupane, S.-M. Huang, C.-C. Lee, Y. Song, H. Bu, G. Wang, S. Li, G. Eda, H.-T. Jeng, T. Kondo, H. Lin, Z. Liu, F. Song, S. Shin, and M. Z. Hasan. "Discovery of a new type of topological Weyl fermion semimetal state in MoxW1-xTe2". In: *Nature Communications* 7 (Dec. 2016), p. 13643. URL: `https://doi.org/10.1038/ncomms13643`.

[Bel+16b] I. Belopolski, S.-Y. Xu, Y. Ishida, X. Pan, P. Yu, D. S. Sanchez, H. Zheng, M. Neupane, N. Alidoust, G. Chang, T.-R. Chang, Y. Wu, G. Bian, S.-M. Huang, C.-C. Lee, D. Mou, L. Huang, Y. Song, B. Wang, G. Wang, Y.-W. Yeh, N. Yao, J. E. Rault, P. Le Fèvre, F. Bertran, H.-T. Jeng, T. Kondo, A. Kaminski, H. Lin, Z. Liu, F. Song, S. Shin, and M. Z. Hasan. "Fermi arc electronic structure and Chern numbers in the type-II Weyl semimetal candidate $\mathrm{Mo}_x\mathrm{W}_{1-x}\mathrm{Te}_2$". In: *Phys. Rev. B* 94 (8 Aug. 2016), p. 085127. URL: `https://link.aps.org/doi/10.1103/PhysRevB.94.085127`.

[Ber+07] B. A. Bernevig, T. L. Hughes, S. Raghu, and D. P. Arovas. "Theory of the Three-Dimensional Quantum Hall Effect in Graphite". In: *Phys. Rev. Lett.* 99 (14 Oct. 2007), p. 146804. URL: `https://link.aps.org/doi/10.1103/PhysRevLett.99.146804`.

[Ber+15] E. J. Bergholtz, Z. Liu, M. Trescher, R. Moessner, and M. Udagawa. "Topology and Interactions in a Frustrated Slab: Tuning from Weyl Semimetals to $\mathcal{C} > 1$ Fractional Chern Insulators". In: *Phys. Rev. Lett.* 114.1 (2015), p. 016806. URL: `http://link.aps.org/doi/10.1103/PhysRevLett.114.016806`.

[BF04] H. Bruus and K. Flensberg. *Many-Body Quantum Theory in Condensed Matter physics: an introduction.* Oxford University Press, Oxford, 2004.

[BH13] B. A. Bernevig and T. L. Hughes. *Topological Insulators and Topological Superconductors.* Princeton University Press, 2013.

[Bil16] S. Bilenky. "Neutrino oscillations: From a historical perspective to the present status". In: *Nuclear Physics B* 908 (2016). Neutrino Oscillations: Celebrating the Nobel Prize in Physics 2015, pp. 2–13. ISSN: 0550-3213. URL: `http://www.sciencedirect.com/science/article/pii/S0550321316000353`.

[BKS18] J. Behrends, F. K. Kunst, and B. Sbierski. “Transversal magnetotransport in Weyl semimetals: Exact numerical approach”. In: *Phys. Rev. B* 97 (6 Feb. 2018), p. 064203. URL: `https://link.aps.org/doi/10.1103/PhysRevB.97.064203`.

[BKW95] L. Balicas, G. Kriza, and F. I. B. Williams. “Sign Reversal of the Quantum Hall Number in $(TMTSF)_2PF_6$”. In: *Phys. Rev. Lett.* 75 (10 Sept. 1995), pp. 2000–2003. URL: `https://link.aps.org/doi/10.1103/PhysRevLett.75.2000`.

[BM94] H. Baranger and P. Mello. “Mesoscopic transport through chaotic cavities: A random S-matrix theory approach”. In: *Phys. Rev. Lett.* 73.1 (1994), pp. 142–145. URL: `http://link.aps.org/doi/10.1103/PhysRevLett.73.142`.

[Bor+15] S. Borisenko, D. Evtushinsky, Q. Gibson, A. Yaresko, T. Kim, M. N. Ali, B. Buechner, M. Hoesch, and R. J. Cava. “Time-reversal symmetry breaking Weyl state in YbMnBi2”. In: *arxiv:1507.04847v1* (2015). URL: `http://arxiv.org/abs/1507.04847v1`.

[BR83] Y. A. Bychkov and E. Rashba. “Two-dimensional electron-hole system in a strong magnetic field: biexcitons and charge-density waves”. In: *Zh. Eksp. Teor. Fiz.* 85 (1983), pp. 1826–1846.

[BS84] M. V. Berry and F. R. S. “Quantal phase factors accompanying adiabatic changes”. In: *Proceedings of the Royal Society of London A: Mathematical, Physical and Engineering Sciences* 392.1802 (1984), pp. 45–57. ISSN: 0080-4630. URL: `http://rspa.royalsocietypublishing.org/content/392/1802/45`.

[Bur15] A. A. Burkov. “Negative longitudinal magnetoresistance in Dirac and Weyl metals”. In: *Phys. Rev. B* 91.24 (24 June 2015), p. 245157. ISSN: 1550-235X. URL: `http://dx.doi.org/10.1103/PhysRevB.91.245157`.

[Büt88] M. Büttiker. “Symmetry of electrical conduction”. In: *IBM Journal of Research and Development* 32.3 (June 1988), pp. 317–334. URL: `http://ieeexplore.ieee.org/document/5390001/`.

[Büt90] M. Büttiker. “Scattering theory of thermal and excess noise in open conductors”. In: *Phys. Rev. Lett.* 65 (23 Dec. 1990), pp. 2901–2904. URL: `https://journals.aps.org/prl/abstract/10.1103/PhysRevLett.65.2901`.

[Cap+18] M. Caputo, L. Khalil, E. Papalazarou, N. Nilforoushan, L. Perfetti, A. Taleb-Ibrahimi, Q. D. Gibson, R. J. Cava, and M. Marsi. “Dynamics of out-of-equilibrium electron and hole pockets in the type-II Weyl semimetal candidate WTe_2”. In: *Phys. Rev. B* 97 (11 Mar. 2018), p. 115115. URL: `https://link.aps.org/doi/10.1103/PhysRevB.97.115115`.

[CEE08] A. V. Chubukov, D. V. Efremov, and I. Eremin. “Magnetism, superconductivity, and pairing symmetry in iron-based superconductors”. In: *Phys. Rev. B* 78 (13 Oct. 2008), p. 134512. URL: `https://link.aps.org/doi/10.1103/PhysRevB.78.134512`.

[Cha+91] J.-C. Charlier, J.-P. Michenaud, X. Gonze, and J.-P. Vigneron. “Tight-binding model for the electronic properties of simple hexagonal graphite”. In: *Phys. Rev. B* 44.24 (1991), pp. 13237–13249. URL: `http://link.aps.org/doi/10.1103/PhysRevB.44.13237`.

[Che+15] C.-Z. Chen, J. Song, H. Jiang, Q.-f. Sun, Z. Wang, and X. C. Xie. “Disorder and Metal-Insulator Transitions in Weyl Semimetals”. In: *Phys. Rev. Lett.* 115.24 (24 Dec. 2015), p. 246603. URL: `https://doi.org/10.1103/physrevlett.115.246603`.

[Che45] S.-s. Chern. “On the Curvatura Integra in a Riemannian Manifold”. In: *Annals of Mathematics* 46.4 (1945), pp. 674–684. ISSN: 0003486X. URL: `http://www.jstor.org/stable/1969203`.

[Chi+16] M. Chinotti, A. Pal, W. J. Ren, C. Petrovic, and L. Degiorgi. “Electrodynamic response of the type-II Weyl semimetal YbMnBi_2”. In: *Phys. Rev. B* 94 (24 Dec. 2016), p. 245101. URL: `https://link.aps.org/doi/10.1103/PhysRevB.94.245101`.

[Com+16] F. Combes, M. Trescher, F. Piéchon, and J.-N. Fuchs. In: *Phys. Rev. B* 94 (15 Oct. 2016), p. 155109. URL: `https://link.aps.org/doi/10.1103/PhysRevB.94.155109`.

[Dat97] S. Datta. *Electronic Transport in Mesoscopic Systems.* Cambridge University Press, 1997.

[Den+16] K. Deng, G. Wan, P. Deng, K. Zhang, S. Ding, E. Wang, M. Yan, H. Huang, H. Zhang, Z. Xu, J. Denlinger, A. Fedorov, H. Yang, W. Duan, H. Yao, Y. Wu, S. Fan, H. Zhang, X. Chen, and S. Zhou. “Experimental observation of topological Fermi arcs in type-II Weyl semimetal MoTe2”. In: *Nature Physics* 12.12 (Sept. 2016), pp. 1105–1110. URL: `https://doi.org/10.1038/nphys3871`.

[DiC+08] L. DiCarlo, J. R. Williams, Y. Zhang, D. T. McClure, and C. M. Marcus. “Shot Noise in Graphene”. In: *Phys. Rev. Lett.* 100.15 (Apr. 2008). URL: `https://doi.org/10.1103/physrevlett.100.156801`.

[Dir28] P. A. M. Dirac. “The quantum theory of the electron”. In: *Proceedings of the Royal Society of London A: Mathematical, Physical and Engineering Sciences* 117.778 (1928), pp. 610–624. ISSN: 0950-1207. URL: `http://rspa.royalsocietypublishing.org/content/117/778/610`.

[Fan+03] Z. Fang, N. Nagaosa, K. S. Takahashi, A. Asamitsu, R. Mathieu, T. Ogasawara, H. Yamada, M. Kawasaki, Y. Tokura, and K. Terakura. "The Anomalous Hall Effect and Magnetic Monopoles in Momentum Space". In: *Science* 302.5642 (2003), pp. 92–95. URL: `http://www.sciencemag.org/content/302/5642/92`.

[Fan+16] C. Fang, L. Lu, J. Liu, and L. Fu. "Topological semimetals with helicoid surface states". In: *Nature Physics* 12.10 (June 2016), pp. 936–941. URL: `https://doi.org/10.1038/nphys3782`.

[Fat+17] V. Fatemi, Q. D. Gibson, K. Watanabe, T. Taniguchi, R. J. Cava, and P. Jarillo-Herrero. "Magnetoresistance and quantum oscillations of an electrostatically tuned semimetal-to-metal transition in ultrathin WTe_2". In: *Phys. Rev. B* 95.4 (2017), p. 041410. URL: `https://link.aps.org/doi/10.1103/PhysRevB.95.041410`.

[Fau+13] B. Fauqué, D. LeBoeuf, B. Vignolle, M. Nardone, C. Proust, and K. Behnia. "Two Phase Transitions Induced by a Magnetic Field in Graphite". In: *Phys. Rev. Lett.* 110 (26 June 2013), p. 266601. URL: `https://link.aps.org/doi/10.1103/PhysRevLett.110.266601`.

[FKM07] L. Fu, C. L. Kane, and E. J. Mele. "Topological Insulators in Three Dimensions". In: *Phys. Rev. Lett.* 98.10 (2007), p. 106803. URL: `http://link.aps.org/doi/10.1103/PhysRevLett.98.106803`.

[FPA79] H. Fukuyama, P. M. Platzman, and P. W. Anderson. "Two-dimensional electron gas in a strong magnetic field". In: *Phys. Rev. B* 19.10 (June 1979), pp. 5211–5217. ISSN: 0163-1829. URL: `http://dx.doi.org/10.1103/physrevb.19.5211`.

[Fra86] E. Fradkin. "Critical behavior of disordered degenerate semiconductors. II. Spectrum and transport properties in mean-field theory". In: *Phys. Rev. B* 33.5 (Mar. 1986), pp. 3263–3268. ISSN: 0163-1829. URL: `http://dx.doi.org/10.1103/physrevb.33.3263`.

[GLS04] M. O. Goerbig, P. Lederer, and C. M. Smith. "Competition between quantum-liquid and electron-solid phases in intermediate Landau levels". In: *Phys. Rev. B* 69.11 (Mar. 2004), p. 115327. ISSN: 1550-235X. URL: `http://dx.doi.org/10.1103/physrevb.69.115327`.

[Goe+08] M. O. Goerbig, J.-N. Fuchs, G. Montambaux, and F. Piechon. "Tilted anisotropic Dirac cones in quinoid-type graphene and alpha-$(\mathrm{BEDT\text{-}TTF})_2 I_3$". In: *Phys. Rev. B* 78.4 (2008), p. 045415. URL: `http://link.aps.org/doi/10.1103/PhysRevB.78.045415`.

[Goe11] M. O. Goerbig. "Electronic properties of graphene in a strong magnetic field". In: *Rev. Mod. Phys.* 83.4 (Nov. 2011), pp. 1193–1243. ISSN: 1539-0756. URL: `http://dx.doi.org/10.1103/revmodphys.83.1193`.

[Gon+17] J. X. Gong, J. Yang, M. Ge, Y. J. Wang, D. D. Liang, L. Luo, X. Yan, W. L. Zhen, S. R. Weng, L. Pi, W. K. Zhu, and C. J. Zhang. "Non-stoichiometry effects on the extreme magnetoresistance in Weyl semimetal WTe2". In: *arxiv:1712.10200v1* (2017). URL: `http://arxiv.org/abs/1712.10200v1`.

[Gru12] A. G. Grushin. "Consequences of a condensed matter realization of Lorentz-violating QED in Weyl semi-metals". In: *Phys. Rev. D* 86.4 (Aug. 2012). ISSN: 1550-2368. URL: `http://dx.doi.org/10.1103/PhysRevD.86.045001`.

[GT13] P. Goswami and S. Tewari. "Axionic field theory of (3 + 1)-dimensional Weyl semimetals". In: *Phys. Rev. B* 88 (24 Dec. 2013), p. 245107. URL: `https://link.aps.org/doi/10.1103/PhysRevB.88.245107`.

[Hal79] E. H. Hall. "On a New Action of the Magnet on Electric Currents". In: *American Journal of Mathematics* 2.3 (1879), pp. 287–292. ISSN: 00029327, 10806377. URL: `http://www.jstor.org/stable/2369245`.

[Hal88] F. D. M. Haldane. "Model for a Quantum Hall Effect without Landau Levels: Condensed-Matter Realization of the "Parity Anomaly"". In: *Phys. Rev. Lett.* 61 (18 Oct. 1988), pp. 2015–2018. URL: `https://link.aps.org/doi/10.1103/PhysRevLett.61.2015`.

[Her37] C. Herring. "Accidental Degeneracy in the Energy Bands of Crystals". In: *Physical Review* 52.4 (1937), pp. 365–373. URL: `https://link.aps.org/doi/10.1103/PhysRev.52.365`.

[HQ13] P. Hosur and X. Qi. "Recent developments in transport phenomena in Weyl semimetals". In: *Comptes Rendus Physique* 14.9–10 (2013), p. 857. URL: `https://doi.org/10.1016/j.crhy.2013.10.010`.

[Hua+15] X. Huang, L. Zhao, Y. Long, P. Wang, D. Chen, Z. Yang, H. Liang, M. Xue, H. Weng, Z. Fang, X. Dai, and G. Chen. "Observation of the Chiral-Anomaly-Induced Negative Magnetoresistance in 3D Weyl Semimetal TaAs". In: *Physical Review X* 5.3 (Aug. 2015), p. 031023. ISSN: 2160-3308. URL: `http://dx.doi.org/10.1103/physrevx.5.031023`.

[Hua+16] L. Huang, T. M. McCormick, M. Ochi, Z. Zhao, M.-T. Suzuki, R. Arita, Y. Wu, D. Mou, H. Cao, J. Yan, N. Trivedi, and A. Kaminski. "Spectroscopic evidence for a type II Weyl semimetallic state in MoTe2". In: *Nature Materials* 15.11 (July 2016), pp. 1155–1160. URL: `https://doi.org/10.1038/nmat4685`.

[JPB94] R. A. Jalabert, J.-L. Pichard, and C. W. J. Beenakker. "Universal Quantum Signatures of Chaos in Ballistic Transport". In: *EPL (Europhysics Letters)* 27.4 (1994), p. 255. URL: `http://iopscience.iop.org/0295-5075/27/4/001`.

[Kat06] M. I. Katsnelson. “Zitterbewegung, chirality, and minimal conductivity in graphene”. In: *The European Physical Journal B - Condensed Matter and Complex Systems* 51.2 (2006), pp. 157–160. URL: `http://link.springer.com/article/10.1140/epjb/e2006-00203-1`.

[KC15] J. Knolle and N. R. Cooper. “Quantum Oscillations without a Fermi Surface and the Anomalous de Haas–van Alphen Effect”. In: *Phys. Rev. Lett.* 115.14 (Sept. 2015). URL: `https://doi.org/10.1103/physrevlett.115.146401`.

[KDP80] K. v. Klitzing, G. Dorda, and M. Pepper. “New Method for High-Accuracy Determination of the Fine-Structure Constant Based on Quantized Hall Resistance”. In: *Phys. Rev. Lett.* 45 (6 Aug. 1980), pp. 494–497. URL: `https://link.aps.org/doi/10.1103/PhysRevLett.45.494`.

[KGM15] J. Klier, I. V. Gornyi, and A. D. Mirlin. “Transversal magnetoresistance in Weyl semimetals”. In: *Phys. Rev. B* 92.20 (Nov. 2015). URL: `https://doi.org/10.1103/physrevb.92.205113`.

[KGM17] J. Klier, I. V. Gornyi, and A. D. Mirlin. “Transversal magnetoresistance and Shubnikovde Haas oscillations in Weyl semimetals”. In: *Phys. Rev. B* 96 (21 Dec. 2017), p. 214209. URL: `https://link.aps.org/doi/10.1103/PhysRevB.96.214209`.

[Khv01] D. V. Khveshchenko. “Magnetic-Field-Induced Insulating Behavior in Highly Oriented Pyrolitic Graphite”. In: *Phys. Rev. Lett.* 87.20 (2001), p. 206401. URL: `https://link.aps.org/doi/10.1103/PhysRevLett.87.206401`.

[KKS06] S. Katayama, A. Kobayashi, and Y. Suzumura. “Pressure-Induced Zero-Gap Semiconducting State in Organic Conductor α-(BEDT-TTF)2I3 Salt”. In: *Journal of the Physical Society of Japan* 75.5 (2006), p. 054705. URL: `http://journals.jps.jp/doi/abs/10.1143/JPSJ.75.054705`.

[Kob+07] A. Kobayashi, S. Katayama, Y. Suzumura, and H. Fukuyama. “Massless Fermions in Organic Conductor”. In: *J. Phys. Soc. Jpn.* 76.3 (Mar. 2007), p. 034711. ISSN: 1347-4073. URL: `http://dx.doi.org/10.1143/jpsj.76.034711`.

[Kob+14] K. Kobayashi, T. Ohtsuki, K.-I. Imura, and I. F. Herbut. “Density of States Scaling at the Semimetal to Metal Transition in Three Dimensional Topological Insulators”. In: *Phys. Rev. Lett.* 112.1 (Jan. 2014). ISSN: 1079-7114. URL: `http://dx.doi.org/10.1103/physrevlett.112.016402`.

[Koe+16] K. Koepernik, D. Kasinathan, D. V. Efremov, S. Khim, S. Borisenko, B. Büchner, and J. van den Brink. “TaIrTe$_4$: A ternary type-II Weyl semimetal”. In: *Phys. Rev. B* 93 (20 June 2016), p. 201101. URL: `https://link.aps.org/doi/10.1103/PhysRevB.93.201101`.

[Kön+07] M. König, S. Wiedmann, C. Brüne, A. Roth, H. Buhmann, L. W. Molenkamp, X.-L. Qi, and S.-C. Zhang. “Quantum Spin Hall Insulator State in HgTe Quantum Wells”. In: *Science* 318.5851 (Nov. 2007), pp. 766–770. URL: `https://doi.org/10.1126/science.1148047`.

[Kon64] J. Kondo. “Resistance Minimum in Dilute Magnetic Alloys”. In: *Progress of Theoretical Physics* 32.1 (1964), pp. 37–49. URL: `http://dx.doi.org/10.1143/PTP.32.37`.

[Kra30] H. A. Kramers. “Théorie générale de la rotation paramagnétique dans les cristaux”. In: *Proc. Amsterdam Acad.* 33 (1930), pp. 959–972.

[KTB17] F. K. Kunst, M. Trescher, and E. J. Bergholtz. “Anatomy of topological surface states: Exact solutions from destructive interference on frustrated lattices”. In: *Phys. Rev. B* 96.8 (Aug. 2017). URL: `https://doi.org/10.1103/physrevb.96.085443`.

[Kub57] R. Kubo. “Statistical-Mechanical Theory of Irreversible Processes. I. General Theory and Simple Applications to Magnetic and Conduction Problems”. In: *Journal of the Physical Society of Japan* 12.6 (1957), pp. 570–586. URL: `https://doi.org/10.1143/JPSJ.12.570`.

[Kum+17] N. Kumar, Y. Sun, N. Xu, K. Manna, M. Yao, V. Süss, I. Leermakers, O. Young, T. Förster, M. Schmidt, H. Borrmann, B. Yan, U. Zeitler, M. Shi, C. Felser, and C. Shekhar. “Extremely high magnetoresistance and conductivity in the type-II Weyl semimetals WP2 and MoP2”. In: *Nature Communications* 8.1 (Nov. 2017). URL: `https://doi.org/10.1038/s41467-017-01758-z`.

[Lan57] R. Landauer. “Spatial Variation of Currents and Fields Due to Localized Scatterers in Metallic Conduction”. In: *IBM Journal of Research and Development* 1.3 (July 1957), pp. 223–231. URL: `https://doi.org/10.1147/rd.13.0223`.

[Lan70] R. Landauer. “Electrical resistance of disordered one-dimensional lattices”. In: *The Philosophical Magazine: A Journal of Theoretical Experimental and Applied Physics* 21.172 (1970), pp. 863–867. URL: `https://doi.org/10.1080/14786437008238472`.

[Lau+16] M. Laubach, C. Platt, R. Thomale, T. Neupert, and S. Rachel. “Density wave instabilities and surface state evolution in interacting Weyl semimetals”. In: *Phys. Rev. B* 94 (24 Dec. 2016), p. 241102. URL: `https://link.aps.org/doi/10.1103/PhysRevB.94.241102`.

[LCF16] T. Louvet, D. Carpentier, and A. A. Fedorenko. “On the disorder-driven quantum transition in three-dimensional relativistic metals”. In: *Phys. Rev. B* 94 (22 Dec. 2016), p. 220201. URL: `https://link.aps.org/doi/10.1103/PhysRevB.94.220201`.

[LeB+17] D. LeBoeuf, C. W. Rischau, G. Seyfarth, R. Küchler, M. Berben, S. Wiedmann, W. Tabis, M. Frachet, K. Behnia, and B. Fauqué. “Thermodynamic signatures of the field-induced states of graphite”. In: *Nature Communications* 8.1 (Nov. 2017). URL: `https://doi.org/10.1038/s41467-017-01394-7`.

[Les89] G. B. Lesovik. “Excess quantum noise in 2D ballistic point contacts”. In: *JETP Letters* 49 (9 Mar. 1989), p. 592. URL: `http://www.jetpletters.ac.ru/ps/1120/article_16970.shtml`.

[Liu+14a] Z. K. Liu, J. Jiang, B. Zhou, Z. J. Wang, Y. Zhang, H. M. Weng, D. Prabhakaran, S.-K. Mo, H. Peng, P. Dudin, T. Kim, M. Hoesch, Z. Fang, X. Dai, Z. X. Shen, D. L. Feng, Z. Hussain, and Y. L. Chen. “A stable three-dimensional topological Dirac semimetal Cd3As2”. In: *Nature Materials* 13.7 (2014), p. 677. URL: `http://www.nature.com/nmat/journal/v13/n7/full/nmat3990.html`.

[Liu+14b] Z. K. Liu, B. Zhou, Y. Zhang, Z. J. Wang, H. M. Weng, D. Prabhakaran, S.-K. Mo, Z. X. Shen, Z. Fang, X. Dai, Z. Hussain, and Y. L. Chen. “Discovery of a Three-Dimensional Topological Dirac Semimetal, Na3Bi”. In: *Science* 343.6173 (2014), p. 864. URL: `http://www.sciencemag.org/content/343/6173/864`.

[Liu+17a] J. Y. Liu, J. Hu, D. Graf, T. Zou, M. Zhu, Y. Shi, S. Che, S. M. A. Radmanesh, C. N. Lau, L. Spinu, H. B. Cao, X. Ke, and Z. Q. Mao. “Unusual interlayer quantum transport behavior caused by the zeroth Landau level in YbMnBi2”. In: *Nature Communications* 8.1 (2017), p. 646. ISSN: 2041-1723. URL: `https://doi.org/10.1038/s41467-017-00673-7`.

[Liu+17b] J. Y. Liu, J. Hu, Q. Zhang, D. Graf, H. B. Cao, S. M. A. Radmanesh, D. J. Adams, Y. L. Zhu, G. ? F. Cheng, X. Liu, W. A. Phelan, J. Wei, M. Jaime, F. Balakirev, D. A. Tennant, J. F. DiTusa, I. Chiorescu, L. Spinu, and Z. Q. Mao. “A magnetic topological semimetal Sr1-yMn1-zSb2 (y, z ¡ 0.1)”. In: *Nature Materials* 16 (July 2017), pp. 905–910. URL: `http://dx.doi.org/10.1038/nmat4953`.

[Lu+15] L. Lu, Z. Wang, D. Ye, L. Ran, L. Fu, J. D. Joannopoulos, and M. Soljačić. “Experimental observation of Weyl points”. In: *Science* 349.6248 (July 2015), pp. 622–624. ISSN: 1095-9203. URL: `http://dx.doi.org/10.1126/science.aaa9273`.

[Lv+15] B. Q. Lv, H. M. Weng, B. B. Fu, X. P. Wang, H. Miao, J. Ma, P. Richard, X. C. Huang, L. X. Zhao, G. F. Chen, Z. Fang, X. Dai, T. Qian, and H. Ding. “Experimental Discovery of Weyl Semimetal TaAs”. In: *Phys. Rev. X* 5 (3 July 2015), p. 031013. URL: `http://link.aps.org/doi/10.1103/PhysRevX.5.031013`.

[LYQ13] C.-X. Liu, P. Ye, and X.-L. Qi. “Chiral gauge field and axial anomaly in a Weyl semimetal”. In: *Phys. Rev. B* 87 (23 June 2013), p. 235306. URL: `https://link.aps.org/doi/10.1103/PhysRevB.87.235306`.

[LZQ16] C.-X. Liu, S.-C. Zhang, and X.-L. Qi. “The Quantum Anomalous Hall Effect: Theory and Experiment”. In: *Annual Review of Condensed Matter Physics* 7.1 (2016), pp. 301–321. URL: `https://doi.org/10.1146/annurev-conmatphys-031115-011417`.

[MB07] J. Moore and L. Balents. “Topological invariants of time-reversal-invariant band structures”. In: *Phys. Rev. B* 75.12 (2007), p. 121306. URL: `http://link.aps.org/doi/10.1103/PhysRevB.75.121306`.

[McK+95] S. K. McKernan, S. T. Hannahs, U. M. Scheven, G. M. Danner, and P. M. Chaikin. “Competing Instabilities and the High Field Phases of $(\mathrm{TMTSF})_2$ ClO_4”. In: *Phys. Rev. Lett.* 75 (8 Aug. 1995), pp. 1630–1633. URL: `https://link.aps.org/doi/10.1103/PhysRevLett.75.1630`.

[McK10] W. McKinney. “Data Structures for Statistical Computing in Python”. In: *Proceedings of the 9th Python in Science Conference*. Ed. by S. van der Walt and J. Millman. 2010, pp. 51–56.

[Men+16] T. Meng, A. G. Grushin, K. Shtengel, and J. H. Bardarson. “Theory of a 3+1D fractional chiral metal: Interacting variant of the Weyl semimetal”. In: *Phys. Rev. B* 94.15 (Oct. 2016). URL: `https://doi.org/10.1103/physrevb.94.155136`.

[Meu+17] A. Meurer, C. P. Smith, M. Paprocki, O. Čertík, S. B. Kirpichev, M. Rocklin, A. Kumar, S. Ivanov, J. K. Moore, S. Singh, T. Rathnayake, S. Vig, B. E. Granger, R. P. Muller, F. Bonazzi, H. Gupta, S. Vats, F. Johansson, F. Pedregosa, M. J. Curry, A. R. Terrel, Š. Roučka, A. Saboo, I. Fernando, S. Kulal, R. Cimrman, and A. Scopatz. “SymPy: symbolic computing in Python”. In: *PeerJ Computer Science* 3 (Jan. 2017), e103. ISSN: 2376-5992. URL: `https://doi.org/10.7717/peerj-cs.103`.

[Mol+16] P. J. W. Moll, N. L. Nair, T. Helm, A. C. Potter, I. Kimchi, A. Vishwanath, and J. G. Analytis. “Transport evidence for Fermi-arc-mediated chirality transfer in the Dirac semimetal Cd3As2”. In: *Nature* 535.7611 (July 2016). Letter, pp. 266–270. ISSN: 0028-0836. URL: `http://dx.doi.org/10.1038/nature18276`.

[Mur07] S. Murakami. “Phase transition between the quantum spin Hall and insulator phases in 3D: emergence of a topological gapless phase”. In: *New Journal of Physics* 9.9 (2007), p. 356. URL: `http://iopscience.iop.org/1367-2630/9/9/356`.

[NB09] Y. V. Nazarov and Y. M. Blanter. *Quantum Transport: Introduction to Nanoscience*. Cambridge University Press, 2009.

[NHS14] R. Nandkishore, D. A. Huse, and S. L. Sondhi. “Rare region effects dominate weakly disordered three-dimensional Dirac points”. In: *Phys. Rev. B* 89.24 (June 2014). ISSN: 1550-235X. URL: `http://dx.doi.org/10.1103/PhysRevB.89.245110`.

[NKA10] M. Noro, M. Koshino, and T. Ando. “Theory of Transport in Graphene with Long-Range Scatterers”. In: *Journal of the Physical Society of Japan* 79.9 (Sept. 2010), p. 094713. URL: `https://doi.org/10.1143/jpsj.79.094713`.

[NN83] H. Nielsen and M. Ninomiya. “The Adler-Bell-Jackiw anomaly and Weyl fermions in a crystal”. In: *Physics Letters B* 130.6 (Nov. 1983), pp. 389–396. URL: `https://doi.org/10.1016%5C%5C%2F0370-2693%5C%5C%2883%5C%5C%2991529-0`.

[Nov+04] K. S. Novoselov, A. K. Geim, S. V. Morozov, D. Jiang, Y. Zhang, S. V. Dubonos, I. V. Grigorieva, and A. A. Firsov. “Electric Field Effect in Atomically Thin Carbon Films”. In: *Science* 306.5696 (2004), pp. 666–669. URL: `http://www.sciencemag.org/content/306/5696/666`.

[Nov+05] K. S. Novoselov, A. K. Geim, S. V. Morozov, D. Jiang, M. I. Katsnelson, I. V. Grigorieva, S. V. Dubonos, and A. A. Firsov. “Two-dimensional gas of massless Dirac fermions in graphene”. In: *Nature* 438.7065 (2005), pp. 197–200. URL: `http://www.nature.com/nature/journal/v438/n7065/abs/nature04233.html`.

[Ohm27] G. S. Ohm. *Die galvanische Kette.* Berlin: Deutsches Textarchiv (Kernkorpus), 1827. URL: `http://www.deutschestextarchiv.de/ohm_galvanische_1827`.

[Oja13] T. Ojanen. “Helical Fermi arcs and surface states in time-reversal invariant Weyl semimetals”. In: *Phys. Rev. B* 87.24 (June 2013). ISSN: 1550-235X. URL: `http://dx.doi.org/10.1103/physrevb.87.245112`.

[OK14] Y. Ominato and M. Koshino. “Quantum transport in a three-dimensional Weyl electron system”. In: *Phys. Rev. B* 89.5 (Feb. 2014), p. 054202. ISSN: 1550-235X. URL: `http://dx.doi.org/10.1103/physrevb.89.054202`.

[Oli07] T. E. Oliphant. “Python for Scientific Computing”. In: *Computing in Science & Engineering* 9.3 (2007), pp. 10–20. URL: `https://doi.org/10.1109/mcse.2007.58`.

[PAP11] F. M. D. Pellegrino, G. G. N. Angilella, and R. Pucci. “Transport properties of graphene across strain-induced nonuniform velocity profiles”. In: *Phys. Rev. B* 84.19 (2011), p. 195404. URL: `http://link.aps.org/doi/10.1103/PhysRevB.84.195404`.

[Par+14] S. A. Parameswaran, T. Grover, D. A. Abanin, D. A. Pesin, and A. Vishwanath. “Probing the Chiral Anomaly with Nonlocal Transport in Three-Dimensional Topological Semimetals”. In: *Physical Review X* 4.3 (Sept. 2014). URL: `https://doi.org/10.1103/physrevx.4.031035`.

[Pez+17] S. Pezzini, M. R. van Delft, L. M. Schoop, B. V. Lotsch, A. Carrington, M. I. Katsnelson, N. E. Hussey, and S. Wiedmann. “Unconventional mass enhancement around the Dirac nodal loop in ZrSiS”. In: *Nature Physics* 14 (Nov. 2017), pp. 178–183. URL: `http://dx.doi.org/10.1038/nphys4306`.

[PGS15] J. H. Pixley, P. Goswami, and S. D. Sarma. “Anderson Localization and the Quantum Phase Diagram of Three Dimensional Disordered Dirac Semimetals”. In: *Phys. Rev. Lett.* 115.7 (Aug. 2015). URL: `https://doi.org/10.1103/physrevlett.115.076601`.

[PKV14] A. C. Potter, I. Kimchi, and A. Vishwanath. “Quantum oscillations from surface Fermi arcs in Weyl and Dirac semimetals”. In: *Nature Communications* 5 (Oct. 2014), p. 5161. ISSN: 2041-1723. URL: `http://dx.doi.org/10.1038/ncomms6161`.

[PML15] D. A. Pesin, E. G. Mishchenko, and A. Levchenko. “Density of states and magnetotransport in Weyl semimetals with long-range disorder”. In: *Phys. Rev. B* 92.17 (Nov. 2015). ISSN: 1550-235X. URL: `http://dx.doi.org/10.1103/physrevb.92.174202`.

[Ram+17] B. J. Ramshaw, K. A. Modic, A. Shekhter, Y. Zhang, E.-A. Kim, P. J. W. Moll, M. Bachmann, M. K. Chan, J. B. Betts, F. Balakirev, A. Migliori, N. J. Ghimire, E. D. Bauer, F. Ronning, and R. D. McDonald. “Unmasking Weyl Fermions using Extreme Magnetic Fields”. In: *arxiv:1704.06944v2* (2017). URL: `http://arxiv.org/abs/1704.06944v2`.

[Raz+18] E. Razzoli, B. Zwartsenberg, M. Michiardi, F. Boschini, R. P. Day, I. S. Elfimov, J. D. Denlinger, V. Süß, C. Felser, and A. Damascelli. “Stable Weyl points, trivial surface states and particle-hole compensation in WP2”. In: *arxiv:1801.03956v1* (2018). URL: `http://arxiv.org/abs/1801.03956v1`.

[RGJ17] B. Roy, P. Goswami, and V. Juričić. “Interacting Weyl fermions: Phases, phase transitions, and global phase diagram”. In: *Phys. Rev. B* 95 (20 June 2017), p. 201102. URL: `https://link.aps.org/doi/10.1103/PhysRevB.95.201102`.

[RJS16] B. Roy, V. Juričić, and S. D. Sarma. “Universal optical conductivity of a disordered Weyl semimetal”. In: *Scientific Reports* 6.1 (Aug. 2016). URL: `https://doi.org/10.1038/srep32446`.

[RKL17] B. Rosenstein, H. C. Kao, and M. Lewkowicz. “Nonlocal electrodynamics in Weyl semimetals”. In: *Phys. Rev. B* 95 (8 Feb. 2017), p. 085148. URL: `https://link.aps.org/doi/10.1103/PhysRevB.95.085148`.

[RKN15] Y. I. Rodionov, K. I. Kugel, and F. Nori. "Effects of anisotropy and disorder on the conductivity of Weyl semimetals". In: *Phys. Rev. B* 92.19 (Nov. 2015), p. 195117. ISSN: 1550-235X. URL: `http://dx.doi.org/10.1103/physrevb.92.195117`.

[Roy09] R. Roy. "Topological phases and the quantum spin Hall effect in three dimensions". In: *Phys. Rev. B* 79.19 (2009), p. 195322. URL: `http://link.aps.org/doi/10.1103/PhysRevB.79.195322`.

[RS15a] Y. I. Rodionov and S. V. Syzranov. "Conductivity of a Weyl semimetal with donor and acceptor impurities". In: *Phys. Rev. B* 91.19 (June 2015). ISSN: 1550-235X. URL: `http://dx.doi.org/10.1103/PhysRevB.91.195107`.

[RS15b] B. Roy and J. D. Sau. "Magnetic catalysis and axionic charge density wave in Weyl semimetals". In: *Phys. Rev. B* 92 (12 Sept. 2015), p. 125141. URL: `https://link.aps.org/doi/10.1103/PhysRevB.92.125141`.

[Ryu+10] S. Ryu, A. P. Schnyder, A. Furusaki, and A. W. W. Ludwig. "Topological insulators and superconductors: tenfold way and dimensional hierarchy". In: *New Journal of Physics* 12.6 (2010), p. 065010. URL: `http://stacks.iop.org/1367-2630/12/i=6/a=065010`.

[Sak94] J. J. Sakurai. *Modern quantum mechanics; rev. ed.* Reading, MA: Addison-Wesley, 1994. URL: `https://cds.cern.ch/record/1167961`.

[SBB15] B. Sbierski, E. J. Bergholtz, and P. W. Brouwer. "Quantum critical exponents for a disordered three-dimensional Weyl node". In: *Phys. Rev. B* 92 (11 Sept. 2015), p. 115145. URL: `http://link.aps.org/doi/10.1103/PhysRevB.92.115145`.

[Sbi+14] B. Sbierski, G. Pohl, E. J. Bergholtz, and P. W. Brouwer. "Quantum Transport of Disordered Weyl Semimetals at the Nodal Point". In: *Phys. Rev. Lett.* 113.2 (2014), p. 026602. URL: `http://link.aps.org/doi/10.1103/PhysRevLett.113.026602`.

[Sbi+17] B. Sbierski, M. Trescher, E. J. Bergholtz, and P. W. Brouwer. "Disordered double Weyl node: Comparison of transport and density of states calculations". In: *Phys. Rev. B* 95.11 (Mar. 2017). URL: `https://doi.org/10.1103/physrevb.95.115104`.

[Sbi16] B. Sbierski. *On disorder effects in topological insulators and semimetals.* 2016.

[SDB16] B. Sbierski, K. S. C. Decker, and P. W. Brouwer. "Weyl node with random vector potential". In: *Phys. Rev. B* 94 (22 Dec. 2016), p. 220202. URL: `https://link.aps.org/doi/10.1103/PhysRevB.94.220202`.

[Sen15] T. Senthil. "Symmetry-Protected Topological Phases of Quantum Matter". In: *Annual Review of Condensed Matter Physics* 6.1 (2015), pp. 299–324. URL: `https://doi.org/10.1146/annurev-conmatphys-031214-014740`.

[SF17] T. S. Sikkenk and L. Fritz. “Disorder in tilted Weyl semimetals from a renormalization group perspective”. In: *Phys. Rev. B* 96.15 (Oct. 2017). URL: `https://doi.org/10.1103/physrevb.96.155121`.

[SGT16] G. Sharma, P. Goswami, and S. Tewari. “Nernst and magnetothermal conductivity in a lattice model of Weyl fermions”. In: *Phys. Rev. B* 93 (3 Jan. 2016), p. 035116. URL: `https://link.aps.org/doi/10.1103/PhysRevB.93.035116`.

[Shi+18] H. Shishido, S. Yamada, K. Sugii, M. Shimozawa, Y. Yanase, and M. Yamashita. “Anomalous change in the de Haas-van Alphen oscillations of CeCoIn_5 at ultra-low temperatures”. In: *arxiv:1803.05142v1* (2018). URL: `http://arxiv.org/abs/1803.05142v1`.

[Sho84] D. Shoenberg. *Magnetic Oscillations in Metals*. Cambridge Monographs on Physics. Cambridge University Press, 1984.

[Sim83] B. Simon. “Holonomy, the Quantum Adiabatic Theorem, and Berry’s Phase”. In: *Phys. Rev. Lett.* 51 (24 Dec. 1983), pp. 2167–2170. URL: `https://link.aps.org/doi/10.1103/PhysRevLett.51.2167`.

[Sol+15] A. A. Soluyanov, D. Gresch, Z. Wang, Q. Wu, M. Troyer, X. Dai, and B. A. Bernevig. “Type-II Weyl semimetals”. In: *Nature* 527.7579 (Nov. 2015), pp. 495–498. ISSN: 1476-4687. URL: `http://dx.doi.org/10.1038/nature15768`.

[SR17] S. V. Syzranov and L. Radzihovsky. “High-Dimensional Disorder-Driven Phenomena in Weyl Semimetals, Semiconductors, and Related Systems”. In: *Annual Review of Condensed Matter Physics* 9.1 (Nov. 2017). URL: `https://doi.org/10.1146/annurev-conmatphys-033117-054037`.

[SRG15] S. V. Syzranov, L. Radzihovsky, and V. Gurarie. “Critical Transport in Weakly Disordered Semiconductors and Semimetals”. In: *Phys. Rev. Lett.* 114.16 (Apr. 2015). ISSN: 1079-7114. URL: `http://dx.doi.org/10.1103/PhysRevLett.114.166601`.

[SY12] D. T. Son and N. Yamamoto. “Berry Curvature, Triangle Anomalies, and the Chiral Magnetic Effect in Fermi Liquids”. In: *Phys. Rev. Lett.* 109 (18 Nov. 2012), p. 181602. URL: `https://link.aps.org/doi/10.1103/PhysRevLett.109.181602`.

[SY16] J. M. Shao and G. W. Yang. “Magneto-optical conductivity of Weyl semimetals with quadratic term in momentum”. In: *AIP Advances* 6.2 (Feb. 2016), p. 025312. URL: `https://aip.scitation.org/doi/full/10.1063/1.4942203`.

[SZW15] X.-Q. Sun, S.-C. Zhang, and Z. Wang. “Helical Spin Order from Topological Dirac and Weyl Semimetals”. In: *Phys. Rev. Lett.* 115.7 (Aug. 2015), p. 076802. URL: `https://doi.org/10.1103/physrevlett.115.076802`.

[TB12] M. Trescher and E. J. Bergholtz. “Flat bands with higher Chern number in pyrochlore slabs”. In: *Phys. Rev. B* 86.24 (2012), p. 241111. URL: `http://link.aps.org/doi/10.1103/PhysRevB.86.241111`.

[TBK18] M. Trescher, E. J. Bergholtz, and J. Knolle. “Quantum Oscillations and Magnetoresistance in Type-II Weyl Semimetals - Effect of a Field Induced Charge Density Wave Transition”. In: *in preparation* (2018).

[TC15] C. J. Tabert and J. P. Carbotte. “Particle-hole asymmetry in gapped topological insulator surface states”. In: *Phys. Rev. B* 91.23 (June 2015). URL: `https://journals.aps.org/prb/abstract/10.1103/PhysRevB.91.235405`.

[TCG17] S. Tchoumakov, M. Civelli, and M. O. Goerbig. “Magnetic description of the Fermi arc in type-I and type-II Weyl semimetals”. In: *Phys. Rev. B* 95.12 (Mar. 2017). URL: `https://doi.org/10.1103/physrevb.95.125306`.

[TDB10] S. Tomov, J. Dongarra, and M. Baboulin. “Towards dense linear algebra for hybrid GPU accelerated manycore systems”. In: *Parallel Computing* 36.5-6 (June 2010), pp. 232–240. ISSN: 0167-8191.

[TDB17] S. Tomov, J. Dongarra, and M. Baboulin. *Matrix Algebra on GPU and Multicore Architectures.* 2017. URL: `http://icl.cs.utk.edu/magma/` (visited on 10/02/2017).

[Thi+17] S. Thirupathaiah, R. Jha, B. Pal, J. S. Matias, P. K. Das, P. K. Sivakumar, I. Vobornik, N. C. Plumb, M. Shi, R. A. Ribeiro, and D. D. Sarma. “MoTe2 : An uncompensated semimetal with extremely large magnetoresistance”. In: *Phys. Rev. B* 95.24 (June 2017). URL: `https://doi.org/10.1103/physrevb.95.241105`.

[THK] D. J. Thouless, F. D. M. Haldane, and J. M. Kosterlitz. *The Nobel Prize in Physics 2016.* URL: `https://www.nobelprize.org/nobel_prizes/physics/laureates/2016/` (visited on 09/18/2017).

[Tho+15] L. R. Thoutam, Y. L. Wang, Z. L. Xiao, S. Das, A. Luican-Mayer, R. Divan, G. W. Crabtree, and W. K. Kwok. “Temperature-Dependent Three-Dimensional Anisotropy of the Magnetoresistance in WTe 2”. In: *Phys. Rev. Lett.* 115.4 (July 2015). ISSN: 1079-7114. URL: `http://dx.doi.org/10.1103/physrevlett.115.046602`.

[Tho+82] D. J. Thouless, M. Kohmoto, M. P. Nightingale, and M. den Nijs. “Quantized Hall Conductance in a Two-Dimensional Periodic Potential”. In: *Phys. Rev. Lett.* 49 (6 Aug. 1982), pp. 405–408. URL: `https://link.aps.org/doi/10.1103/PhysRevLett.49.405`.

[Tre+15] M. Trescher, B. Sbierski, P. W. Brouwer, and E. J. Bergholtz. “Quantum transport in Dirac materials: Signatures of tilted and anisotropic Dirac and Weyl cones”. In: *Phys. Rev. B* 91.11 (Mar. 2015), p. 115135. ISSN: 1550-235X. URL: `http://dx.doi.org/10.1103/physrevb.91.115135`.

[Tre+17a] M. Trescher, E. J. Bergholtz, M. Udagawa, and J. Knolle. “Charge density wave instabilities of type-II Weyl semimetals in a strong magnetic field”. In: *Phys. Rev. B* 96 (20 Nov. 2017), p. 201101. URL: `https://link.aps.org/doi/10.1103/PhysRevB.96.201101`.

[Tre+17b] M. Trescher, B. Sbierski, P. W. Brouwer, and E. J. Bergholtz. “Tilted disordered Weyl semimetals”. In: *Phys. Rev. B* 95 (4 Jan. 2017), p. 045139. URL: `http://link.aps.org/doi/10.1103/PhysRevB.95.045139`.

[TV13] A. M. Turner and A. Vishwanath. “Beyond Band Insulators: Topology of Semi-metals and Interacting Phases”. In: *arxiv:1301.0330v1* (2013). URL: `http://arxiv.org/abs/1301.0330v1`.

[Two+06] J. Tworzydło, B. Trauzettel, M. Titov, A. Rycerz, and C. W. J. Beenakker. “Sub-Poissonian Shot Noise in Graphene”. In: *Phys. Rev. Lett.* 96.24 (2006), p. 246802. URL: `http://link.aps.org/doi/10.1103/PhysRevLett.96.246802`.

[UB16] M. Udagawa and E. Bergholtz. “Field-Selective Anomaly and Chiral Mode Reversal in Type-II Weyl Materials”. In: *Phys. Rev. Lett.* 117.8 (Aug. 2016). URL: `https://doi.org/10.1103/physrevlett.117.086401`.

[Vol09] G. E. Volovik. *The Universe in a Helium Droplet*. Oxford University Press (OUP), Feb. 2009. ISBN: http://id.crossref.org/isbn/9780199564842. URL: `http://dx.doi.org/10.1093/acprof:oso/9780199564842.001.0001`.

[Wan+11] X. Wan, A. M. Turner, A. Vishwanath, and S. Y. Savrasov. “Topological semimetal and Fermi-arc surface states in the electronic structure of pyrochlore iridates”. In: *Phys. Rev. B* 83.20 (2011), p. 205101. URL: `http://link.aps.org/doi/10.1103/PhysRevB.83.205101`.

[Wan+16] C. Wang, Y. Zhang, J. Huang, S. Nie, G. Liu, A. Liang, Y. Zhang, B. Shen, J. Liu, C. Hu, Y. Ding, D. Liu, Y. Hu, S. He, L. Zhao, L. Yu, J. Hu, J. Wei, Z. Mao, Y. Shi, X. Jia, F. Zhang, S. Zhang, F. Yang, Z. Wang, Q. Peng, H. Weng, X. Dai, Z. Fang, Z. Xu, C. Chen, and X. J. Zhou. “Observation of Fermi arc and its connection with bulk states in the candidate type-II Weyl semimetal WTe_2”. In: *Phys. Rev. B* 94 (24 Dec. 2016), p. 241119. URL: `https://link.aps.org/doi/10.1103/PhysRevB.94.241119`.

[WBB14] T. Wehling, A. Black-Schaffer, and A. Balatsky. “Dirac materials”. In: *Advances in Physics* 63.1 (2014), pp. 1–76. URL: `http://dx.doi.org/10.1080/00018732.2014.927109`.

[WCA12] H. Wei, S.-P. Chao, and V. Aji. “Excitonic Phases from Weyl Semimetals”. In: *Phys. Rev. Lett.* 109 (19 Nov. 2012), p. 196403. URL: `https://link.aps.org/doi/10.1103/PhysRevLett.109.196403`.

[WCV11] S. van der Walt, S. C. Colbert, and G. Varoquaux. “The NumPy Array: A Structure for Efficient Numerical Computation”. In: *Computing in Science & Engineering* 13.2 (Mar. 2011), pp. 22–30. URL: `https://doi.org/10.1109/mcse.2011.37`.

[Wei+06] A. Weiße, G. Wellein, A. Alvermann, and H. Fehske. “The kernel polynomial method”. In: *Rev. Mod. Phys.* 78 (1 Mar. 2006), pp. 275–306. URL: `http://link.aps.org/doi/10.1103/RevModPhys.78.275`.

[Wey29] H. Weyl. “Elektron und Gravitation. I”. In: *Z. Physik* 56.5-6 (June 1929), pp. 330–352. ISSN: 1434-601X. URL: `http://dx.doi.org/10.1007/bf01339504`.

[Wig32] E. Wigner. “Über die Operation der Zeitumkehr in der Quantenmechanik”. In: *Nachr. Akad. Ges. Wiss. Göttingen* 31 (1932), pp. 546–559. URL: `http://www.digizeitschriften.de/dms/img/?PPN=GDZPPN002509032`.

[Wu+15] Y. Wu, N. H. Jo, M. Ochi, L. Huang, D. Mou, S. L. Bud’ko, P. C. Canfield, N. Trivedi, R. Arita, and A. Kaminski. “Temperature-Induced Lifshitz Transition in WTe_2”. In: *Phys. Rev. Lett.* 115.16 (2015), p. 166602. URL: `https://link.aps.org/doi/10.1103/PhysRevLett.115.166602`.

[WY16] Y. Wang and P. Ye. “Topological density-wave states in a particle-hole symmetric Weyl metal”. In: *Phys. Rev. B* 94 (7 Aug. 2016), p. 075115. URL: `https://link.aps.org/doi/10.1103/PhysRevB.94.075115`.

[WZ13] Z. Wang and S.-C. Zhang. “Chiral anomaly, charge density waves, and axion strings from Weyl semimetals”. In: *Phys. Rev. B* 87 (16 Apr. 2013), p. 161107. URL: `https://link.aps.org/doi/10.1103/PhysRevB.87.161107`.

[XCN10] D. Xiao, M.-C. Chang, and Q. Niu. “Berry Phase Effects on Electronic Properties”. In: *Reviews of Modern Physics* 82.3 (2010). URL: `https://doi.org/10.1103/revmodphys.82.1959`.

[XCZ14] Y. Xu, R.-L. Chu, and C. Zhang. “Anisotropic Weyl Fermions from the Quasiparticle Excitation Spectrum of a 3D Fulde-Ferrell Superfluid”. In: *Phys. Rev. Lett.* 112.13 (2014), p. 136402. URL: `http://link.aps.org/doi/10.1103/PhysRevLett.112.136402`.

[XD16] Y. Xu and L.-M. Duan. “Type-II Weyl points in three-dimensional cold-atom optical lattices”. In: *Physical Review A* 94.5 (Nov. 2016). ISSN: 2469-9934. URL: `http://dx.doi.org/10.1103/physreva.94.053619`.

[Xu+15] S.-Y. Xu, I. Belopolski, N. Alidoust, M. Neupane, G. Bian, C. Zhang, R. Sankar, G. Chang, Z. Yuan, C.-C. Lee, S.-M. Huang, H. Zheng, J. Ma, D. S. Sanchez, B. Wang, A. Bansil, F. Chou, P. P. Shibayev, H. Lin, S. Jia, and M. Z. Hasan. “Discovery of a Weyl fermion semimetal and topological Fermi arcs”. In: *Science* 349.6248 (2015), pp. 613–617. ISSN: 0036-8075. URL: `http://science.sciencemag.org/content/349/6248/613`.

[Xu+16] N. Xu, Z. J. Wang, A. P. Weber, A. Magrez, P. Bugnon, H. Berger, C. E. Matt, J. Z. Ma, B. B. Fu, B. Q. Lv, N. C. Plumb, M. Radovic, E. Pomjakushina, K. Conder, T. Qian, J. H. Dil, J. Mesot, H. Ding, and M. Shi. "Discovery of Weyl semimetal state violating Lorentz invariance in MoTe2". In: *arxiv:1604.02116v1* (2016). URL: `http://arxiv.org/abs/1604.02116v1`.

[XZZ15] Y. Xu, F. Zhang, and C. Zhang. "Structured Weyl Points in Spin-Orbit Coupled Fermionic Superfluids". In: *Phys. Rev. Lett.* 115.26 (Dec. 2015), p. 265304. ISSN: 1079-7114. URL: `http://dx.doi.org/10.1103/physrevlett.115.265304`.

[Yan+17] H.-Y. Yang, T. Nummy, H. Li, S. Jaszewski, M. Abramchuk, D. S. Dessau, and F. Tafti. "Extreme magnetoresistance in the topologically trivial lanthanum monopnictide LaAs". In: *Phys. Rev. B* 96 (23 Dec. 2017), p. 235128. URL: `https://link.aps.org/doi/10.1103/PhysRevB.96.235128`.

[YF81] D. Yoshioka and H. Fukuyama. "Electronic Phase Transition of Graphite in a Strong Magnetic Field". In: *Journal of the Physical Society of Japan* 50.3 (Mar. 1981), pp. 725–726. URL: `https://doi.org/10.1143/jpsj.50.725`.

[YI14] Y. Yamaji and M. Imada. "Metallic Interface Emerging at Magnetic Domain Wall of Antiferromagnetic Insulator: Fate of Extinct Weyl Electrons". In: *Physical Review X* 4.2 (June 2014). ISSN: 2160-3308. URL: `http://dx.doi.org/10.1103/physrevx.4.021035`.

[YLR11] K.-Y. Yang, Y.-M. Lu, and Y. Ran. "Quantum Hall effects in a Weyl semimetal: Possible application in pyrochlore iridates". In: *Phys. Rev. B* 84 (7 Aug. 2011), p. 075129. URL: `https://link.aps.org/doi/10.1103/PhysRevB.84.075129`.

[YYY16] Z.-M. Yu, Y. Yao, and S. A. Yang. "Predicted Unusual Magnetoresponse in Type-II Weyl Semimetals". In: *Phys. Rev. Lett.* 117.7 (Aug. 2016). URL: `https://doi.org/10.1103/physrevlett.117.077202`.

[ZB12] A. A. Zyuzin and A. A. Burkov. "Topological response in Weyl semimetals and the chiral anomaly". In: *Phys. Rev. B* 86 (11 Sept. 2012), p. 115133. URL: `https://link.aps.org/doi/10.1103/PhysRevB.86.115133`.

[Zen+16] L.-K. Zeng, R. Lou, D.-S. Wu, Q. N. Xu, P.-J. Guo, L.-Y. Kong, Y.-G. Zhong, J.-Z. Ma, B.-B. Fu, P. Richard, P. Wang, G. T. Liu, L. Lu, Y.-B. Huang, C. Fang, S.-S. Sun, Q. Wang, L. Wang, Y.-G. Shi, H. M. Weng, H.-C. Lei, K. Liu, S.-C. Wang, T. Qian, J.-L. Luo, and H. Ding. "Compensated Semimetal LaSb with Unsaturated Magnetoresistance". In: *Phys. Rev. Lett.* 117.12 (Sept. 2016). URL: `https://doi.org/10.1103/physrevlett.117.127204`.

[Zha+05] Y. Zhang, Y.-W. Tan, H. L. Stormer, and P. Kim. "Experimental observation of the quantum Hall effect and Berry's phase in graphene". In: *Nature* 438.7065 (2005), pp. 201–204. URL: `http://www.nature.com/nature/journal/v438/n7065/full/nature04235.html`.

[Zha+10] Y. Zhang, K. He, C.-Z. Chang, C.-L. Song, L.-L. Wang, X. Chen, J.-F. Jia, Z. Fang, X. Dai, W.-Y. Shan, S.-Q. Shen, Q. Niu, X.-L. Qi, S.-C. Zhang, X.-C. Ma, and Q.-K. Xue. "Crossover of the three-dimensional topological insulator Bi2Se3 to the two-dimensional limit". In: *Nature Physics* 6.8 (2010), pp. 584–588. URL: `http://www.nature.com/nphys/journal/v6/n8/abs/nphys1689.html`.

[Zha+15] C. Zhang, S.-Y. Xu, I. Belopolski, Z. Yuan, Z. Lin, B. Tong, N. Alidoust, C.-C. Lee, S.-M. Huang, H. Lin, M. Neupane, D. S. Sanchez, H. Zheng, G. Bian, J. Wang, C. Zhang, T. Neupert, M. Z. Hasan, and S. Jia. "Observation of the Adler-Bell-Jackiw chiral anomaly in a Weyl semimetal". In: *arxiv:1503.02630v1* (2015). URL: `http://arxiv.org/abs/1503.02630v1`.

[Zha+16] C.-L. Zhang, S.-Y. Xu, I. Belopolski, Z. Yuan, Z. Lin, B. Tong, G. Bian, N. Alidoust, C.-C. Lee, S.-M. Huang, T.-R. Chang, G. Chang, C.-H. Hsu, H.-T. Jeng, M. Neupane, D. S. Sanchez, H. Zheng, J. Wang, H. Lin, C. Zhang, H.-Z. Lu, S.-Q. Shen, T. Neupert, M. Zahid Hasan, and S. Jia. "Signatures of the Adler-Bell-Jackiw chiral anomaly in a Weyl fermion semimetal". In: *Nat Comms* 7 (Feb. 2016), p. 10735. ISSN: 2041-1723. URL: `http://dx.doi.org/10.1038/ncomms10735`.

[ZS17] X.-T. Zhang and R. Shindou. "Transport properties of density wave phases in three-dimensional metals and semimetals under high magnetic field". In: *Phys. Rev. B* 95.20 (June 2017), p. 205108. URL: `https://doi.org/10.1103/physrevb.95.205108`.

F. Curriculum Vitae

Der Lebenslauf ist in der Online-Version aus Gründen des Datenschutzes nicht enthalten.

Der Lebenslauf ist in der Online-Version aus Gründen des Datenschutzes nicht enthalten.